

# Zuni-Banderas Volcanic Field



**Planetary Geology Field Studies PTYS 594A**

**October 17-21, 2019**

# Table of Contents

<b>Trip Overview (Christopher)</b> .....	<b>1</b>
<b>Geologic Overview (Kiana)</b> .....	<b>2</b>
<b>Effusive Eruptions (Claire)</b> .....	<b>10</b>
<b>Explosive Eruptions (Maria)</b> .....	<b>16</b>
<b>Interplay of Life and Land (Zarah)</b> .....	<b>21</b>
<b>Ground Penetrating Radar 1 (Emileigh, Indujaa, Joana, John)</b> .....	<b>26</b>
<b>Ground Penetrating Radar 2 (Brandon, Nicole, Michael)</b> .....	<b>39</b>
<b>UAV Photogrammetry (Daniel)</b> .....	<b>46</b>
<b>Geology Reference</b> .....	<b>59</b>
<b>Activities</b> .....	<b>85</b>

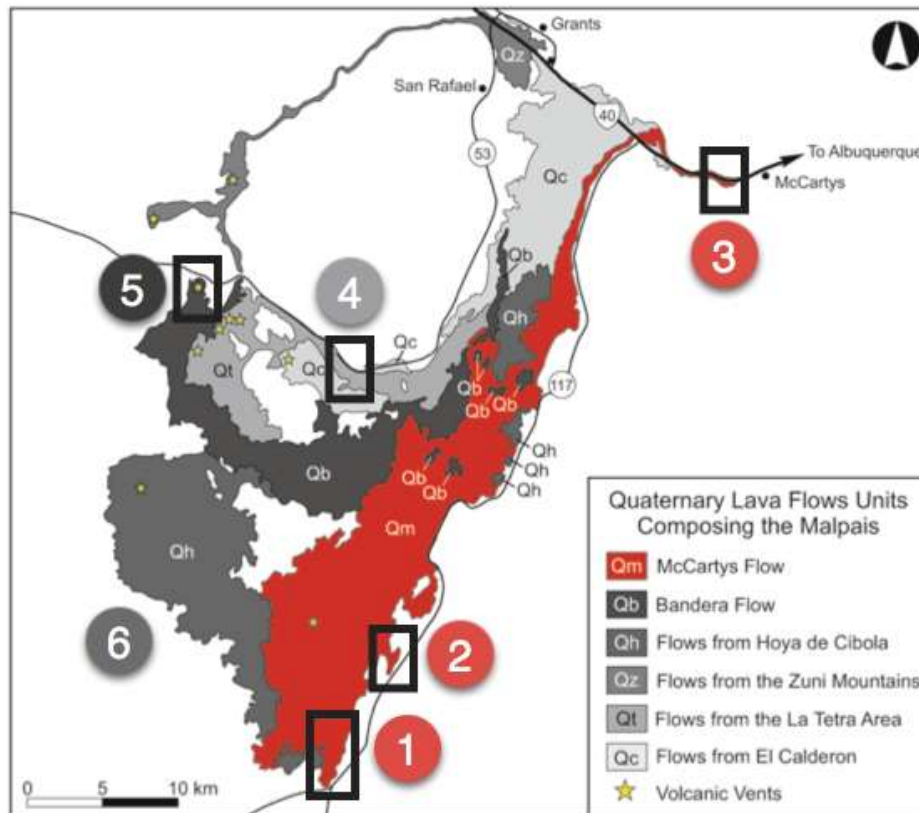
U of A Travel Emergency:	520-307-9576
U of A Travel Incident:	800-243-6124
U of A Risk Management:	520-621-1790
U of A Motorpool:	520-621-3000

Cover photo by L.Crumpler

## Zuni–Bandera Volcanic Field

*Lunar and Planetary Laboratory (LPL) Field Trip: October 17–21, 2019*

The Zuni–Bandera Volcanic Field is located in west-central New Mexico, near the town of Grants (see Figure below). The volcanic field is part of the Jemez lineament, which extends from central Arizona to northeastern New Mexico. This region includes approximately 100 volcanoes, which have erupted during the past 16 Ma, with the youngest volcanic activity occurring 700 to 3000 years ago in what is now the El Malpais National Monument, with the McCartys lava flow-field being emplaced ~2500–3900-years-ago, making it the youngest basalt flow in the region.



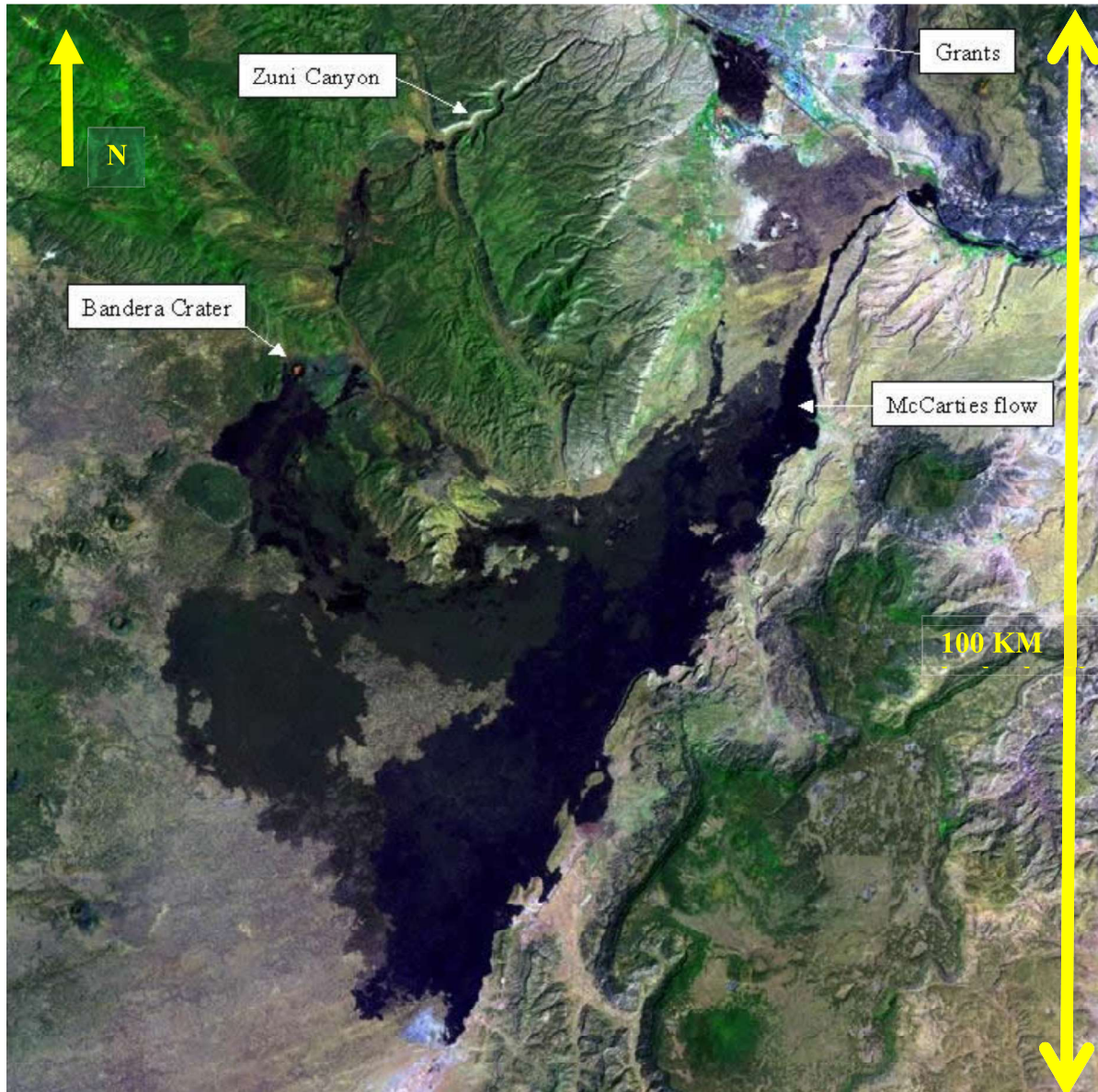
The primary focus of the LPL field trip will be on the McCartys lava flow-field, and it is anticipated that the class will spend one full-day examining the southern part of the flow-field (#1), complete a half-day exercise near the “hammerhead” on the eastern margin of the flow (#2), and stop briefly at road cut exposures near the distal (i.e., northeastern) end of the flow (#3). The half-day excursion at locations #2 and #3 will be paired with a half-day stop to a section of the Twin Craters lava flow-field (#4). The third day of the field trip will examine Bandera Crater (#5) and investigate lava tube structures with local Park Service Rangers located within the Hoya de Cibola lava flow-field (#6). In the event that a lava tubes are closed, the class will instead visit the “Ice Cave” located near #5.

It is expected that each day, the group will depart the campsite at 8:00 am and return by 6:00 pm. Over the course of three days the class will visit the six locations described above. However, the ordering of activities on Days 1, 2, and 3 (i.e., Friday, Saturday, and Sunday) will depend on the Park Rangers’ schedule and the specific campsite location, which should be near Site #4.

## Zuni-Bandera Volcanic Field Overview

Kiana McFadden

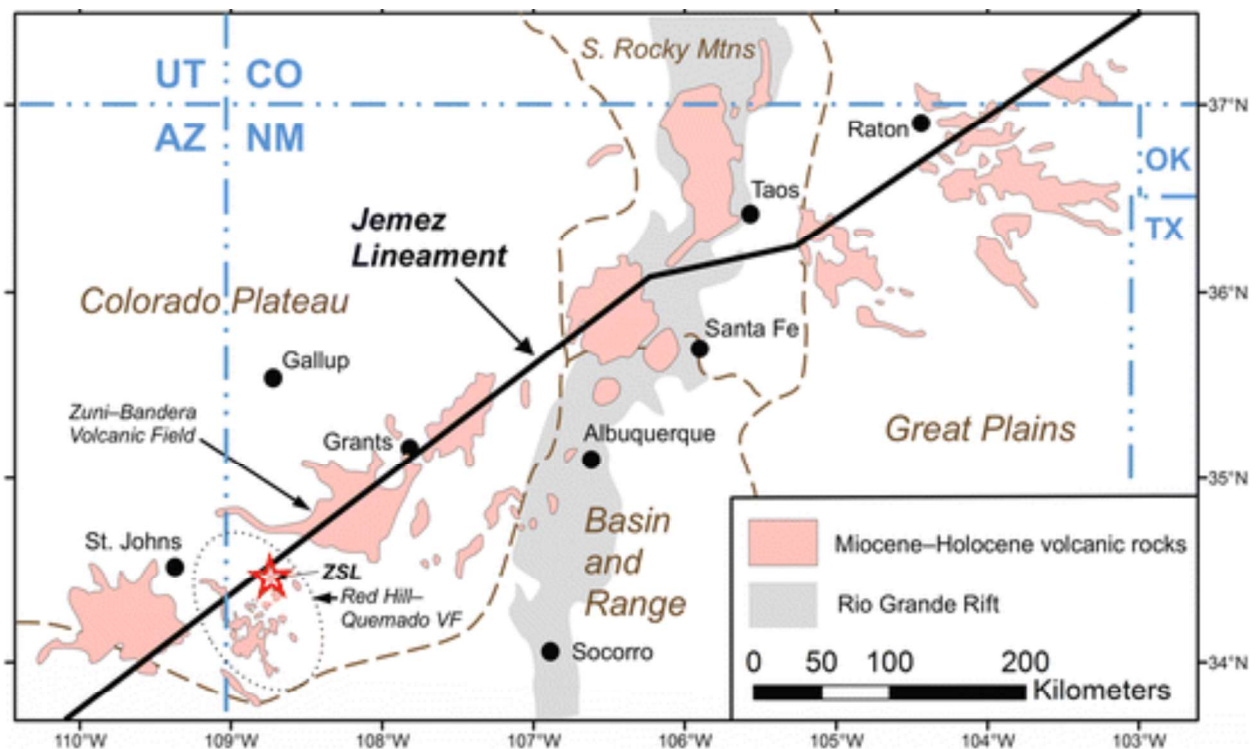
### Introduction



**Fig.1.** This is a satellite image of the Zuni-Bandera Volcanic Field. White boxes and arrows indicate distinctive features within this field. This picture was acquired from the New Mexico Bureau of Geology & Mineral Resources New Mexico Institute of Mining & Technology.

**Figure 1** depicts a satellite image of the Zuni-Bandera Volcanic Field. This volcanic field is located in northwest New Mexico [1]. More specifically, the Zuni-Bandera Volcanic Field can be found at these coordinates of 34.8°N, 108°W [2]. The entire volcanic field expands about 100 km in the north to south direction [1]. The Zuni-Bandera Volcanic Field is filled with a plethora of important geological features. These features include the Zuni Canyon, Bandera Crater Lava Flows, and McCarty's Lava Flows. The lava flows are mostly comprised of basalt [1]. Among these features span an array of cinder cones, vents, and lava tubes. The entire volcanic field expands about 100 km in the north to south direction [1].

### Jemez Lineament-Tectonic Setting



**Fig 2.** This image depicts the Jemez Lineament within the Southwestern United States. The Jemez Lineament intersects the Colorado Plateau. The Zuni-Bandera Volcanic Field is also shown to be dated as Miocene-Holocene age. Onken and Forman, 2011

The Zuni-Bandera Volcanic Field is located along the Jemez Lineament. As shown in **Figure 2** above, this site is the source of other major volcanic activity. In addition, this geological feature extends northeast towards Colorado and southwest towards Arizona while also intersecting the Rio Grande Rift. A transition zone also occurs along the southeastern part of the Colorado Plateau, and the Jemez Lineament separates this

zone from the Rio Grande Rift [15]. Laughlin et. al suggests that volcanism was focused along the Jemez Lineament during Cenozoic time due to the weakness at the Precambrian-age boundary [11]. This volcanic activity started as much as 13 Ma years ago in the Jemez volcanic field, and the lineament serves as a center for late Cenozoic volcanic activity [15]. As a result, cinder cones and basaltic dominant flows occur along this northeast-trending line [15].

### Geologic Age of Volcanic Field

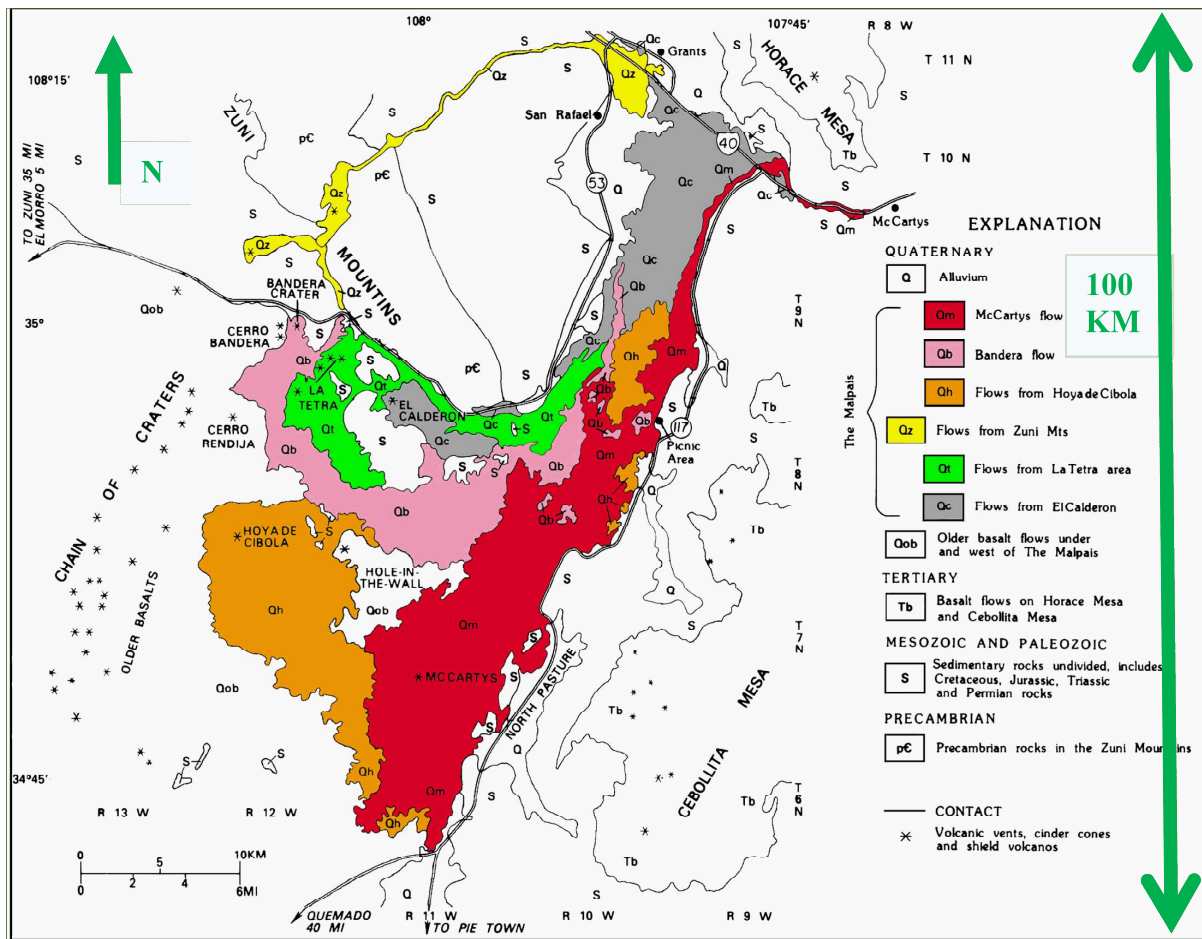
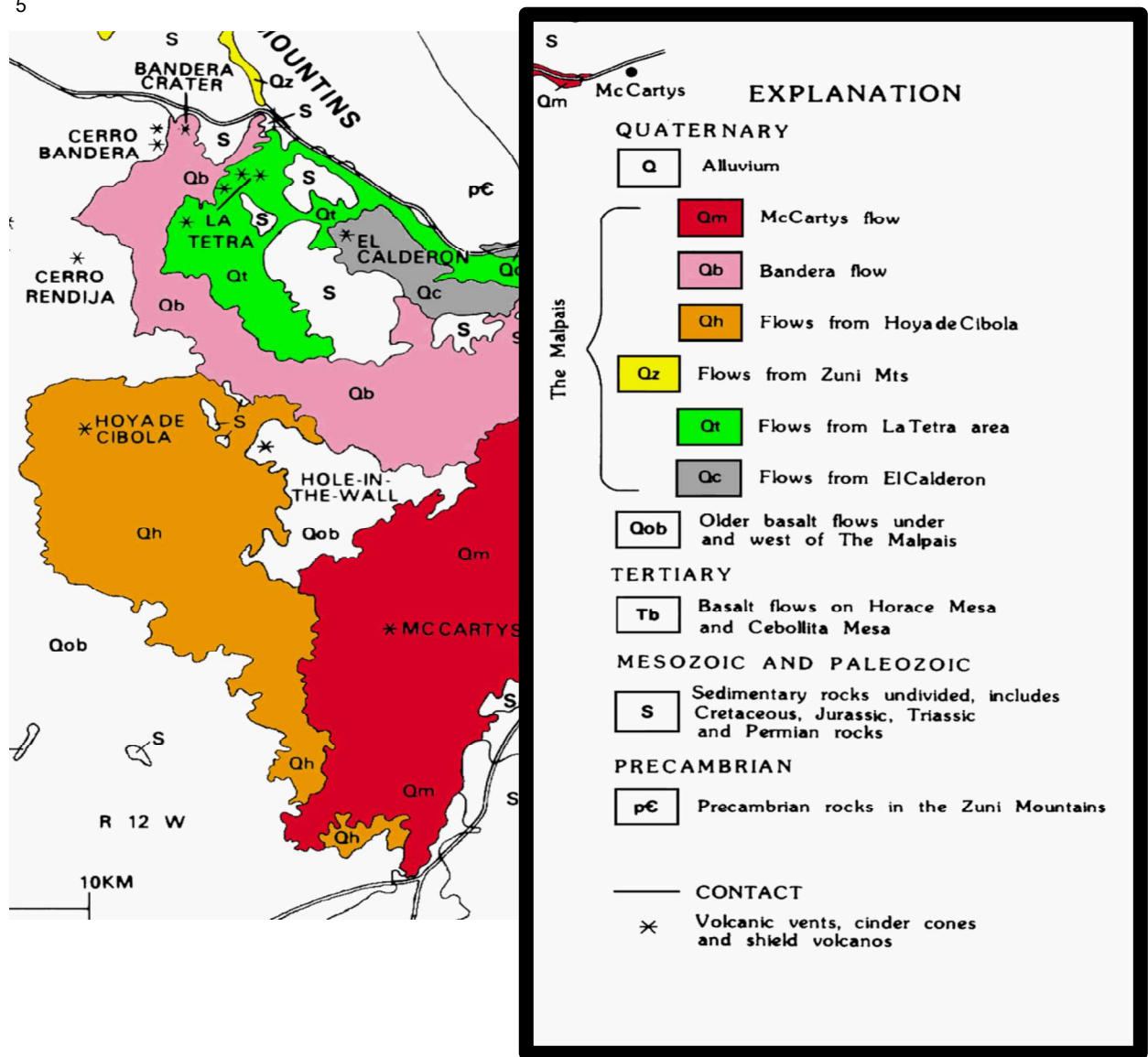


Fig.3. This is a complete geological map of the Zuni-Bandera Volcanic Field. Ages of different areas are highlighted on this map. This picture was acquired from the New Mexico Bureau of Geology & Mineral Resources and New Mexico Institute of Mining & Technology website.



**Fig 3a.** This figure is zoomed in on the ages of the flows for readability. It is taken from the original image in Fig 3.

The Geologic age of this field is depicted by **Figure 3** from the New Mexico Bureau of Geology & Mineral Resources and New Mexico Institute of Mining & Technology website. Within this field, geological ages date from Precambrian to Quaternary. The area of study that we are most interested in includes flows from El Calderon, La Tetra, Zuni Mountains, Hoya de Cibola, Bandera Crater, and McCarty. These flows are also labeled as the Malpais. As shown on the **Figure 3** map, the McCarty Lava Flow is the youngest flow in this study area. The New Mexico Bureau of Geology & Mineral Resources provides a table that summarizes the ages of the many lava flows within this region. It is provided below in **Table 1**. This table puts the McCarty's Lava Flow age to be between 2,500-3,900 years old.

NAME	VENT	TYPE OF FLOW	AGE
<b>McCartys</b>	McCartys Shield	Pahoehoe sheet flow, aa	2,500-3,900
<b>Bandera</b>	Bandera Crater	Aa and tube fed pahoehoe	9,500-10,900
<b>Cerro Hoya</b>	Cerro Hoya Shield	Pahoehoe sheet flows	
<b>Lava Crater</b>	Lava Crater Shield	Tube fed pahoehoe	16,000
<b>Lost Woman Crater</b>	Lost Woman Cinder Cone	Channelized and tube Fed pahoehoe	
<b>Twin Craters</b>	Twin Craters Cinder Cone	Channelized and tube fed pahoehoe	15,800-17,800
<b>Laguna</b>	El Calderon		33,400
<b>Bluewater Flow</b>	El Tintero Cinder Cone		35,600-79,000
<b>Candelaria</b>	Cerro Candelaria	Aa	
<b>El Calderon</b>	El Calderon Cinder Cone and Shield	Aa flowed by pahoehoe	115,000
<b>Zuni Canyon</b>	Paxton Springs Cinder Cone	Channelized aa	Older than Bandera and younger than Bluewater and Laguna flows
<b>Oso Ridge</b>	Oso Ridge Cinder Cone	Aa	Older than Zuni Canyon, younger than El Calderon
<b>Plagioclase Lava</b>	South Rendija Shield	Pahoehoe sheet	
<b>Cerro Rendija</b>	Cerro Rendija Shield	Tube fed pahoehoe	
<b>Cerro Encierro</b>		Tube fed pahoehoe	
<b>Ramah Navajo</b>			7.65 million years
<b>Fence Lake Flow</b>	Unknown		0.6-0.7 million years
<b>North Plains Basalts</b>	Unknown		0.6-0.7 million years

**Table 1.** Mayberry et al., 1999; Laughlin et al., 1993; Laughlin et al., 1994; Dunbar and Phillips, 1994; Phillips et al., 1997). Acquired from the New Mexico Bureau of Geology & Mineral Resources and New Mexico Institute of Mining & Technology website.



## Description of Main Basaltic Lava Flows

According to **Table 1**, many of these lava flows within the Zuni-Bandera Volcanic Field can be characterized as a pahoehoe sheet flow or as an aa flow. Britannica states that “Pahoehoe lava flows are characterized by smooth, gently undulating, or broadly hummocky surfaces [3].” **Figure 4** depicts the smooth flowing surface of a pahoehoe lava flow sheet, and **Figure 5** shows an aa lava flow. Britannica also describes aa flows as being completely opposite of pahoehoe flows [3]. They are defined as, “exceedingly rough, covered with a layer of partly loose, very irregular fragments called clinkers[3].” Self et al. briefly details that inflation caused the pahoehoe lava flow. Inflation is defined as, “the injection of molten lava underneath a solidified crust [16].” Moreover, the McCartys Flow is categorized as a young pahoehoe lava flow with it being 30 miles in length and 119 square miles[13]. **Table 1** indicates that the Bandera Crater lava flow started as a pahoehoe lava flow, but it eventually was tube-fed and is now categorized as an aa flow.



**Fig 4.** This is an example of a pahoehoe lava flow taken from the Kilauea Volcano in Hawaii.  
<https://www.britannica.com/science/lava-volcanic-ejecta#/media/1/332564/94994>



**Fig 5.** This is an example of an aa lava flow taken from Pali in Hawaii.  
<https://volcanoes.usgs.gov/vsc/glossary/aa.html>

## References:

### Websites:

1. [https://geoinfo.nmt.edu/tour/federa/monuments/el\\_malpais/zuni-bandera/background.html](https://geoinfo.nmt.edu/tour/federa/monuments/el_malpais/zuni-bandera/background.html)
2. Global Volcanism Program, 2013. Zuni-Bandera (327120) Volcanoes of the World, v. 4.8.2. Venzke, E (ed.). Smithsonian Institution. Downloaded 11 Sep 2019 (<https://volcano.si.edu/volcano.cfm?vn=327120>). <https://doi.org/10.5479/si.GVP.VoTW4-2013>
3. <https://www.britannica.com/science/lava-volcanic-ejecta#/media/1/332564/94994>
4. <https://volcanoes.usgs.gov/vsc/glossary/aa.html>

### Journals and Books:

5. Aldrich, M.J. Jr., Ander, M. E., and Laughlin, A.W. Geological and geophysical signatures of the Jemez lineament: a reactivated Precambrian structure. United States: N.p., 1981. Web
6. Dunbar, N. W., and Phillips, F. M., 1994, 36Cl surface exposure determinations of eruption ages for quaternary lava flows of the Zuni-Bandera volcanic field: *New Mexico Geology*, v. 16, p. 80.
7. Global Volcanism Program, 2013. Zuni-Bandera (327120) Volcanoes of the World, v. 4.8.2. Venzke, E (ed.). Smithsonian Institution. Downloaded 11 Sep 2019 (<https://volcano.si.edu/volcano.cfm?vn=327120>). <https://doi.org/10.5479/si.GVP.VoTW4-2013>
8. Laughlin, A. W., Perry, F. V., and WoldeGabriel, G., 1994, Geochronology and geochemistry of basalts of the Zuni-Bandera volcanic field; a review and update [abs]: *New Mexico Geology*, v. 16, p. 60.
9. Laughlin, A. W., Charles, R. W., Reid, K., and White, C., 1993, Field-trip guide to the geochronology of the El Malpais National Monument and the Zuni-Bandera volcanic field, New Mexico, *New Mexico Bureau of Geology and Mineral Resources Bulletin* 149, p. 23.
10. Laughlin, A. W., Perry, F. V., Damon, P. E., Shafiqullah, M., Harrington, C. D., Wells, S. G., and Drake, P., 1993, Geochronology of the Mount Taylor, Cebollita Mesa, and Zuni-Bandera volcanic fields, Cibola County, New Mexico: *New Mexico Geology*, v. 15, no. 4.
11. Laughlin, A. W., Aldrich, M.J., Jr., M.E. Ander, G.H. Heiken, and D.T. Vaniman, 1982 pp. 279-284
12. Laughlin, A. W., Poths, J., Healey, H. A., Reneau, S., and WoldeGabriel, G., 1994, Dating of Quaternary basalts using the cosmogenic <sup>3</sup>He and <sup>14</sup>C methods with implications for excess <sup>40</sup>Ar: *Geology*, v. 22, p. 135-138.
13. Nichols, Robert L. "Mccartys Basalt Flow, Valencia County, New Mexico." *Geological Society of America Bulletin*, vol. 57, no. 11, 1946, p. 1049., doi:10.1130/0016-7606(1946)57[1049:mbfvcn]2.0.co;2.
14. Onken, J., Forman, S. *Bulletin of Volcanology*, 2017, Volume 79, Number 1, Page 1
15. Phillips, F. M., Dunbar, N. W., and Zreda, M. G., 1997, A Test of Chlorine-36 for Dating of Late Quaternary Basaltic Volcanoes [abs]: *Eos, Transactions, American Geophysical Union*, v. 78, no. 46, p. 760
16. Self, S., et al. "The Importance Of Pāhoehoe." *Annual Review of Earth and Planetary Sciences*, vol. 26, no. 1, 1998, pp. 81–110., doi:10.1146/annurev.earth.26.1.81.
17. Wood, Charles, and Jürgen Kienle. "Western USA." *Volcanoes of North America: United States and Canada*, edited by Charles A. Wood, 1992, pp. 149–152.



John Gemperline

2 hrs · 🧑



Me for the next week on the grad geology field trip:



## Effusive Volcanic Processes

### Overview

Effusive volcanic eruptions are those for which lava flows onto the surface, in contrast to explosive eruptions, for which pyroclasts and ash are thrown into the air. The difference between the two types comes from the viscosity of the magma. As magmas rise toward the surface, they experience less pressure and gases are less soluble in them (Melosh, 2011). For low viscosity magmas (silica poor, basaltic) gases are able to escape easily and rise to the top, where they are erupted first, followed by the magma (Melosh, 2011). For higher viscosity magmas (silica rich, andesitic and rhyolitic magmas) gases are trapped as bubbles in the magma and ultimately explode out of the magma, leading to the eruption of clasts and ash (Melosh, 2011).

Basaltic volcanism, and thus effusive volcanism, occurs where the crust is thinner, because basaltic magmas are denser than other magmas (Murase and McBirney, 1973) and thus not buoyant enough to reach the surface through thick continental crust. Therefore this type of volcanism tends to occur at rift zones like mid-ocean ridges and mantle plume hot-spots (Grotzinger and Jordan, 2010).

### Morphology

#### Lavas Flows

There are two main types of basaltic lava flows: pāhoehoe and 'a'ā (Fig. 1). Pāhoehoe has a smooth, sometimes ropy texture, while 'a'ā has a very rough texture, with the surface covered in chunks of crust. A single flow can be partly pahoehoe and partly 'a'a.



Figure 1: a) pahoehoe lava flow ([https://www.lpi.usra.edu/publications/slidesets/hawaiiivolcanoes/slidespages/slide\\_04.html](https://www.lpi.usra.edu/publications/slidesets/hawaiiivolcanoes/slidespages/slide_04.html)) and b) 'a'ā lava flow ([http://volcano.si.edu/learn\\_galleries.cfm?p=12](http://volcano.si.edu/learn_galleries.cfm?p=12)).

Pahoehoe advances by inflation. Measurements from active flows on Kilauea showed that it starts out as thin flows of 10-50 cm thick due to its low yield stress (Hon et al., 1994). As it cools, the crust hardens and pressure builds underneath it as lava continues to flow underneath, causing the crust of the flow to be uplifted, i.e. inflated (Hon et al., 1994). The flows can be inflated up to 4 m (Hon et al., 1994). Because flows tend to follow topographic lows, when they inflate they can cause topographic inversion. When the front of the crust can no longer support the force of the lava behind it, toes break out from it and the inflation process repeats.

When flows occur on shallow slopes of  $<1-2$  deg, they are not emplaced in channels and these toes coalesce to produce a sheet flow with billowed forms on the surface (Hon et al., 1994). Flows on steeper slopes tend to create channels. In addition, downslope flow exceeds lateral flow, and toes don't tend to coalesce. This type of flow exhibits features like tumuli that are indicative of inflation and is described as hummocky (Hon et al., 1994).

Tumuli (Fig. 2) are circular to elongate domes 1-10 m high and 10s of meters wide, formed by uplift of crustal blocks during inflation, likely at locations where there is an existing swell in the flow (Walker, 1991). Lava rise plateaus are flatter features up to hundreds of meters across and raised a few meters high, also formed by uplift (Walker, 1991). Sometimes parts of lava rise plateaus fail to be elevated as the surrounding area rises, leading to lava-rise pits/inflation pits of similar dimensions to tumuli (Walker, 1991)



Figure 2: Tumulus. <http://volcano.oregonstate.edu/book/export/html/136>.

Lava tubes can be formed by either of these types of pahoehoe flows. In the case of sheet flows, tubes form because flows cool more rapidly at the margins, leading to less flow at the margins, and lava moving through the center of the flow. Once the flow stops (and if it is on a steep enough slope to drain) the hardened margins leave behind a tube (Hon et al., 1994). For non-sheet flows, lava flowing in channels may form a crust which remains after the lava has drained (Greeley, 1971).

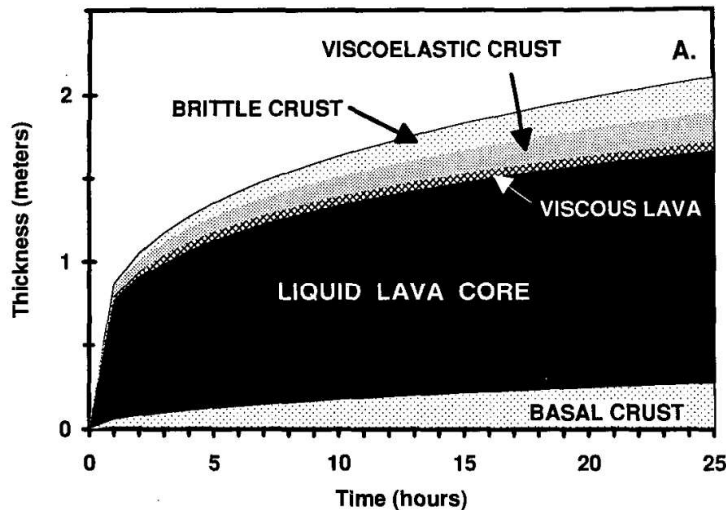


Figure 3: Internal structure of sheet flow pahoehoe from Hon et al 1994.

The internal structure of these pahoehoe flows includes three crustal layers (Fig. 3) The middle layer, at temperatures of 800-1700 C, provides the most strength to the flow and is the most important in determining the internal pressure, and retains the liquid lava during the inflation phase (Hon et al., 1994).

'A'a has a rough surface and base covered with rocks called clinkers. 'A'a is not associated with inflation. Instead, as it flows, clinkers on the surface fall off the top and are run over by the flow. It is associated with a higher eruption rate than pahoehoe of  $>5-10 \text{ m}^3/\text{s}$  (Rowland and Walker, 1990). Because 'a'a has a high effusion rate and becomes channelized, it flows rapidly. Crust is disrupted quickly, leading to rapid heat loss and increase in viscosity. It reaches a viscosity for which it cannot flow fast enough to repair disruptions in the crust, thus leading to the rubbly texture of the crust. Pahoehoe's lower effusion rate and its spread over various lobes means it flows slowly. The skin cools, thickens, and becomes static before the viscosity has increased to the point where the lava can't repair the crust, so it has a smooth surface.

#### Landforms

Effusive volcanism forms large flood basalt sheets as well as shield volcanoes. These are built up over the course of multiple basaltic flows, which because of their low viscosity spread widely rather than piling up steeply as more viscous flows do (Grotzinger and Jordan, 2010).

#### Physics

In a simple model, lava flows can be described as Bingham fluids: shear stress is related to strain rate linearly, after certain stress (the yield stress) is surpassed. Before that yield stress is reached, the fluid is static. This can be described by an equation of the form:  $\sigma = \sigma_0 + \eta \dot{\epsilon}$  where  $\sigma$  is the shear stress,  $\sigma_0$  is the yield stress,  $\eta$  is the viscosity, and  $\dot{\epsilon}$  is the strain rate (Griffiths, 2000).

By doing force balance in a column of the lava, you can derive an expression for the height of the flow as a function of distance across the flow.

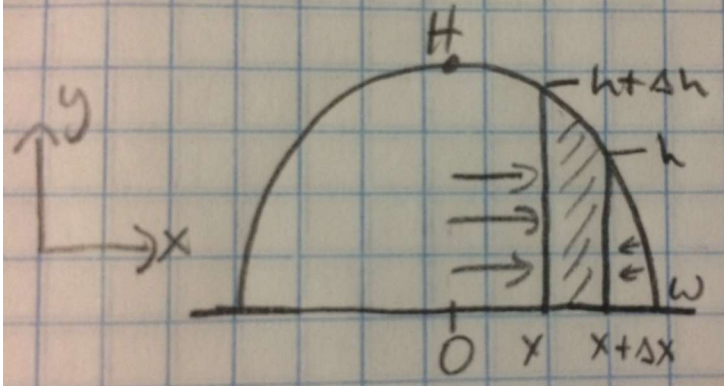


Figure 4: Diagram of a cross section of a lava flow with width  $w$  and height  $H$ .

Set the force due to the pressure difference on either side of the column equal to the force related to the shear stress. Consider the column, arbitrarily, to be 1 m thick.

$$\frac{1}{2} \rho g (h + \Delta h)^2 (1 \text{ m}) - \frac{1}{2} \rho g h^2 (1 \text{ m}) = -\sigma_0 \Delta x (1 \text{ m})$$

Rearranging this, assuming that the yield stress and density are constant along the width of the flow, and integrating from the height of the flow  $H$  to 0 and the distance from 0 to the width of the flow  $w$  gives a relation for the height of the flow in terms of the width:

$$H^2 = \frac{2\sigma_0}{\rho g} w$$

Integrating from the maximum height  $H$  to some height  $h$  and from 0 to some distance  $x$ , gives a more general expression:

$$h = \sqrt{H^2 - \frac{2\sigma_0}{\rho g} x}.$$

These equations can be used to find the yield stress of flows from measurements of the width and height of flows. The heights and widths of flows along with viscosity can also be related to the speed and discharge rate of the flows. After the yield stress is exceeded, the flows are essentially Newtonian and this results in a discharge rate of

$$Q_E = \frac{2}{3} U_{\text{surf}} H W_c \quad \text{where} \quad U_{\text{surf}} = \frac{\rho g H^2 \sin \alpha}{2 \eta}. \quad (\text{Melosh, 2011}).$$

The viscosity of a basaltic flow can be taken to follow:

$$\eta_A(T, \phi) = \eta_0 (1 - \phi/\phi_{\text{max}})^{-2.5} e^{\gamma(T_0 - T)},$$

where  $\eta$  is the viscosity,  $\phi$  is the volume fraction of crystals,  $\gamma$  is a constant  $\sim 0.04$ , and  $T$  is the temperature (Griffiths, 2000). The constants  $\eta_0$  and  $T_0$  are reference values (at the vent for example) and  $\phi_{\text{max}}$  is the maximum crystal fraction that allows flow. Intuitively, this equation indicates that as the crystal fraction increases, the viscosity increases and that as the temperature increases, the viscosity decreases.

The surface of lavas cool by radiation and convection (Griffiths, 2000) and the thickness of the crust increases as the surface cools. The rate at which this occurs is  $C = \lambda \sqrt{4\kappa t}$  where  $\lambda$  is the root to an equation that depends on properties of the lava, such as its heat capacity and diffusivity,  $\kappa$  is the thermal diffusivity, and  $t$  is time.

### *Effusive volcanism on other solar system bodies*

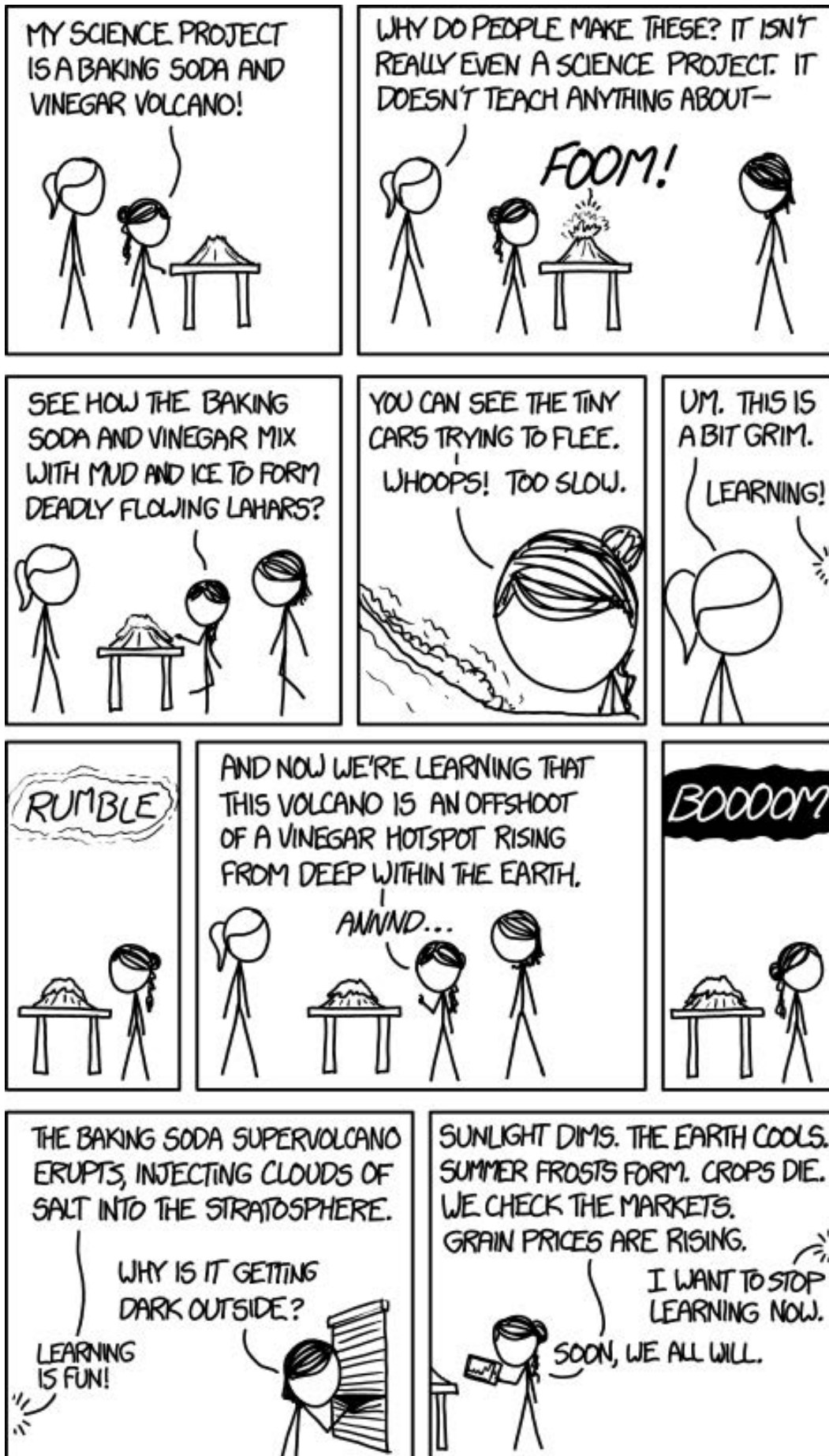
Because the formation of silica rich magmas such as andesite requires water to be brought into the mantle by plate tectonics, these magmas are not common elsewhere in solar system. Therefore basaltic volcanism and thus effusive volcanism is the type that primarily occurs elsewhere in the solar system. There is evidence for prior effusive volcanism on Mercury (smooth volcanic plains observed), Venus (shield volcanoes and indications of large scale planetary resurfacing have been observed), the moon (the maria flood basalts), and Mars (for example the shield volcano Olympus Mons, and possible pahoehoe-like flows in Hrad Vallis and Elysium Planitia; (Hamilton et al., 2011; Voigt and Hamilton, 2018)) and current volcanism is everywhere on Io (Melosh, 2011).

Properties such as viscosities and yield stresses for silicate magmas are similar on these various bodies (Hiesinger et al., 2007). Another commonality is that the crust thickening rate only depends on properties of the lava not the planetary body and will always be proportional to the square root of time. The equation for the height of a flow as a function of the width indicates that for bodies with lower surface gravity than on Earth, a flow of a given width will be thicker than it would be on Earth. The gravity also affects the discharge rate:  $Q$  depends on  $H$  and  $U$ , though the  $g$  dependence in  $U$  disappears when put  $H$  into the equation. So for planets with lower gravity, you would expect higher flow thicknesses and higher discharge rates.

### *References*

- Greeley, R., 1971. Observations of Actively Forming Lava Tubes and Associated Structures, Hawaii.
- Griffiths, R.W., 2000. The Dynamics of Lava Flows. *Annu. Rev. Fluid Mech.* 32, 477–518.  
<https://doi.org/10.1146/annurev.fluid.32.1.477>
- Grotzinger, J., Jordan, T., 2010. Volcanoes, in: *Understanding Earth*. W. H. Freeman and Company, pp. 305–335.
- Hamilton, C.W., Fagents, S.A., Thordarson, T., 2011. Lava–ground ice interactions in Elysium Planitia, Mars: Geomorphological and geospatial analysis of the Tartarus Colles cone groups. *J. Geophys. Res.* 116, E03004.  
<https://doi.org/10.1029/2010JE003657>
- Hiesinger, H., Head, J.W., Neukum, G., 2007. Young lava flows on the eastern flank of Ascraeus Mons: Rheological properties derived from High Resolution Stereo Camera (HRSC) images and Mars Orbiter Laser Altimeter (MOLA) data. *J. Geophys. Res.* 112, E05011. <https://doi.org/10.1029/2006JE002717>
- Hon, K., Kauahikaua, J., Denlinger, R., Mackay, K., 1994. Emplacement and inflation of pahoehoe sheet flows: Observations and measurements of active lava flows on Kilauea Volcano, Hawaii. *Geol. Soc. Am. Bull.* 106, 351–370. [https://doi.org/10.1130/0016-7606\(1994\)106<0351:EAIOPS>2.3.CO;2](https://doi.org/10.1130/0016-7606(1994)106<0351:EAIOPS>2.3.CO;2)
- Melosh, H.J., 2011. Volcanism, in: *Planetary Surface Processes*. Cambridge University Press, pp. 169–218.
- Murase, T., McBirney, A.R., 1973. Properties of Some Common Igneous Rocks and Their Melts at High Temperatures. *Geol. Soc. Am. Bull.* 84, 3563. [https://doi.org/10.1130/0016-7606\(1973\)84<3563:POSCIR>2.0.CO;2](https://doi.org/10.1130/0016-7606(1973)84<3563:POSCIR>2.0.CO;2)
- Rowland, S.K., Walker, G.P., 1990. Pahoehoe and aa in Hawaii: volumetric flow rate controls the lava structure. *Bull. Volcanol.* 52, 615–628. <https://doi.org/10.1007/BF00301212>
- Voigt, J.R.C., Hamilton, C.W., 2018. Investigating the volcanic versus aqueous origin of the surficial deposits in Eastern Elysium Planitia, Mars. *Icarus* 309, 389–410. <https://doi.org/10.1016/J.ICARUS.2018.03.009>
- Walker, G.P.L., 1991. Structure, and origin by injection of lava under surface crust, of tumuli, lava rises, lava-rise pits, and lava-inflation clefts in Hawaii. *Bull. Volcanol.* 53, 546–558. <https://doi.org/10.1007/BF00298155>





# Volcanic Processes: Explosive Eruptions

Maria Steinrueck

## Factors determining explosivity

In general, higher viscosity and higher gas content of the magma lead to more explosive eruptions. This is because explosions happen when gas gets trapped in the magma and builds up until the pressure becomes too high.

The viscosity of magma decreases with increasing temperature and increases with increasing silica content (because silica polymers form even before the magma fully crystallizes, increasing viscosity). Explosive eruptions therefore in general are associated with intermediate and felsic magmas.

*Table 1 Reminder for non-geology folks like me*

	Silica content	Mg and Fe content	Typical rock formed in volcanic eruptions
<b>Mafic</b>	Low	High	Basalt
<b>Intermediate</b>	Intermediate	Intermediate	Andesite
<b>Felsic</b>	High	Low	Rhyolite

## Volcanic Explosivity Index

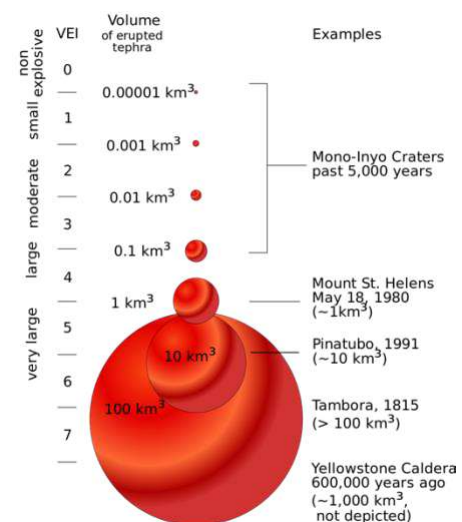
The Volcanic Explosivity Index (VEI) was developed by Chris Newhall and Stephen Self in the 1980s. It categorizes the explosivity of volcanic eruptions based on multiple criteria including

- Volume of ejected tephra
- Height of eruptive column
- Height of spreading
- Qualitative description (“effusive”, “gentle”, ..., “mega-colossal”).

Starting at VEI-2, the VEI increases logarithmically with the volume of ejected tephra. The VEI can only be accurately determined for historically observed eruptions. For past eruptions, the VEI can only be estimated based on the volume of ejecta.

The higher the VEI, the lower is the world-wide frequency of the eruption type. VEI-1 Strombolian eruptions occur on a daily basis, while VEI-6 Plinian eruptions occur 1-2 times per century and VEI-8 Ultra-Plinian events are estimated to occur less than once in 50,000 years.

*Figure 1 Volcanic Explosivity Index (credit: USGS)*



## Strombolian Eruptions

Strombolian eruptions are small-scale explosive volcanic eruptions with a VEI of 1 to 3. They are named after Stromboli volcano off the west coast of Italy. The lava in Strombolian eruptions is typically basaltic lava with relatively high viscosity. Typically, during these eruptions, material is thrown tens to a few hundreds of meters into the air and then falls back onto the ground in ballistic trajectories. Over time, material accumulates around the eruption site to form a scoria cone (cinder cone).

Scoria cones are tens to hundreds of meters tall. They have uniform slopes close to the angle of repose ( $30^\circ$  to  $40^\circ$ ). Some, but not all scoria cones are monogenetic, meaning that they formed in a single eruption episode.



Figure 3 Examples of scoria cones. Left: Bandera Crater, a 10-20 ka old scoria cone in the Zuni-Bandera volcanic field (credit: L. Crumpler) Right: SP Crater in the San Francisco volcanic field near Flagstaff (credit: USGS)



Figure 2 Strombolian Eruption of Stromboli volcano in Italy (credit: Wolfgang Beyer)

## Vulcanian Eruptions

Vulcanian eruptions are named after Vulcano, a volcano on the Italian island of Vulcano. With a VEI of 2 to 3, they are more explosive than Strombolian eruptions. Typically, Vulcanian eruptions start with a sequence of loud steam explosions (phreatomagmatic) that clear away rock over the volcanic vent. An eruption column (cloud of ash and tephra, mixed with volcanic gases) forms and can reach heights of 5-10 km.

Throughout the eruption, explosions remain distinct, “cannon-like” bursts. The eruption can be accompanied by pyroclastic flows. Vulcanian eruptions are typically associated with intermediate to felsic magma.



Figure 4 Vulcanian eruption of Tavurvur volcano in Papua New Guinea (credit: J.W. Ewert, USGS)

## Plinian Eruptions

Plinian (VEI $\geq$ 4) and Ultra-Plinian (VEI $\geq$ 6) eruptions are the most catastrophic and explosive volcanic eruptions. Unlike Strombolian and Vulcanian eruptions, which have discrete explosive bursts, they produce a sustained eruption column that continuously expels enormous volumes of tephra, ash and volcanic gases. These ash plumes can reach heights of up to 45 km. Often, extensive, highly destructive pyroclastic flows are part of the eruption. Plinian eruptions were named after Pliny the Younger, who extensively described the 79 AD eruption of Mount Vesuvius, which buried the cities of Pompeii and Herculaneum. Other famous examples are the 1980 eruptions of Mount St. Helens and the Ultra-Plinian 1991 eruption of Mount Pinatubo.



Figure 5 Examples of Plinian eruptions. Left: 1991 eruption of Redoubt Mountain (credit: R. Cluclas, USGS). Right: 1980 eruption of Mount St. Helens (credit: Austin Post, USGS)

## Planetary Connection

While there are many examples of effusive volcanism (flood volcanism and shield volcanoes) on planetary bodies such as the Moon, Mars and Venus, it has proven much harder to find unambiguous evidence of the classic explosive eruption types mentioned above on these bodies. One example of explosive volcanism that has been relatively well-studied is rootless cones (e.g., Lanagan et al., 2001). These are formed through steam explosions that happen when lava flows over damp ground or a small enclosure of water or ice.

There are also cones that have been interpreted to be cinder cones by one author (e.g., Brož and Tauber, 2011). However, alternative interpretations (both volcanic and non-volcanic) cannot be excluded for these cones.

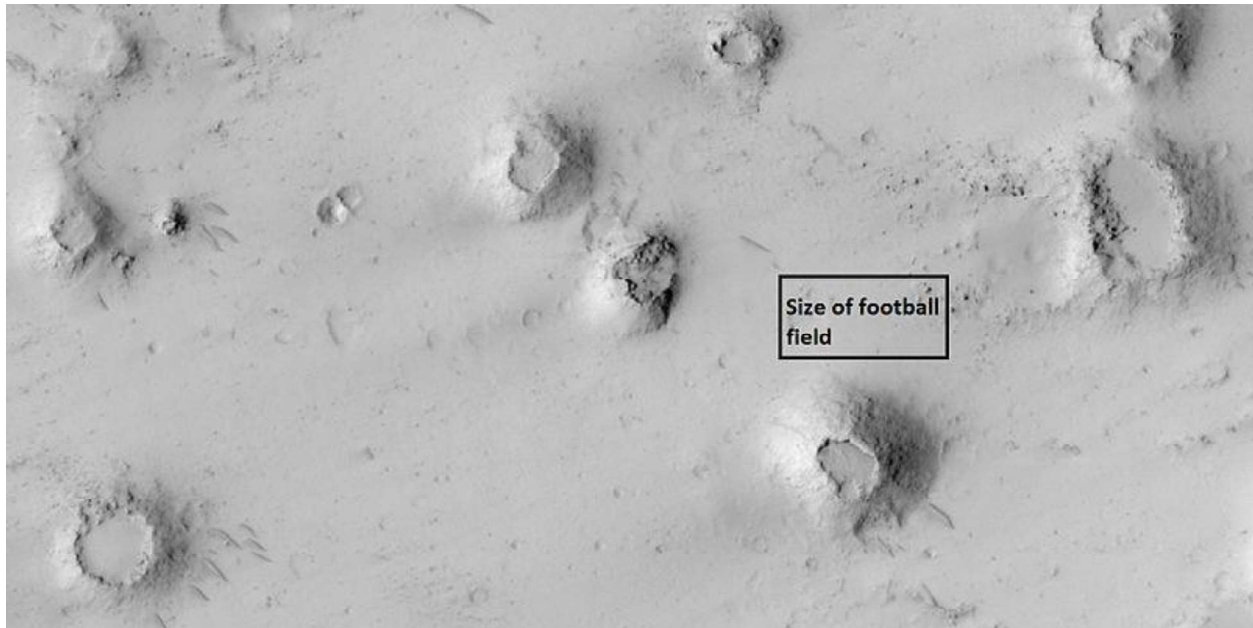


Figure 6 HiRISE image of rootless cones in Elysium quadrangle on Mars. (credit: NASA/JPL/ University of Arizona)

## References

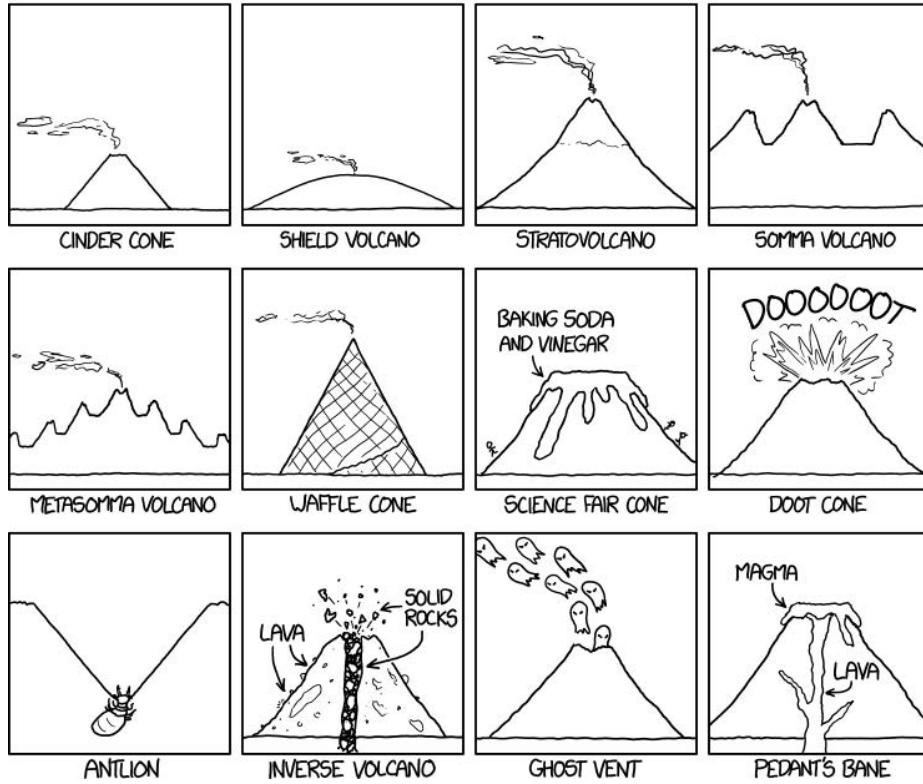
### Journal Articles:

- Brož, P. and Hauber, E. (2011). *Icarus*, Vol. 218, 1, p. 88-89.  
 Lanagan, P. D. et al. (2001). *Geophysical Research Letters*, Vol. 28, p. 2365-2368.  
 Newhall, C. and Self, S. (1982). *Journal of Geophysical Research*, Vol. 87, C2, p. 1231-1238.

### Websites:

- [http://sci.sdsu.edu/how\\_volcanoes\\_work/Controls.html](http://sci.sdsu.edu/how_volcanoes_work/Controls.html) (10/10/2019)  
[http://sci.sdsu.edu/how\\_volcanoes\\_work/Variability.html](http://sci.sdsu.edu/how_volcanoes_work/Variability.html) (10/11/2019)  
[https://en.wikipedia.org/wiki/Volcanic\\_Explosivity\\_Index](https://en.wikipedia.org/wiki/Volcanic_Explosivity_Index) (10/11/2019)  
<http://www.nmnaturalhistory.org/volcanoes/zuni-bandera-field-and-mccartys-lava-flow>  
 (10/11/2019)  
[http://sci.sdsu.edu/how\\_volcanoes\\_work/Vulcanian.html](http://sci.sdsu.edu/how_volcanoes_work/Vulcanian.html) (10/12/2019)  
[https://en.wikipedia.org/wiki/Vulcanian\\_eruption](https://en.wikipedia.org/wiki/Vulcanian_eruption) (10/12/2019)  
[http://sci.sdsu.edu/how\\_volcanoes\\_work/Plinian.html](http://sci.sdsu.edu/how_volcanoes_work/Plinian.html) (10/12/2019)  
<https://www.nature.com/news/2001/010614/full/news010614-3.html> (10/12/2019)

# A GUIDE TO VOLCANO TYPES



IMAGINE EARTH'S HISTORY AS A FOOTBALL FIELD, FROM THE PLANET'S FORMATION AT ONE END TO TODAY AT THE OTHER.

COMPLEX LIFE WOULD BE LARGELY LIMITED TO THE FINAL TEN YARDS.

DINOSAURS APPEAR AT THE FIVE-YARD LINE, THE AGE OF MAMMALS HAPPENS IN THE LAST 1½ YARDS, AND HUMANS ARISE IN THE FINAL FEW MILLIMETERS.

ALL OF WRITTEN HISTORY WOULD FIT IN A STRIP NARROWER THAN A SINGLE HAIR.

"TWO WEEKS" WOULD BE TOO SMALL TO SEE EVEN WITH A POWERFUL MICROSCOPE.

MM HMM.

GEOLOGISTS ALWAYS TRY THIS WHEN THEY'RE LATE TURNING SOMETHING IN.

**Awesome** 😊

if you're having a bad day... just look at this lizard



## Interplay of Life and Land on and around the Zuni-Bandera Volcanic Field

Geology ↔ Soil ↔ Climate ↔ Flora ↔ Fauna ↔ Human Interactions

Zarah Brown October 11th, 2019

### Geology, Soil, Climate

The Zuni-Bandera Volcanic Field contains five lava flows ranging from ~3,000 to 54,000 years old, of both aa and pahhoehoe types. These provide a wide array of volcanic substrates for life. Cinder cones dot the landscape and lava tubes form underground caves. Cracks and depressions in the lava surface along with the collapse of lava tubes add unevenness to the terrain. The oldest flows in this region are more heavily covered with sand, soil and sediment delivered by flowing water and aeolian processes from the surrounding landscape. While some of this volcanic field is characterized by barren rock, much of it is covered by forest, shrubland and grassland (see Fig. 1). Kipukas are islands of pre-existing rock around which lava has flowed. The underlying sedimentary limestone, sandstone and shale can provide archipelagos of habitat for plants that cannot otherwise grow on volcanic substrate.

Local vegetation depends on soil, climate, elevation and aspect (compass direction a slope faces). The El Malpais National Monument (ELMA) that encompasses most of the Zuni-Bandera Volcanic Field ranges from 1,950 to 2,560 m in elevation (6,400-8,400 ft). The cool, semi-arid continental climate here is typical of New Mexico. This region gets about 280 mm (11 in) of rain annually, concentrated in the summer monsoon season. Flash flooding helps transport sediment and contributes to the formation of arroyos. Surface water percolates into the groundwater within a few weeks. Volcanic rocks can be vesicular and porous and the lava beds retain water better than the surrounding land. Water percolates down into the basalt, where it is insulated from evaporation and can form pools. Plants can access this water through deep root system. In some cases, this water becomes ice, for example, at the Bandera Ice Cave. The moist, cool environment near the mouths of ice caves can support plant species like ferns, mosses and lichens, which would otherwise not grow in the surrounding arid climate.

### Flora

The McCarty's flow and Bandera flows are the youngest in this region (~3 and ~10 ka, respectively). At higher elevations, these flows host low density coniferous forests of Douglas-fir and ponderosa pine. Aspen can sometimes be found growing from fissures within the lava. At lower elevations, these woodlands become dominated by the shorter pinyon pine and one-seed junipers. The understory of the younger flows is sparse; grasses and other vegetation exist sporadically where soils have accumulated. Because of scant understory and open canopy, fire is relatively infrequent in young flows, allowing for trees to live longer. Tree ring data from a dead Rocky Mountain juniper log showed it growing between 29 BCE and 1859 CE. ELMA is currently home to Douglas-firs dating from between 719-1062 CE, one of the older living Douglas-firs in existence. Ponderosa pine are resistant to both fire and drought and tend to be found in sites that are drier.

The Twin Craters, Hoya de Citoya and El Calderon flows are older (~16, 50, 54 ka, respectively). Due to the more robust and uniformly distributed soil layers, these flows exhibit more developed understories. The abundance of grasses fosters more frequent fires and can lead to a lower density of trees. Following Fig. 1 is an identification guide for three of the most predominant tree species in the national monument.

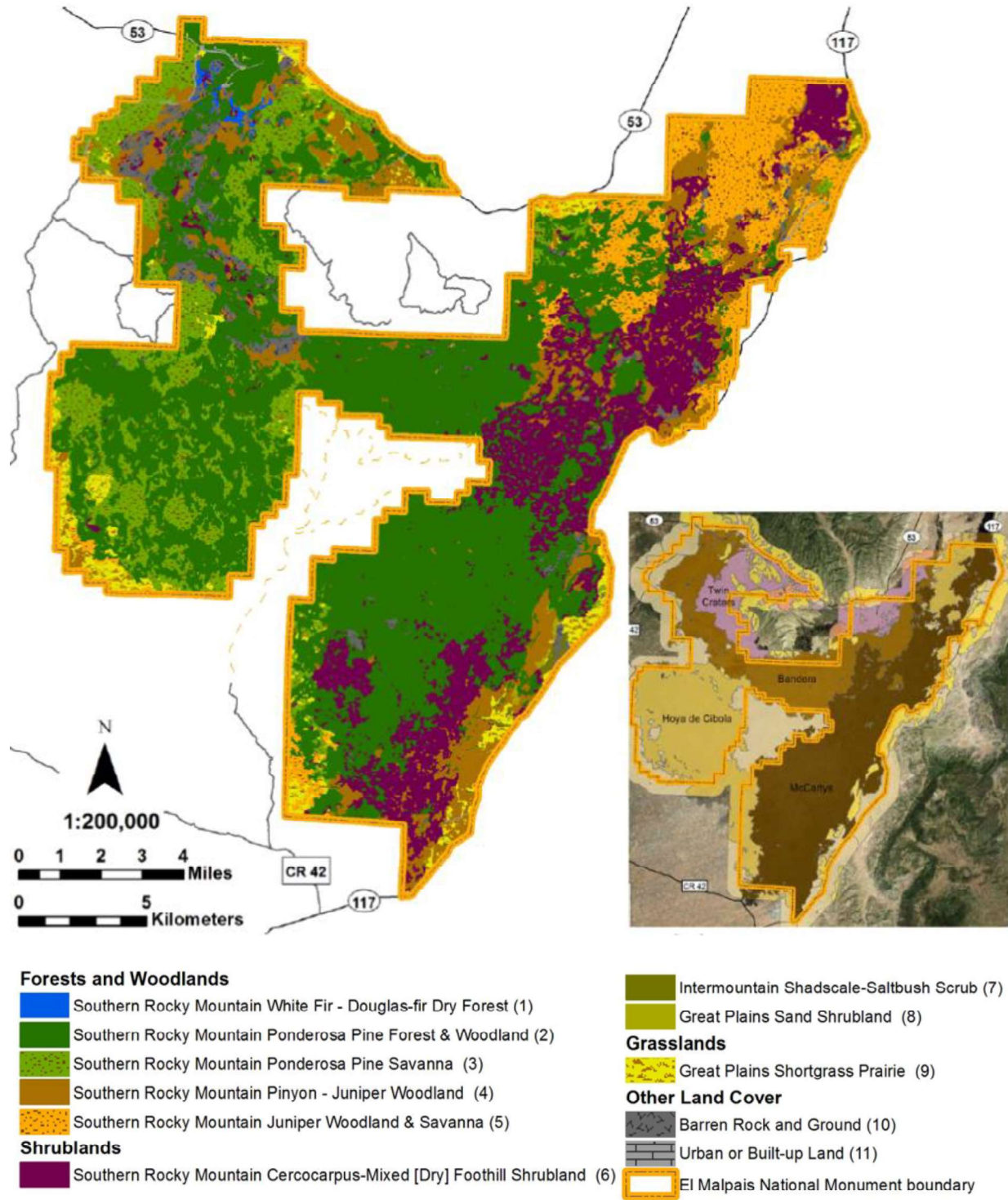


Figure 1. Vegetation map of El Malpais National Monument. Inset shows four of the volcanic flows in ELMA. These figures are 26 and 8, respectively, from the National Resource Technical Report NPS/SCPN/NRTR-2013/803.

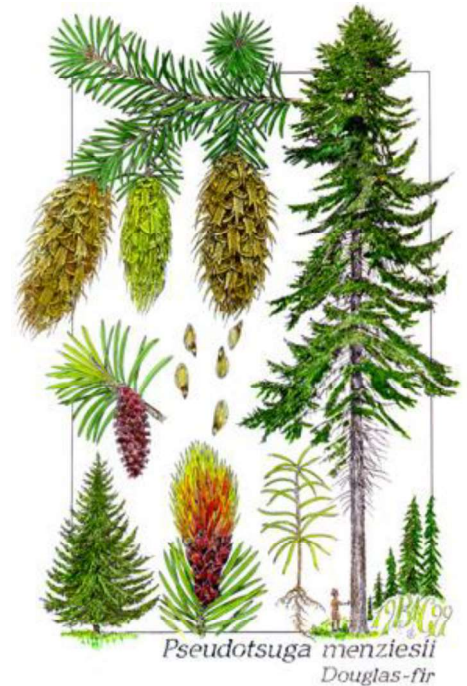


## Douglas Fir

*Pseudotsuga menziesii*

Douglas-fir can be identified by their cones, which point downward and have three-pointed bracts sticking out of the scales, which drop to the ground intact. They have soft, thin needles spiraling out in double rows from the twig. Bark is grey to brown, becoming darker and more deeply furrowed with age. Young trees take on a conical shape, making them popular for Christmas trees, but develop a characteristic droop as they grow and age. While Douglas-firs grow on average to be 70 m (210 ft), on the shallow soil of the lava fields they grow stunted, typically reaching only about 5 m (16 ft).

These trees host insects, small mammals and epiphytic plants like lichens and mosses. It also supports microscopic fungi and Scuzz, a cohort of fungi, algae, yeasts and bacteria that can be found in or on the needles. Scuzz reduces the loss of needs to needle-eating insects and increases the nitrogen intake for the tree.



## Ponderosa Pine

*Pinus ponderosa*

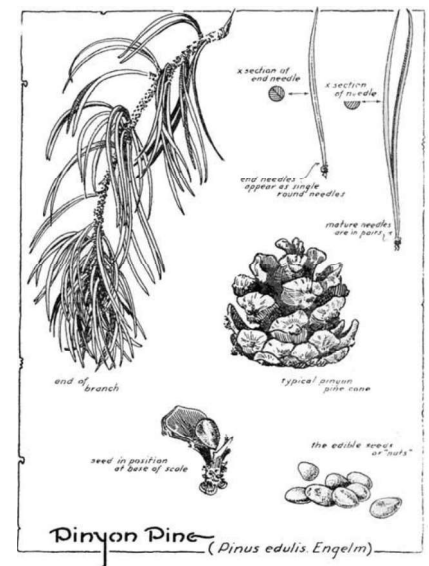
Ponderosa pine can be identified by their dark, yellow-green needles 13-25 cm long (5-10 in), which grow in clusters of two or three. Cones have a distinctive triangular barb. Their orange-brown bark forms long vertical plates. The tallest and most densely-packed stands of ponderosa pine are located in the northwestern end of ELMA. Like the Douglas-fir, ponderosa pine tend to grow in stunted form on the lava flows.



## Pinyon Pine

*Pinus edulis*

The state tree of New Mexico, pinyon pine trees have stiff, dark green needles which grow in bundles of two and are ~3 cm (1.2 in) long. The cones are rounded and about as long as the needles. They contain nut-like seeds, covered in a thin shell. These are edible (and delicious) and are eaten and traded between Native American tribes. These are also a food source to small mammals in ELMA.



## Fauna

The trees found on the Zuni-Bandera lava field provided cover and protections for animals and animals can feed on the browse. More than 50 species of mammals have been found in the ELMA. In the summer deer, elk and turkey can be found in ELMA. In the winter, deer can still be found in the lower-elevation pinyon-juniper type regions. Twelve species of bats have been identified in the national monument. The El Calderon and Braided Bat Caves, have been closed at



various points in the history of their management in an effort to slow the westward progression of white-nose syndrome (left). This disease is caused by the fungus, *Pseudogymnoascus destructans* (far left), which can be transported into caves on the shoes of visitors. It grows on the faces of the bats, increasing the time they spend awake during hibernation, depleting their fat reserves and leading to starvation. It can also damage their wings and other thin membranes, leading to dehydration. Other cave biota can be negatively affected by surface runoff, which transports pesticides, nitrates and petrochemicals from roads and nearby farming to the caves. Stream channels originate outside the lava field but can flow into the lava tube system.

## Humans

The first humans to inhabit the area around the Zuni-Bandera Volcanic Fields lived in the Paleo-Indian period of 10,000 to 5,500 years ago. The land covered by ELMA is the indigenous land of two tribes - the Zuni Pueblo to the west and the Acoma Pueblo to the east. The Zuni people have lived in this region for 3-4,000 years, establishing irrigated agriculture and raising livestock. They live in the mountains to the west, hunting there and in northern plains. They also historically used the land around the Bandera Ice Caves. Success as a desert agri-economy is due to careful management, conservation of resource and the maintenance of a complex social web. For some Zuni's, this is supplemented by the sale of arts and crafts. The Zuni Pueblo hosts the A:shiwi A:wam Museum and Heritage Center. The Acoma Pueblo were established in this region by at least the 11<sup>th</sup> century. Acoma people used kipukas for cattle and sheep. Analysis of pottery shards found in ELMA suggests trade relationships with other tribes.



Figure 3. Examples of the type of pottery found at ELMA, which are made by tribes located elsewhere and are an indication of trading. Left: White Mountain Redware (prehistoric Anasazi/Mogollon). Center: Socorro Black-On-White (storage jar, ~1100 - 1250 CE). Right: Mongollon Brown Ware (St. Johns Bowl 1175-1300 CE)

## References

- Inelson, D. (2004, February 1) Nature Program. <http://www.davidinelson.md/Cazadero/DouglasFir.htm>
- Jones, M. Scientific Illustration. <https://scientificillustration.tumblr.com/post/15890283473/rubus-ursinus-common-name-douglas-fir>
- KellerLynn, K. 2012. El Malpais National Monument: geologic resources inventory report. Natural Resource Report NPS/NRSS/GRD/NRR—2012/578. National Park Service, Fort Collins, Colorado.
- Muldavin, E., Y. et al. (2013). Vegetation Classification and Map: El Malpais National Monument. Natural Resource Technical Report NPS/SPCN/NRTR—2013/803. National Park Service, Fort Collins, Colorado.
- Pueblo of Zuni <http://www.ashiwi.org/>
- Schellbach III., L. (1933, December) Grand Canyon Nature Notes [http://npshistory.com/nature\\_notes/grca/vol8-9c.htm](http://npshistory.com/nature_notes/grca/vol8-9c.htm)
- United States Bureau of Chemistry and Soils and United States. Bureau of Plant Industry and United States. Bureau of Plant Industry, Soils, and Agricultural Engineering and United States. Soil Conservation Service and United States. Natural Resources Conservation Service. (1967). *Soil Survey*. U.S. Dept. of Agriculture

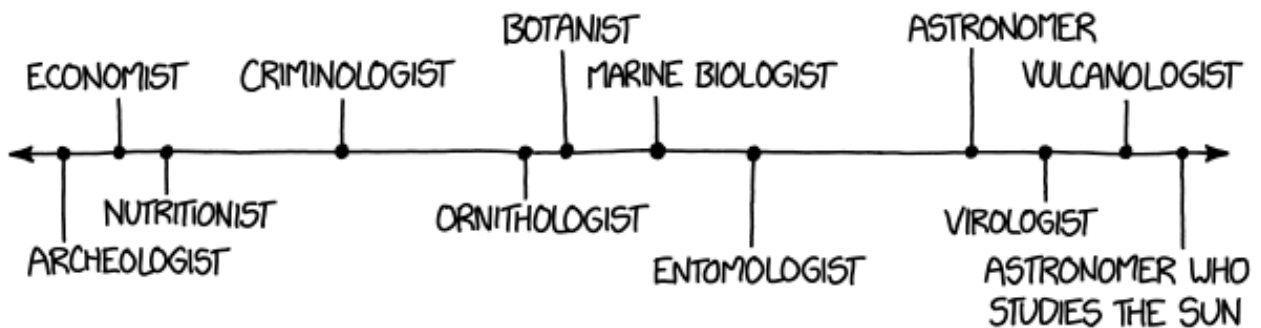
The author would be grateful to the authors of the National Park Service's Vegetation Classification and Map: El Malpais National Monument, which was particularly useful in producing this report.

## SHARING IS FUN!



HOW WORRIED YOU SHOULD BE IF YOU SEE LOCAL REPORTERS INTERVIEWING SCIENTISTS ABOUT A BREAKING NEWS STORY, BY FIELD:

MORE WORRIED →



# Ground Penetrating Radar Investigations of the Zuni-Bandera Volcanic Field

Emileigh Shoemaker, Indujaa Ganesh, Joana Voigt, John Noonan

## 1 Motivation

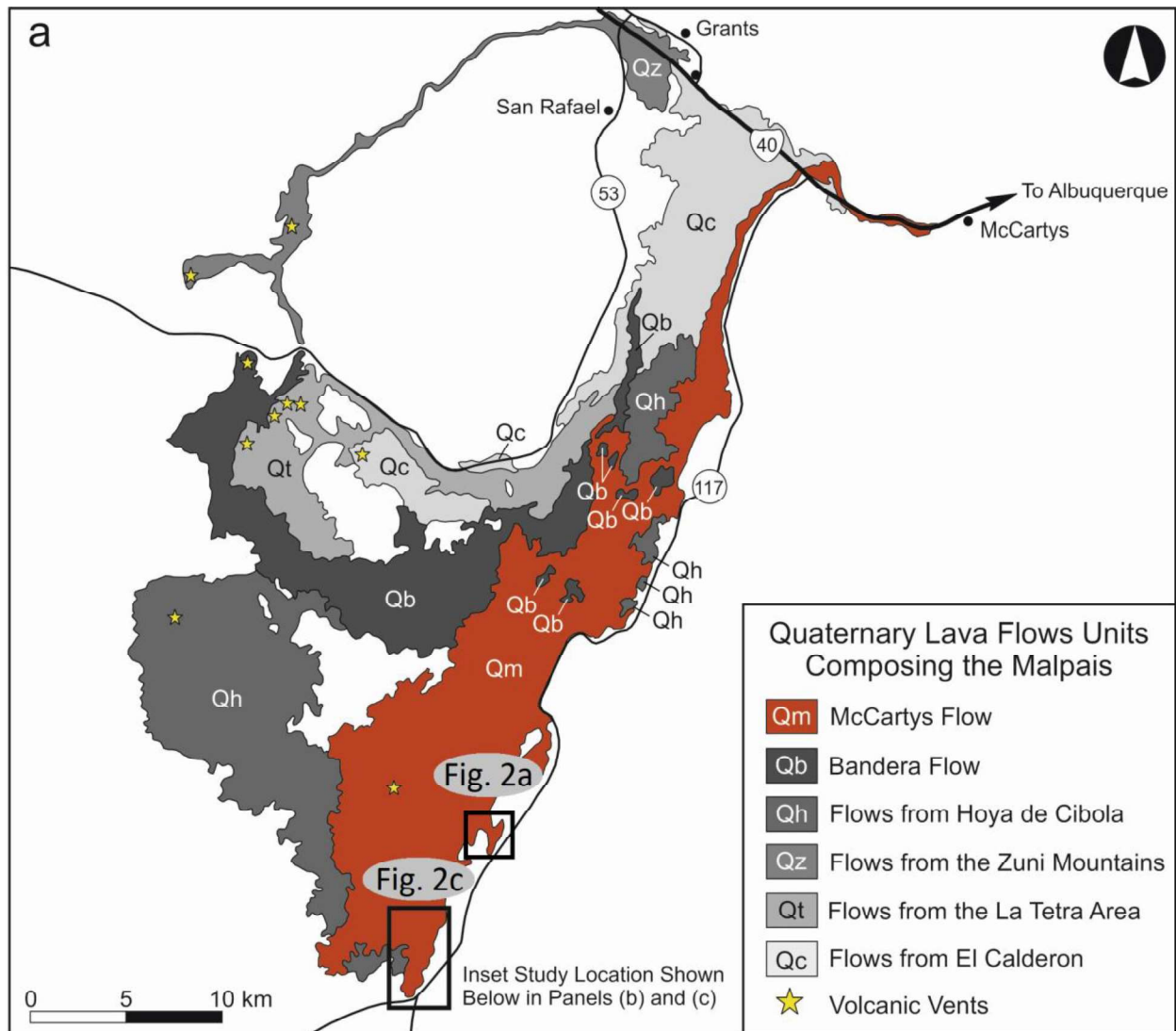
The SHARAD (SHAllow RADar) and MARSIS (Mars Advanced Radar for Subsurface and Ionospheric Sounding) orbital sounding radar systems onboard the NASA Mars Reconnaissance Orbiter (MRO) and ESA Mars Express orbiter detect many subsurface interfaces in volcanic terrains on Mars (Carter et al., 2009; Morgan et al., 2013; Simon et al., 2014; Voigt & Hamilton, 2018; Ganesh et al., 2019; Shoemaker et al., 2019). In cases where emplaced lava flows and other volcanic materials are visible in topography data, a thickness can be determined. The composition can thus be determined using the relationship between the thickness and the real dielectric constant,  $\epsilon'$ , of the medium through which the radar wave propagates given by Equation (1)

$$\epsilon' = \left( \frac{c\Delta t}{2h} \right)^2 \quad (1)$$

where  $\Delta t$  is the round-trip travel time of the radar wave traveling through the subsurface and returning to the spacecraft,  $h$  is the thickness of the material, and  $c$  is the speed of light in a vacuum. In most cases, there is not sufficient topographic relief of the emplaced materials to determine their thickness. Thus interpretation of subsurface stratigraphy from such reflectors becomes much more difficult from orbit. Earth boasts a variety of volcanic fields such as the Zuni-Bandera Volcanic Field, the subject of this investigation, which act as excellent planetary analogs both in composition and eruption style for terrestrial worlds like Mars. Investigation of the varying stratigraphy of lava fields available on Earth and documenting responses by ground penetrating radar (GPR) systems will assist in the geologic interpretation of orbital radar data. In this investigation, we will study three sites within the flow field, each with unique stratigraphies. The general geologic context of the Zuni-Bandera Volcanic Field can be found in Section 2 followed by a detailed description of our regions of interest in Section 3 and a description of GPR techniques and past investigations in Section 4.

## 2 Geologic Context of the Zuni-Bandera Volcanic Field

The Zuni-Bandera volcanic field, located south of the town of Grants in central-western New Mexico, comprises ~100 identified volcanoes. These volcanoes, located along the Jemez lineament, were active within the past 16 Ma with the most recent activity constrained to 700-3000 years ago. Within this field, originating southwest of the Rio San Jose, and occupying a valley east of Grants is the McCartys flow (Figure 1). Radiocarbon dating of charcoal samples collected from underneath the flow records an age of 3160-3200 yrs. Contrastingly, He dating performed on samples from the flow top suggests a younger age of  $2450 \pm 1200$  yrs. Cl cosmogenic dating done for all the flows within the Zuni-Bandera field provided an older age of  $3900 \pm 1200$  years for the McCartys field. These studies place the age of the McCartys flow between 2500 and 3900 years, making it the youngest flow in the Zuni-Bandera volcanic field.



**Figure 1.** Map of the Zuni-Bandera field with the study area marked by a hollow black rectangle. The southernmost yellow star shows the location of the McCartys vent. Image slightly modified from Hamilton et al., in review.

This 48 km long basaltic flow extends over an area of ~305 sq. km, and has an estimated volume of ~6.9 cu. km. The flow was emplaced on top of Holocene alluvial sediments and other flows of the Zuni-Bandera field, specifically the Hoya de Cibola flow to the South, and the Hoya de Cibola and Bandera flows to the North. The origin of the flow, marked by a yellow star in Figure 1, lies in a broad valley between mesas 37 km south of the intersection of interstate 40 and NM 117. The vent that sourced the McCartys flow is now occupied by a cinder cone that rises ~8 m above a low, broad shield morphology of the flow field. Lava that was erupted from this vent flowed northeast for 40 km to the San Jose valley along existing drainage paths, and then turned eastward and flowed down the valley for another ~10 km, finally terminating near the town of McCartys. Some of the lava also flowed southwest of the vent for 8-10 km over and around the Hoya de Cibola flows and onto Holocene alluvial plains. Our study area, shown in Figure 1, is located within this southwest part of the flow.

The McCartys flow was initially emplaced at high effusion rates (which decreased with time) as thin lobes which eventually integrated to form a large sheet-lobe flow. Linear flow structures on top of the flows preserve the record of high early effusion rates. Evidence for the early emplacement process can be seen in the form of structures at the contacts/boundaries between initial lobes and kinematic markers on the flow surface which are mis-oriented from the overall flow direction caused by rotation of the outer surfaces from the initial direction of emplacement. The Hoya de Cibola flow also exhibits similar structures. Several volcanic features of interest such as lava rise plateaus, inflation pits, tubes, lava wedges, of interest and squeeze-ups are preserved within this relatively young and unweathered pahoehoe flow.

### 3 Field Objectives

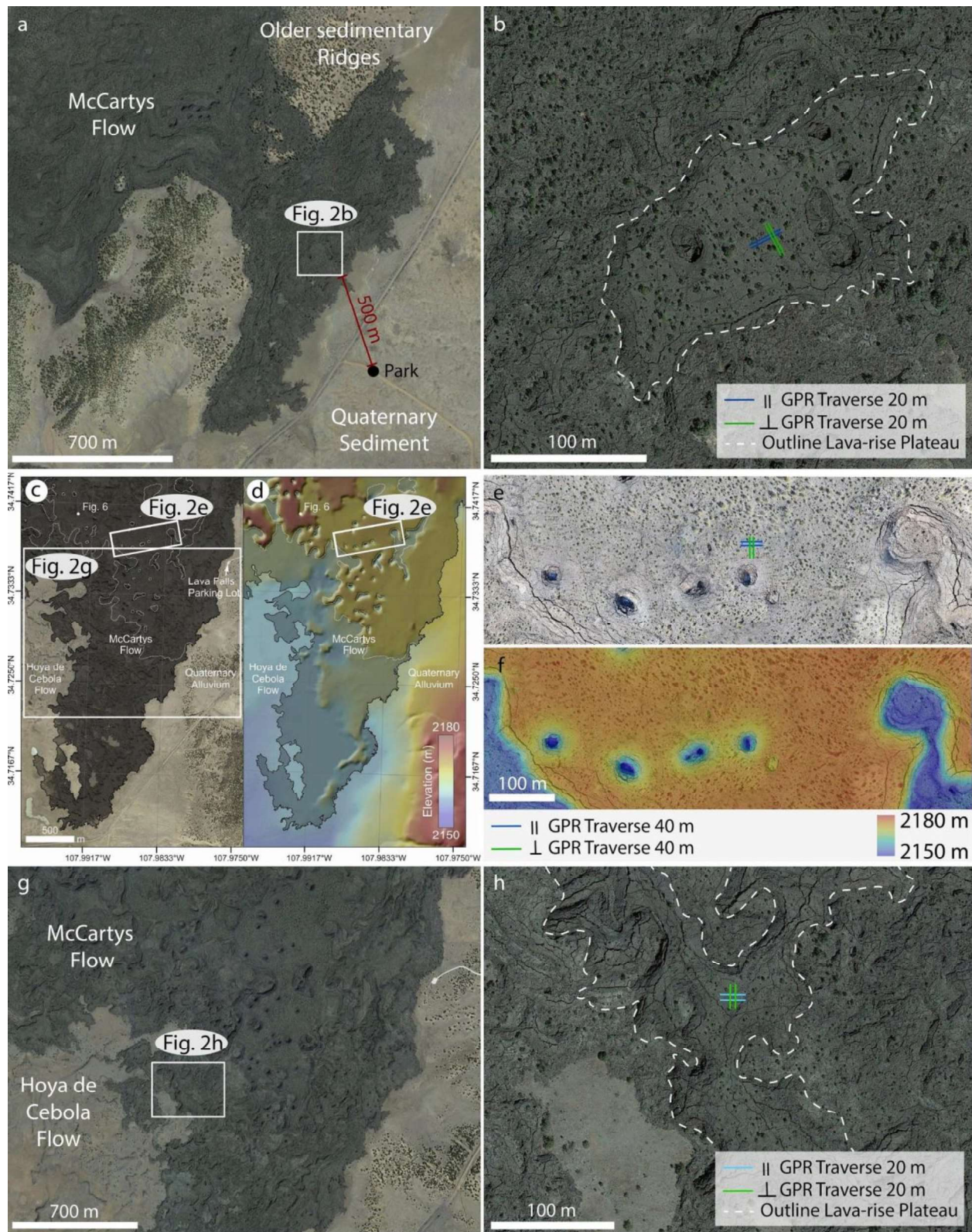
Our field investigation of the Zuni-Bandera Volcanic Field using GPR will visit three sites, each of which possesses a different stratigraphy (see table 1 for the expected geological contacts). Two of the sites have a known stratigraphy. At each site, four GPR transects are planned with length of 20 m (site 1 and 3) and 40 m (site 2). This study will perform two GPR transects parallel to one another and two will be perpendicular to them to get a better three-dimensional understanding of the underlying terrain.

The first study site is located on the eastern margin of the McCartys flow field (see inset in Figure 1). At this site the McCartys lava rests on top of a layer of Quaternary sediment (Fig. 2a and b). An older sedimentary ridge confined the lava which can be seen in the central part of Figure 2 a and branches out towards the flow front forming a “Hammer head” shape (right handside of Fig.

2a). The study site itself is located in the central part of a flat-topped higher-elevated area, that represents a lava-rise plateau. The second study site is located to the west (Fig. 2 c) where the McCartys flow overlies the older lava flow field, Hoya de Cebola (Fig. 2 g). The GPR transects will be 20 m in length and are located on a flat-lying higher-standing lobe. The final site is within the inner part of the McCartys flow field (Fig. c to f for exact location). In this study the McCartys flow buries the underlying geology and thus the stratigraphy is unknown. Based on the geological map shown in Figure 1 the eastern flow front of the older underlying Hoya de Cebola could be inferred to be present in that area.

**Table 1.** summarizes the main parameters of all three investigation sites, including: location, expected geological contacts, GPR track lengths, elevation of the planned study sites versus the elevation of the surrounding of the lava flow, and estimated flow thicknesses.

Study Site	GPS location	Geological Contact	GPR Traverse length [m]	Elevation Flow vs. surrounding [m]	Flow thickness [m]
Hammer Head	34°46'57.59" N 107°56'31.69" W	McCartys - Quaternary Sediment	20	2173 2164	9
Flow Interior	34°44'19.39" N 107°59'06.71" W	McCartys - uncertain: Quaternary Sediment or Hoya de Cebola Flow	40	2180 2161	19
Flow Margin	34°43'52.22" N 107°59'30.74" W	McCartys - Hoya de Cebola Flow	20	2169 2161	8



**Figure 2.** Gives an overview of all three investigation sites. The outlines of panel a) and c) are shown in Figure 1. a) The “Hammer Head” study site; the McCartys lava flow is in contact with quaternary sediment. b) Close-up to the higher-elevated terrain, plateau that is also shown with the dashed white lines. Within



the plateau the planned four GPR traverses are shown. c) and d) Modified version from Hamilton et al., in review. c) orthoimages from the southern part of the McCartys lava flow-field, resting on the older Hoya de Cebola in the west and quaternary Alluvium in the east. Outline of panel e), f), and g) are shown with the white boxes. Panel e) and f) are a close-up to the study site 2. Orthoimage in the e) panel include the planned GPR traverses and respective digital terrain model in panel f). Both images are from Hamilton et al., in review. Panel g) gives an overview of the third study site with a close-up the inflated lobe in h), which is outlined with a white dashed line.

### *Planned Schedule*

#### Day 1: study site “Hammer Head”

- Walk from parking place (500 m) to lava flow margin: ~ 20 min.
- Description of sedimentary layer at flow margin: ~ 30 min.
- Walk to study site (50 m on lava): ~ 10 min.
- Set-up of equipment at study site: ~ 20 min.
- Run one Traverse: ~ 30 min.  
=> total of four traverse: ~2 h; use time to describe lava
- Pack equipment: ~ 20 min.
- Hike back: ~ 30 min.  
Total time: ~ 4 h 20 min.

#### Day 2: study sites “Flow Interior” and “Flow Margin”

- Walk from parking place (50 m) to lava flow margin: ~ 5 min.
- Description of sedimentary layer at flow margin: ~ 20 min.
- Walk to study site (850 m on lava): ~ 30 min.
- Set-up of equipment at study site: ~ 20 min.
- Run one Traverse: ~ 30 min.  
=> total of four traverse: ~2 h; use time to describe lava
- Pack equipment: ~ 20 min.
  
- Hike to study site 3 (1 km on lava): ~ 45 min.
- Set-up of equipment at study site: ~ 20 min.
- Run one Traverse: ~ 30 min.  
=> total of four traverse: ~2 h; use time to describe lava
- Pack equipment: ~ 20 min.
- Hike back (1.5 km on lava or 5 km along the margin): ~ 60 min  
Total time: ~ 8 h

## 4 Methodology

Ground Penetrating Radar (GPR) provides physical properties of materials by receiving a reflected radar signal along a ground track, the path the instrument takes over the landform of interest. An excellent review of the process is described in Davis and Annan 1989, and a brief summary of the physics is presented here. The process for using GPR to determine stratigraphy of a field site follows.

### *Physics of Ground Penetrating Radar*

An electromagnetic wave between 10-1000 MHz is emitted by the GPR, which penetrates the ground below, propagating at a velocity dictated by the material's electric properties, which in turn is determined by both the geophysical parameters and ground mineralogy (Annan and Davis, 1976; Jensen 2009). The depth to which the wave is capable of reaching with an intensity large enough to allow measurement of the reflection is dependent on several factors. First, the frequency of the GPR largely determines the effective depth to which measurements can be made. Longer wavelength (lower frequency) radar is capable of penetrating deeper through the medium, but loses spatial resolution in the process (Annan and Davis, 1976). Secondly, the volume scattering of the medium reduces the reflection and subsequently limits the effective depth of measurements (Davis and Annan, 1989). Thirdly, the electric properties, which are dictated by the mineralogy, density, and water content, strongly affect the depth of measurement (Olheoft 1998). For materials that have a low conductivity, like the porous results of volcanic activity in the form of dry ash and cinders, GPR is capable of penetrating 20 meters at 400 Hz (Heggy et al. 2007). The reflected signal allows determination of depth of boundary layers that indicate a change in dielectric constant, which provides constraints on the material that the radio wave propagates through as well as highlight layering, fracturing, and any large scale (~ 1 meter) porosity. Without a reflection off of a boundary layer the permittivity of the material cannot be determined. When proposed in the 1970's it was intended for Earth-based geological analysis but has been recently adapted for general purpose planetary geology.

### *Previous Investigations of Lava Flows using Ground Penetrating Radar*

Instrument development for planetary missions has seen GPR flown on missions like NASA's Mars Reconnaissance Orbiter (MRO) and the European Space Agency's Mars Express in the form of the SHARAD and MARSIS instruments, respectively. Each instrument has been incredibly successful in their operations, but here we focus specifically on measurements of lava flows. SHARAD measurements from ground tracks over Amazonis Planitia placed constraints on the material properties of Vastitas Borealis formation (Campbell et al. 2008), showing lava flow and/or sediment deposits below a dust mantle. The observed subsurface reflector could be explained by a sharp contrast in density (i.e. lava flow to sediment), or from the presence of a soil layer bifurcating

two deposits of similar dielectric constants. Ground tracks from SHARAD over the Tharsis region were able to determine that lava flows in the region were sourced from rift zone volcanoes and that all lava flows were of similar bulk density (Simon et al. 2014). More specifically, the measurements of lava flow dielectric constants from SHARAD are able to discern that the likely dust covering these flows lowers the permittivity gradient as the wave propagates, in turn allowing a larger than expected signal to pass into the high-permittivity lava flow (Carter et al. 2009). Additional Earth-based radar observations using the Arecibo Observatory as a transmitter and the Green Bank Telescope as a receiver has provided measurements of lunar lava flows as well, showing the presence of large (decimeter) subsurface rocks (Campbell et al. 2009). However, orbital GPR measurements require a significant database of Earth-analog field sites to compare to in order to accurately interpret the remote sensing data.

The plethora of terrestrial analog field sites available for high spatial resolution mapping has provided researchers with the opportunity to explore the reflection signatures of different lava flow structures and volcanic deposits. The research done on Mars geophysical analogs was initiated by Grimm et al. 2006, Heggy et al 2006a, Heggy et al. 2006b, and Khan et al. 2007 at several different locations in the American West. Grimm et al. 2006 focuses on the Bishop Tuff in California, Heggy et al. 2006a and Khan et al. 2007 on lava flows in Craters of the Moon National Monument, and Heggy et al. 2006b on buried volcanic features in the Amargosa Desert of Nevada. These studies also are particularly interested in the loss mechanisms for relatively low frequency GPR, below 100 Hz, which is capable of penetrating 10's of meters into the subsurface, depending on the conductivity and stratigraphy of the geological features. Higher frequency GPR, in the 100-900 MHz range, has been carried out for Mars analog environments as well (Paillou et al. 2001, Grant et al. 2004), but only for a single volcanic field site located in Djibouti with relatively low penetration due to high conductivity. The high-iron content of some lava flows substantially raises the conductivity, limiting the effective depth of GPR. Most critically, Paillou et al. 2001 combines measurements of the lava flow's physical properties with x-ray crystallography of samples taken from the site, allowing correlation of signal with mineralogy. More recent work has focused on the effectiveness of using GPR to detect lava tubes (Miyamoto et al. 2005, Rowell et al. 2010), and was successful to depths of 10m, often similar in depth to the lava flow itself. The lava flows at their sites on Mt. Fuji and in Craters of the Moon are pahoehoe flows, similar to those of the Zuni - Bandera volcanic field. Understanding the structure and radar response of Earth-analog lava flows and tubes at an abundance of sites with high spatial resolution GPR will provide the context dataset needed to identify similar features more successfully in MARSIS and SHARAD orbital observations on Mars.

### *An Introduction to the Ground Penetrating Radar System*

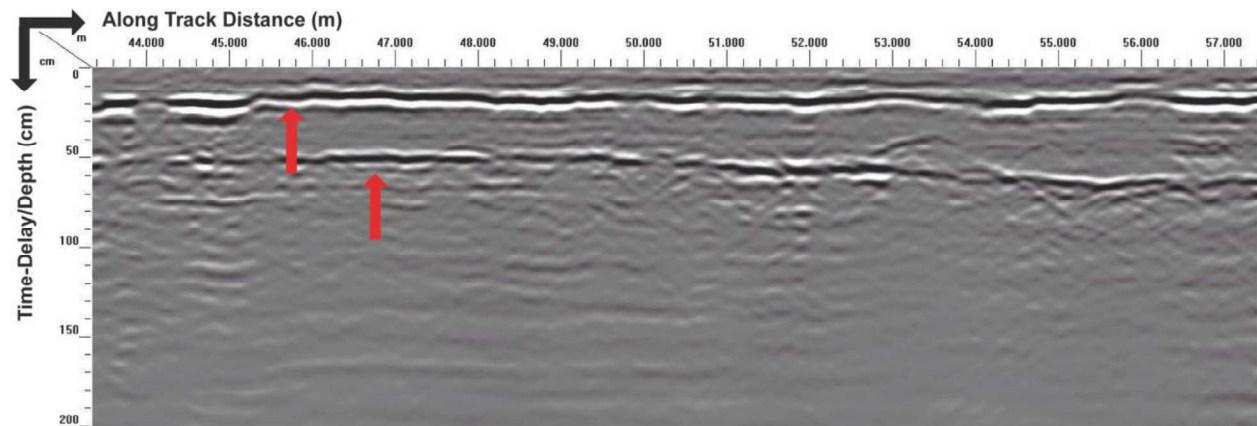
The investigation of the flows in the Zuni-Bandera volcanic field will be conducted using two antennas and a controller manufactured by Geophysical Survey System Inc. (GSSI). The SIR4000 handheld controller system is capable of connecting to both digital and analog antennas as well as integrating GPS. The two antennas that will be used in this investigation are a 200 MHz antenna and a digital 350 MHz HS (HyperStacking) antenna. The digital antenna uses stacking, which is essentially averaging over many scans in order to improve the resolution of the data. A typical depth range for the 200 MHz antenna is between 7 and 12 m while the 350 MHz antenna has a depth range between 6 and 12 m. We will integrate a Trimble Geo7x Handheld GPS system into the GPR setup. The GPS connects directly to the GPR controller and tracks each transect in real time, outputting the radar image along with the GPS information upon downloading. An example of the setup is shown in Figure 3. Both antennas are operated similar to this example.



**Figure 3.** Example of the GSSI GPR setup. The 200 MHz antenna (orange box) is pulled by a strap connected to the box itself with a calibrated survey wheel attached to measure distances. The Trimble Geo7x GPS is attached to the survey wheel mount. One person pulls the antenna forward while the other walks behind holding the controller and monitoring the output in real-time.

### Data Acquisition

The transects conducted will be those described in Section 3. A tape measure will be laid down to measure the length of the transect with survey flags placed at each endpoint. Each transect will be conducted in pairs, with one person pulling the antenna, carefully keeping the radar antenna coupled to the surface while the other person is operating the controller and monitoring the output in real time as the GPR moves across the surface. Data will be collected in what is termed “distance mode” by the GSSI system which is not dependent upon the speed at which the team pulls the antenna. Distances are measured by the system using a calibrated survey wheel which is mounted to the antenna. Each transect will be between 10 and 50 m in length. The location of the survey flags will be recorded by the GPS in addition to the along-transect tracking. As the GPR moves along the surface, pulses at the frequency of the antenna are sent into the subsurface. When a pulse reaches a layer of sufficient dielectric contrast, a bright return can be seen in the radargram at the location of that interface. A representative radargram can be seen in Figure 4.



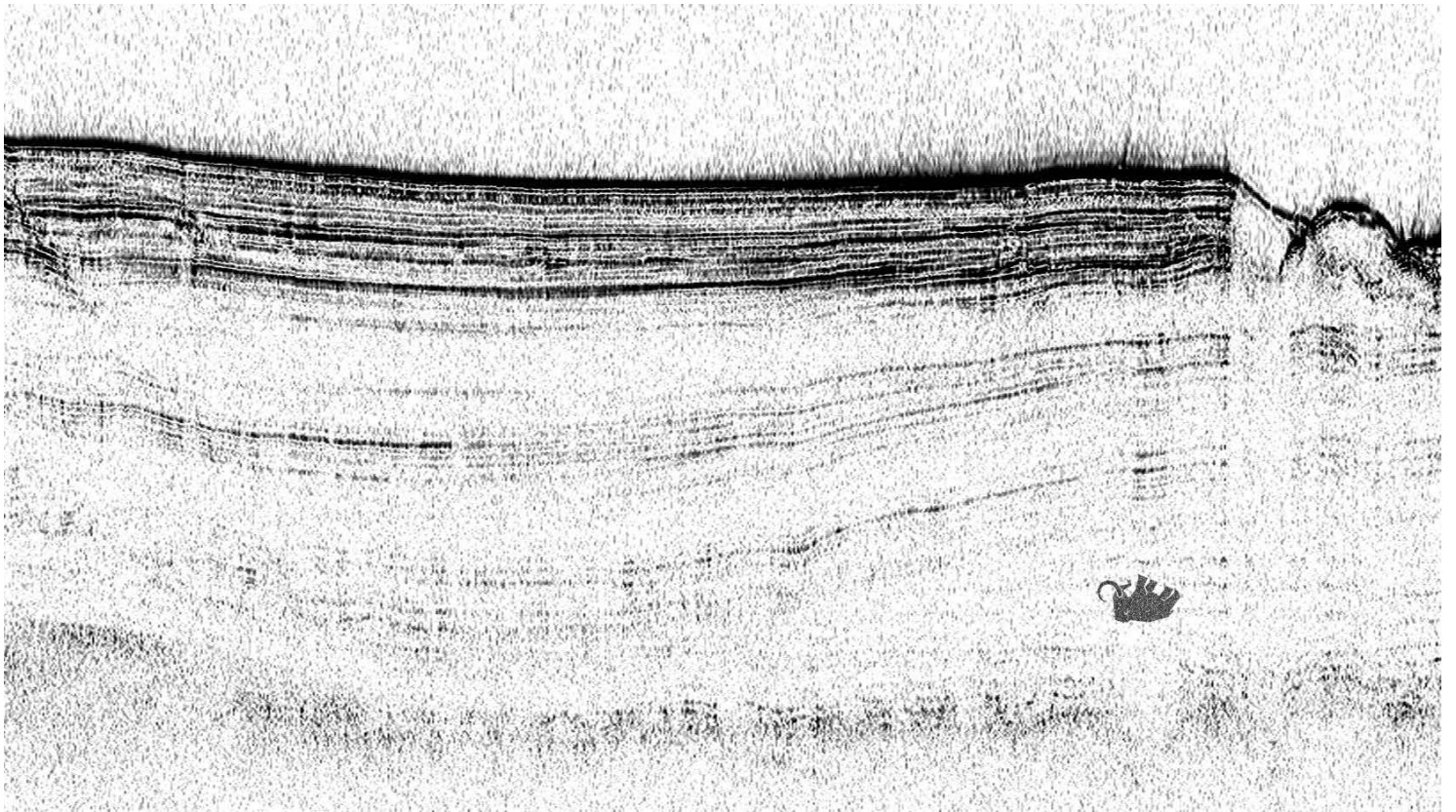
**Figure 4.** Example of a radargram output by the GSSI system. Along track distance increases along the x-direction and time-delay or depth increases in the negative y-direction with the surface at 0 cm. Red arrows indicate two subsurface interfaces, or reflectors, that span the entire visible portion of the radargram. There is a significant contrast in the dielectric constant between each layer creating the two bright, well-defined, linear reflectors.

Radargrams are generated in real-time as the user is operating the controller. The dielectric constant can be assumed to convert time-delay into depth for viewing. For volcanic materials such as Lunar and Terrestrial basalts, dielectrics between 7 and 11 are reasonable (Carter et al., 2009) while more porous or less-dense materials such as sediments or pyroclasts require an assumption of a much lower dielectric. We will assume a dielectric constant reasonable for basalts for this investigation. After the data are collected, they will be exported into the GSSI RADAN 7™ software package in order to be processed and interpreted. All radar transects and GPS information will be imported into a GIS software program for additional post field-trip analysis.

## References

- Annan, A. P., and J. L. Davis. "Impulse radar sounding in permafrost." *Radio Science* 11.4 (1976): 383-394.
- Campbell, Bruce, et al. "SHARAD radar sounding of the Vastitas Borealis Formation in Amazonis Planitia." *Journal of Geophysical Research: Planets* 113.E12 (2008).
- Campbell, Bruce A., et al. "Rugged lava flows on the Moon revealed by Earth-based radar." *Geophysical Research Letters* 36.22 (2009).
- Carter, Lynn M., et al. "Dielectric properties of lava flows west of Ascraeus Mons, Mars." *Geophysical Research Letters* 36.23 (2009).
- Davis, J. L., and A. P. Annan. "GROUND-PENETRATING RADAR FOR HIGH-RESOLUTION MAPPING OF SOIL AND ROCK STRATIGRAPHY 1." *Geophysical prospecting* 37.5 (1989): 531-551.
- Ganesh, I., et al. "SHARAD Mapping of the Caldera of Arsia Mons." *50th Lunar and Planetary Science Conference, abstr. #1859*, (2019).
- Grant, J. A., et al. "Using ground penetrating radar to constrain the drainage evolution in southern Egypt and implications for future deployment on Mars." *AGU Spring Meeting Abstracts*. 2004.
- Grimm, Robert E., et al. "Absorption and scattering in ground-penetrating radar: Analysis of the Bishop Tuff." *Journal of Geophysical Research: Planets* 111.E6 (2006).
- Hamilton, Christopher W., et al. "Lava-rise plateaus and inflation pits in the McCartys lava 1 flow-field, New Mexico: An analog for pāhoehoe-like lava flows on planetary surfaces". In Review.
- Heggy, Essam, et al. "Ground-penetrating radar sounding in mafic lava flows: Assessing attenuation and scattering losses in Mars-analog volcanic terrains." *Journal of Geophysical Research: Planets* 111.E6 (2006a).
- Heggy, Essam, et al. "Low-frequency radar sounding investigations of the North Amargosa Desert, Nevada: A potential analog of conductive subsurface environments on Mars." *Journal of Geophysical Research: Planets* 111.E6 (2006b).
- Heggy, E., et al. "Mapping structural elements in volcanic terrain using multiple frequencies and polarimetric ground penetrating radar: Analogy to the Martian case" EGU General Assembly, abs. 09049. (2007)
- Jensen, John R. *Remote sensing of the environment: An earth resource perspective 2/e*. Pearson Education India, 2009.
- Khan, Shuhab D., Essam Heggy, and Jaime Fernandez. "Mapping exposed and buried lava flows using synthetic aperture and ground-penetrating radar in Craters of the Moon lava field." *Geophysics* 72.6 (2007): B161-B174.
- Miyamoto, Hideaki, et al. "Mapping the structure and depth of lava tubes using ground penetrating radar." *Geophysical research letters* 32.21 (2005).

- Morgan, G. A., et al. "3D Reconstruction of the Source and Scale of Buried Young Flood Channels on Mars." *Science*, 340.6132 (2013):607–610.
- Nichols, R. L. "McCartys basalt flow, Valencia Country, New Mexico." *Geological Society of America Bulletin*, 57(11), 1049–1086. (1946).
- Olhoeft, Gary R. "Ground penetrating radar on Mars: 7th International Conference on GPR." *The Univ. of Kansas* (1998): 387-392.
- Paillou, Ph, et al. "Performances of ground penetrating radars in arid volcanic regions: Consequences for Mars subsurface exploration." *Geophysical Research Letters* 28.5 (2001): 911-914.
- Rowell, Colin R., et al. "Characterization of lava tubes using ground penetrating radar at Craters of the Moon National Monument, USA." *Tech. rep. CREWES Research Report 22* (2010): 1-18.
- Shoemaker, E. S., et al. "Radar Sounding of Lava Flows in the Tharsis Province, Mars." *50th Lunar and Planetary Science Conference, abstr. #2611* (2019).
- Simon, Molly N., et al. "Studies of lava flows in the Tharsis region of Mars using SHARAD." *Journal of Geophysical Research: Planets* 119.11 (2014): 2291-2299.
- Voigt, J. R. C., and Hamilton, C. W., "Investigating the volcanic versus aqueous origin of the surficial deposits in Eastern Elysium Planitia, Mars." *Icarus* 309 (2018): 389–410.





## Ground Penetrating Radar Investigations of Lava Tubes

Michael Christoffersen, Nicole Bardabelias, Brandon Tober

### Ground Penetrating Radar Fundamentals

Ground penetrating radar (GPR) is a geophysical technique that uses radio-frequency electromagnetic radiation to image the subsurface. GPR is an active source geophysical method - a transmitter sends out a signal that is reflected by electrical contrasts in the subsurface and then detected by a receiver.

There are several types of GPR surveys, the most popular for surface based work are common offset and common midpoint surveys. In a common offset survey, the transmitter and receiver are maintained a constant distance apart and translated along a survey line, creating a record of reflectors in the subsurface along that line. Figure 1 shows a standard geometry for a common offset survey. In a common midpoint survey, the transmitter and receiver are moved apart at a constant speed, maintaining the same midpoint. A common midpoint survey allows estimation of the subsurface velocity structure, but the results will be inaccurate in the presence of lateral velocity variations. Knowledge of subsurface velocities is very important for GPR. Raw GPR data is recorded as amplitude vs time - the velocity of the signal in the subsurface is necessary to convert time to depth.

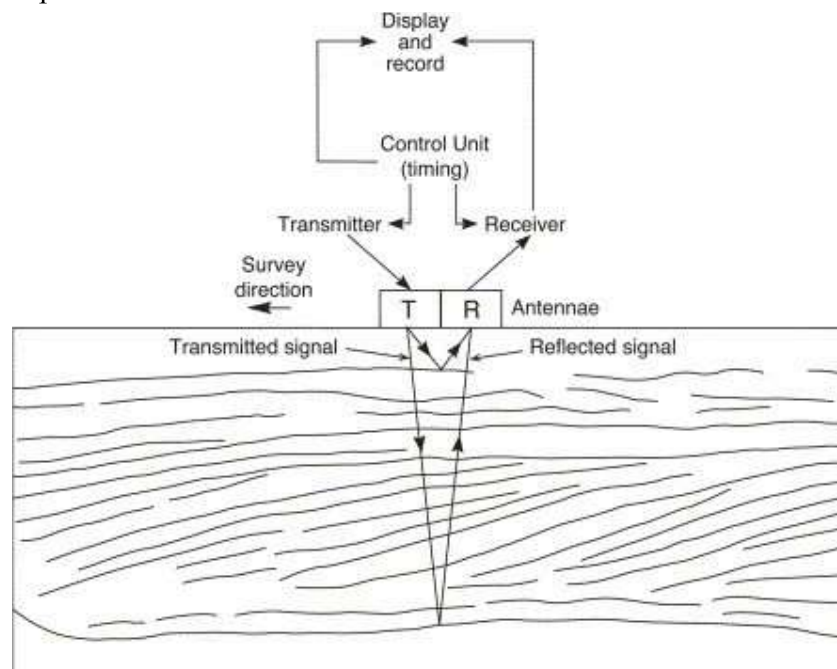


Figure 1. Illustration of a standard common offset survey meant to measure the time delay to reflectors in the subsurface. Source: Adrian Neal, University of Wolverhampton

Under specific conditions GPR can probe thousands of feet into the subsurface. However, most

geologic materials rapidly attenuate the GPR signal which limits the effective depth of the method. Frequency is a control on exploration depth as well, most of the time lower frequency signals are attenuated slower, allowing imaging of deeper reflectors. The trade-off is that using lower frequency signals lowers the resolution of the instrument. Common GPR frequencies for geologic purposes range from hundreds to single MHz. Figure 2 shows three different common offset GPR acquisitions over the same material at different frequencies.

There are several types of waveforms that can be emitted by GPRs. Most surface based geologic work uses an impulse type waveform where the transmitter generates a very short (single nanoseconds), powerful pulse that is fed into the transmit antenna. After the pulse is transmitted the receiver records for a set amount of time before another pulse is generated.

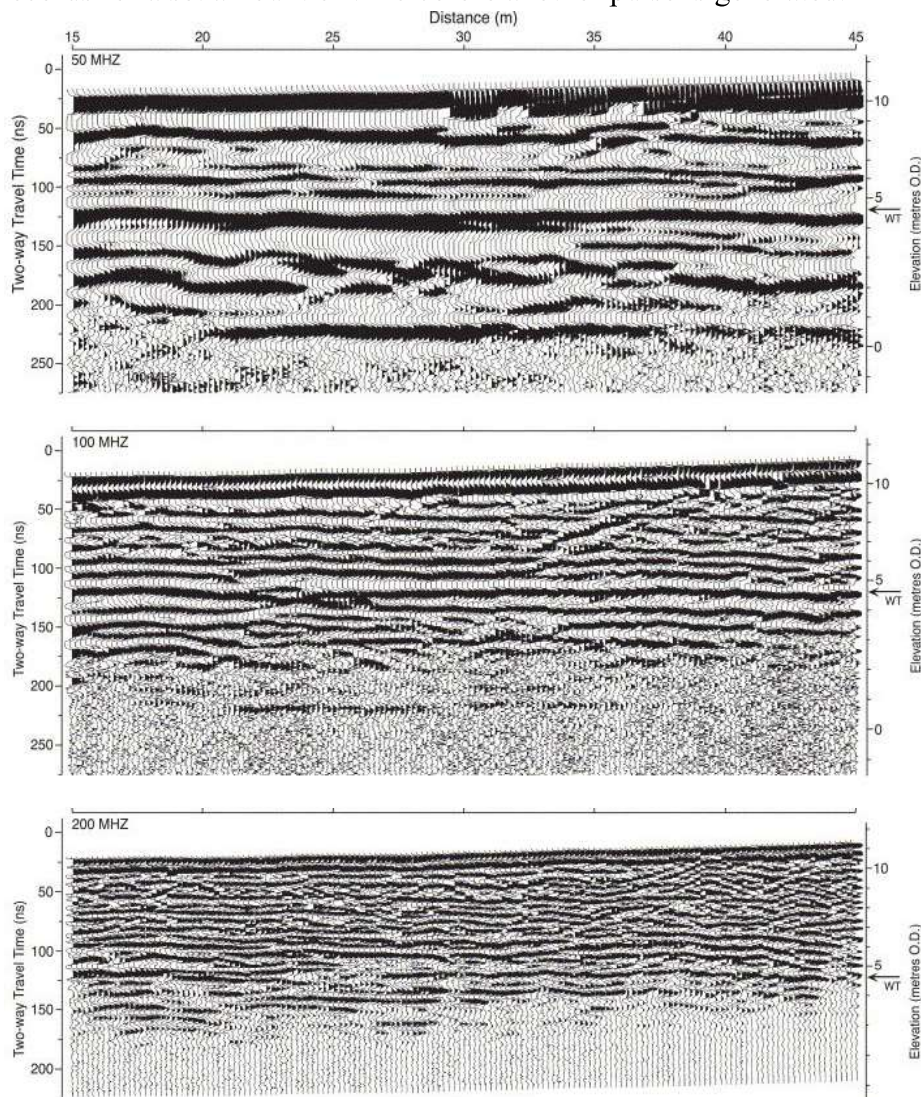


Figure 2: Three common offset surveys over the same material at 50, 100, and 200 MHz. The water table depth is labeled at “WT” on the depth axis in each wiggle trace radargram. Source: Adrian Neal, University of Wolverhampton

## Radar Applications of Lava Tubes

A lava tube is a tunnel-like structure formed beneath the surface of a lava flow through which subsequent flows can be transported (Miyamoto et al., 2005). They typically form in low-viscosity, channelized flows when exposed upper portions cool and solidify while lava continues moving underneath. These tubes thermally insulate the material flowing through it, allowing lava to travel long distances before beginning to crystallize. As the eruption rate slows, the lava level within the tube decreases, eventually partially or fully evacuating and creating a hollow tunnel.

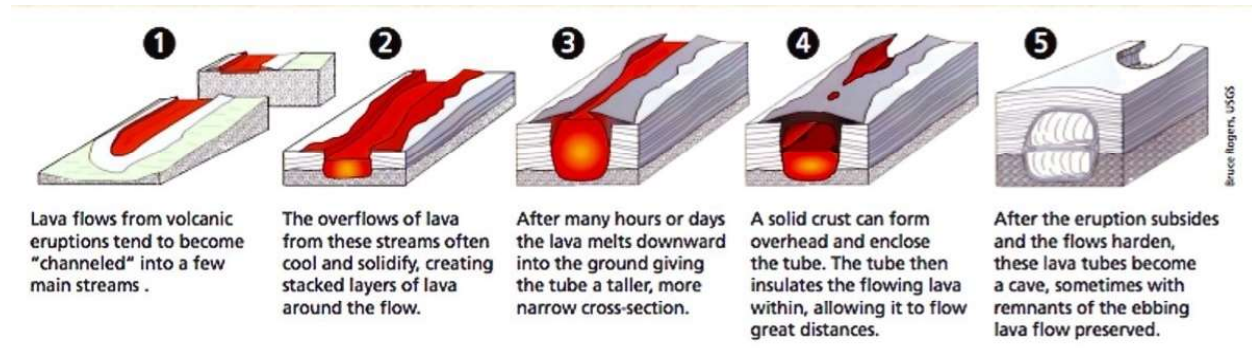


Figure 3: Graphic outlining one method of lava tube formation. A combination of lava overflow, which forms stacked walls around the flow, and mechanical erosion, which drives the base of the flow downwards, results in a tall, narrow channel. A solid crust can form at the surface, insulating the flow within and creating a lava tube (source: Bruce Rogers, United States Geologic Survey).

These tubes are often identified solely by surface features, which makes them difficult to identify in the field. Most surface expressions are the result of collapse: skylights are formed when a small section of the tube roof has collapsed, and large pits, sometimes present in adjacent "chains," point to a more extensive roof and wall collapse. Another example is a sinuous ridge, which indicates collapse of a long portion of the tube without a surface breach. However, without some form of collapse lava tubes generally leave no discernable trace at the surface. Other methods of identifying a lava tube include seismicity, magnetic field perturbations, and measuring low-frequency sounds; however, these three methods only apply to active lava tubes (Miyamoto et al., 2005). Unless a later field study or other methods can confirm the existence of a lava tube, the results of these methods are usually ambiguous.

GPR presents a unique solution to this problem, as it is a great way of detecting subsurface reflectors. The difference in permittivity between the roof of the lava tube, the air inside the tube, and the floor of the tube will give you a distinct echo pattern with which one could map the shape and extent of lava tubes or a lava tube network.

Lava tubes are also observed on the Moon, Mars, and Venus. This heat-efficient transport of lava provided by the long tubes makes it easier to emplace extensive lava flows seen on other terrestrial bodies, such as the lunar mare. The search for lava tubes on the Moon has been

ongoing since the Lunar Orbiter program in 1966, and the higher-resolution SELENE and LRO orbiters have mapped lava tubes thousands of kilometers long as collapse features known as “sinuous rilles” (Haruyama et al., 2009, see Figure 4). It is hypothesized that The Moon may host some of the longer lava tubes of the terrestrial bodies due its low gravity and low-viscosity basaltic flows (Keszthelyi, 1995). In addition, SELENE data has located a putative skylight in a known volcanic region on the Moon (Haruyama et al., 2009, see Figure 4). Lava tubes on Mars are often exposed as pit crater chains and are prevalent in the Tharsis region, and with higher-resolution image data a number of skylights have also been identified. Venus, which was heavily active both volcanically and tectonically, also exhibits collapse features that are interpreted to be either collapsed lava tubes or pit craters (Melville, 1994).

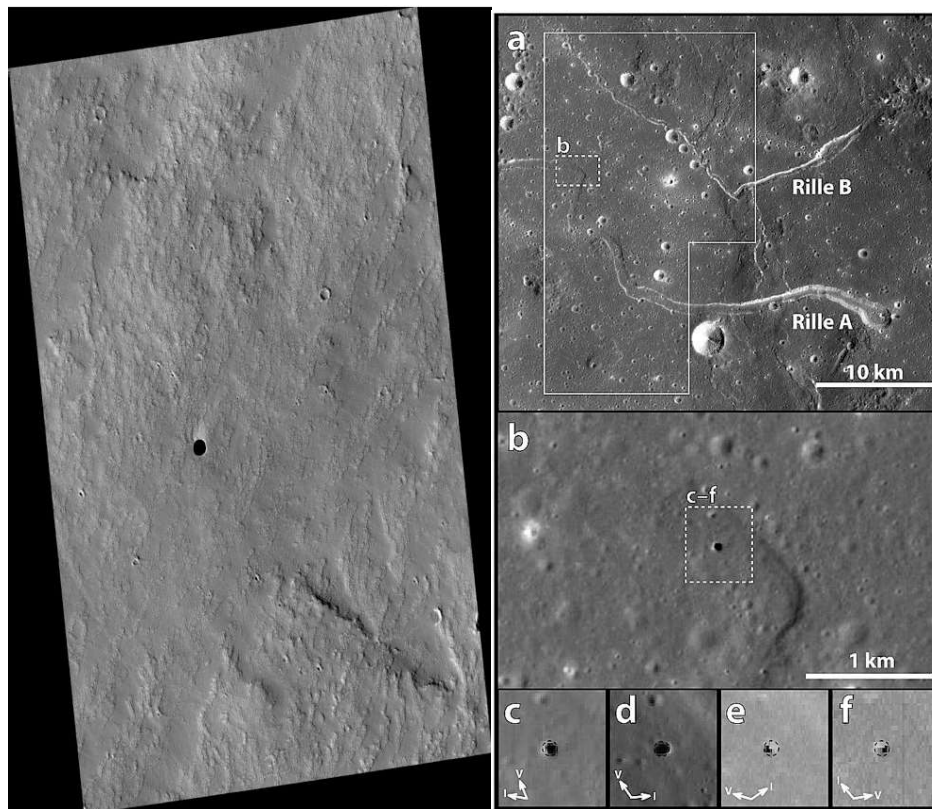


Figure 4: Comparison of potential skylights on both Mars and the Moon.

Left: HiRISE image PSP\_003647\_1745, “Candidate Cavern Entrance Northeast of Arsia Mons.” The dark spot is a potential skylight located in the Tharsis volcanic province. Note the lack of indicative surface expressions for this lava tube (source: NASA/JPL/University of Arizona).

Right: Figure 1 from Haruyama et al., 2009 showing a potential skylight in a known volcanic province on the Moon.

Image A gives the geologic context, highlighting nearby rilles which authors propose are collapsed lava tubes.

Image B shows the portion of the rille in which they found the putative skylight, and images C – F display the breach at different solar illuminations and view vectors.

For bodies with thin or no atmospheres, lava tubes provide shelter from the harsh surface radiation environment, diurnal temperature swings, and meteorite bombardment (Kaku et al., 2017). This is of geologic and astrobiological significance for studies of past habitability or

future human exploration: subsurface caverns may preserve biosignatures or volatiles which would make lava tubes an ideal exploration candidate for terrestrial bodies.

### PulsEKKO GPR System

Sensors and Software's pulseEKKO GPR system is well-suited for the goals of this research. Three sets of antennas are available for this work, operating at 50 MHz, 100 MHz, and 200 MHz (6 m, 3 m, and 1.5 m wavelengths, respectively). These may be used complementary in an effort to image the structure of lava tubes in the subsurface.

Antennas are directly mounted to both the transmitter and receiver. The transmitter and receiver are then connected via fiber optic cables to the DVL-500 control module. The GPS antenna is also connected to the control module. System parameters are set via the control module prior to data acquisition. Users can specify parameters such as the survey type (ie. Common Midpoint (CMP) or Common Offset), antenna frequency, antenna separation, antenna orientation, survey step size, recording time window, and stacking. On rough terrain, two users are typically required – one operating as the transmitter, while the other operates as the receiver and data logger. Both antennas are mounted to handles which the operators can move along the survey line at the desired step size (fig. 5). While performing a common offset survey on smooth terrain, the PulsEKKO SmartCart can be utilized, allowing for more efficient data acquisition.

Common offset surveying will initially be utilized to allow for mapping of any potential subsurface reflectors. Areas where reflectors are seen may then be revisited by a CMP survey in an effort to constrain the velocity of the layer atop such reflectors (Fig. 5). With a CMP survey, reflectors will take on a hyperbolic shape as the distance to the reflection interface increases with antenna separation. Layer velocity can be determined from the two-way travel time (TWTT),  $t$ :

$$t = \sqrt{\left(\frac{x}{v}\right)^2 + \left(\frac{2h}{v}\right)^2} = \sqrt{\frac{x^2}{v^2} + t_0^2}$$

where  $x$  is the offset distance,  $h$  is the layer thickness,  $v$  is the layer velocity, and  $t_0$  is the travel time at normal incidence. The equation for the two-way travel time can be rearranged to achieve the layer velocity:

$$v = \sqrt{\left(\frac{x}{t}\right)^2 + \left(\frac{2h}{t}\right)^2}$$

Following the determination of the layer velocity, layer properties can be constrained by the relation of electromagnetic wave speed and dielectric permittivity:

$$v = \frac{c}{\sqrt{\epsilon_r}}$$

where  $\epsilon_r$  represents the relative dielectric permittivity (dielectric constant).

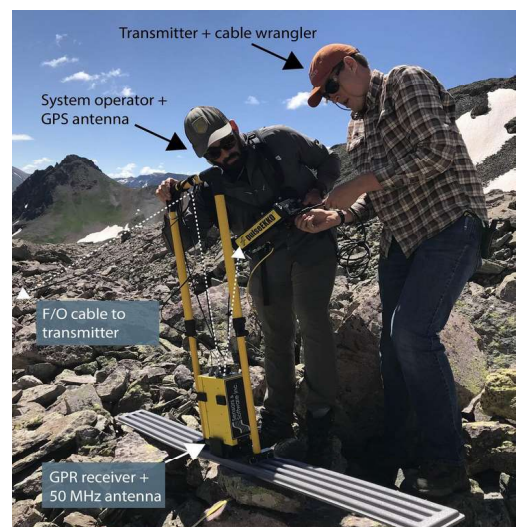


Figure 5. Typical system setup.  
Photo credit: Tyler Meng

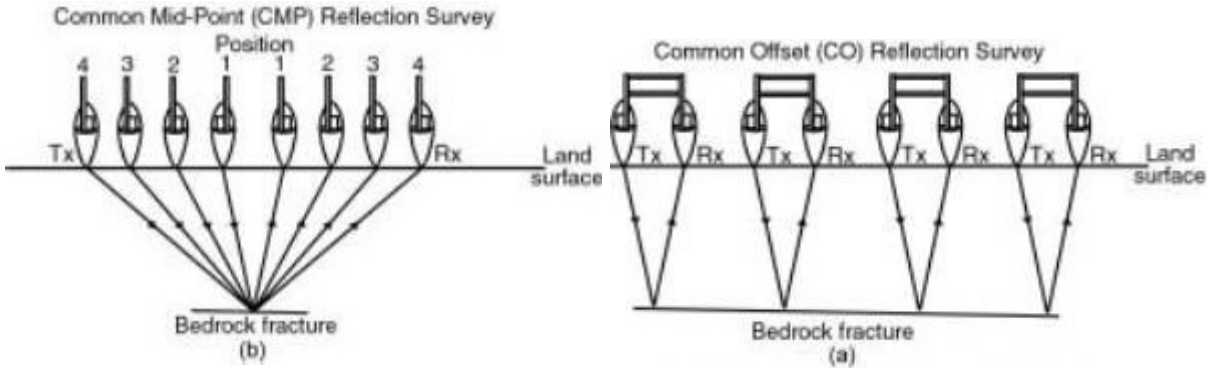


Figure 5. Diagram showing (a) the antenna geometry for a common-offset (CO) ground-penetrating radar reflection survey and (b) the antenna geometry for a common mid-point (CMP) survey used to derive the average subsurface radar propagation velocity. In both, Tx and Rx indicate the locations of the transmitting and receiving antennas, respectively. Source: United States Geological Survey (USGS).

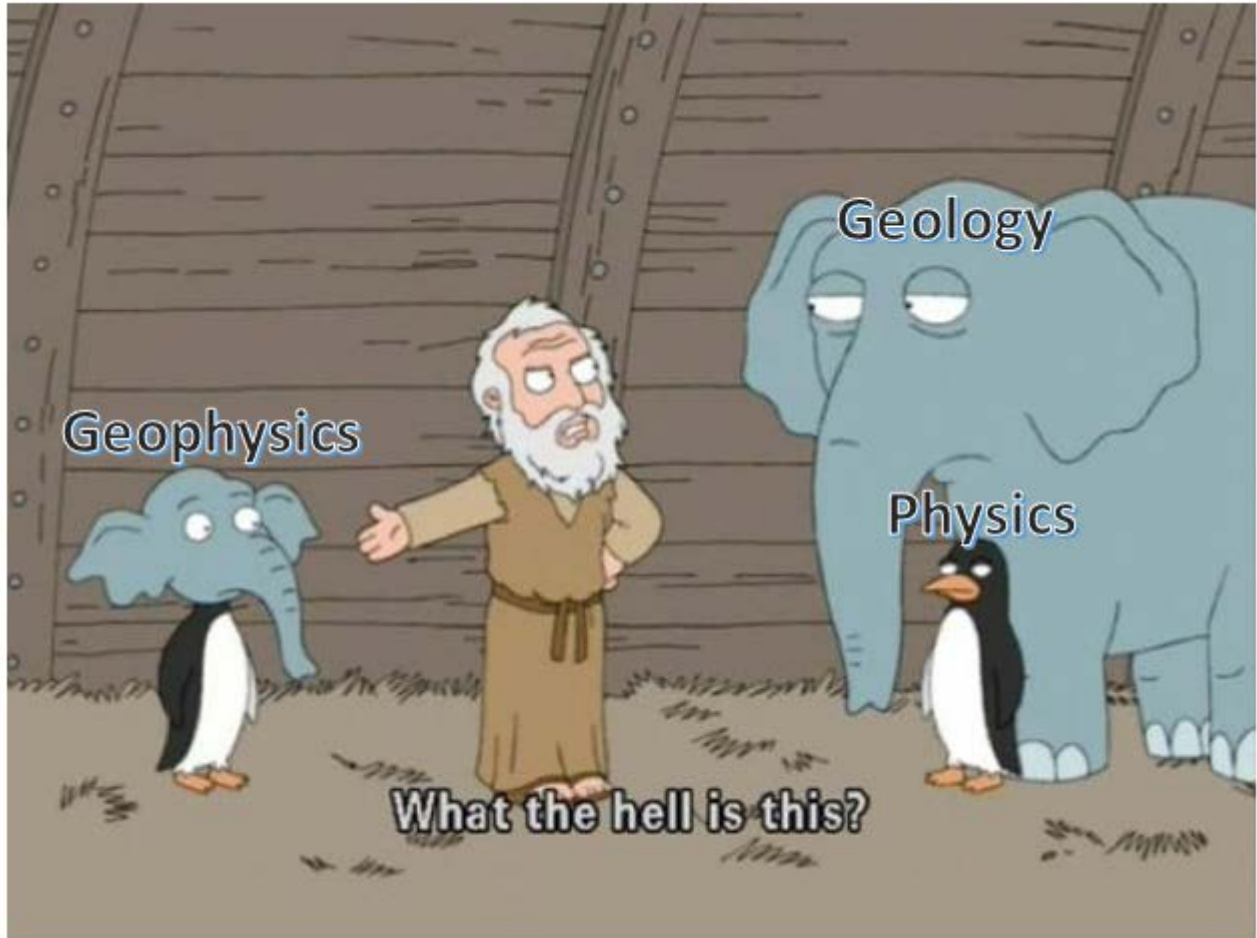
Post-acquisition, radar data will be viewed and interpreted using Sensors and Software's EKKO\_Project software. Here, horizons may be interpreted from any existing reflections resulting from geologic interfaces. Interpretation of CMP data also allows for the determination of electromagnetic wave speed within the layer atop a given reflection event. This will then allow for calculation of that layer's bulk dielectric permittivity, which helps to constrain the geologic medium.

Table 1: PulsEKKO system components

Component	Details
Control module/ Data logger	DVL500
Transmitter	PulsEKKO 100
Receiver	PulsEKKO Ultra
Transmitter antenna	50, 100, 200 MHz
Receiver antenna	10, 100, 200 MHz
GPS	Topcon SGR-1
Fiber optic cables	Data transfer

#### References

- Haruyama, J. et al. Possible lunar lava tube skylight observed by SELENE cameras. *Geophys. Res. Lett.* 36, L21206 (2009).
- Kaku, T., et al. (2017). Detection of intact lava tubes at Marius Hills on the Moon by SELENE (Kaguya) lunar radar sounder. *Geophysical Research Letters*, 44, 10,155– 10,161. <https://doi.org/10.1002/2017GL074998>.
- Keszthelyi, L. A preliminary thermal budget for lava tubes on the Earth and planets. *J. Geophys. Res.* 100, 20411–20420 (1995).
- Melville, Graeme P., Lava tubes and channels of the Earth, Venus, Moon and Mars, Master of Science (Hons.) thesis, Department of Physics, University of Wollongong, 1994. <https://ro.uow.edu.au/theses/2859>
- Miyamoto, H., et al. (2005). Mapping the structure and depth of lava tubes using ground penetrating radar, *Geophys. Res. Lett.*, 32, L21316, doi:10.1029/2005GL024159.
- Neal, A., (2004). Ground-penetrating radar and its use in sedimentology: principles, problems and progress. *Earth Science Reviews*, 36, pp. 261-330.



## Photogrammetry with Unmanned Aerial Vehicles

### Introduction

While airborne photography has existed as early as the 1850s, recent advances in and increased affordability of computer, camera and unmanned aerial vehicle (UAV) technologies have placed in the hands of the layperson an unprecedented ability to record digital imagery of the surroundings. In the hands of a geologist, this digital imagery can be collated to create a coherent picture that tells us something about our surroundings. This process of surveying and then creating a multi-dimensional model of the surroundings is known as *photogrammetry*.

The innovation of Structure-from-Motion (SfM) digital photogrammetry from multiple overlapping photographs has led to an explosion in high resolution 3D terrain reconstructions in the Earth sciences. In contrast to the more traditional LiDAR or photogrammetry using stereo pairs, which require accurate prior input of the camera locations and spatial orientations, SfM techniques make use of ground-control points (GCPs), giving it significant advantages in terms of ease of use, cost, flexibility and accuracy.

### What do you do in photogrammetry?

The first step in photogrammetry is to identify and match features (keypoints) across overlapping images, which capture a static scene from different locations. Provided that a sufficient number of feature matches are correctly identified, the scene can then be reconstructed, and the camera positions, orientations and lens properties are estimated in order to produce a sparse point cloud. The sparse point cloud and associated camera information form the basis for a much more detailed reconstruction using Multi-View Stereo (MVS) methods. The product is a dense **3-D point cloud**, which provides a realistic representation of the color and spatial detail of the scene. This 3-D point cloud can then be further processed to generate **orthoimages**, **triangulated textured meshes** and

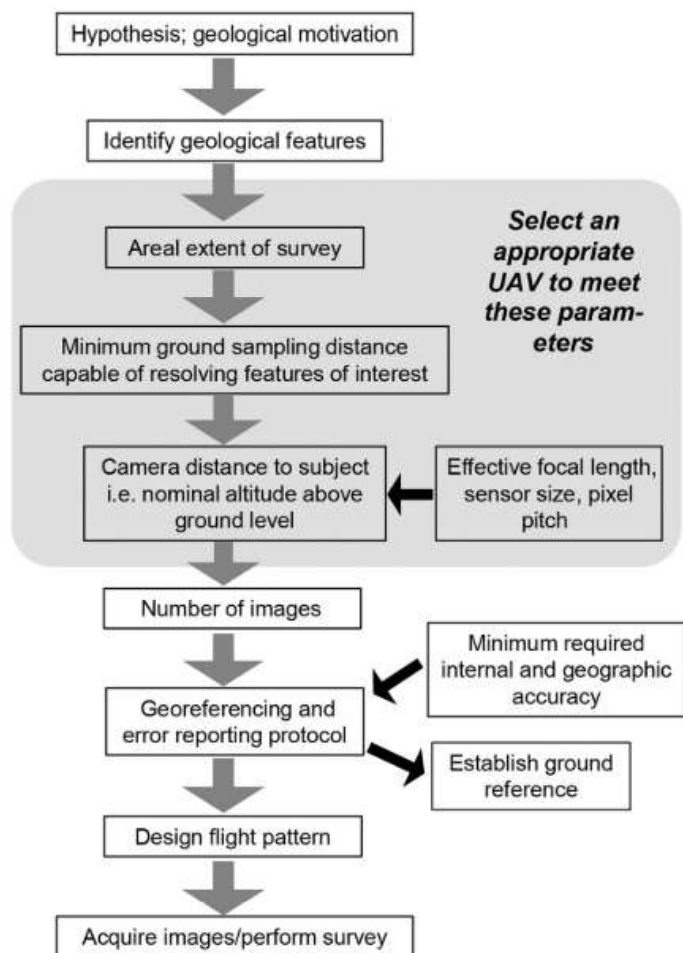


Fig. 1: Flowchart for planning a photogrammetric survey



### digital elevation models (DEMs).

Numerous SfM-MVS software, both open-source and commercial, are available for the geologist to produce these standard products from images obtained in a field survey.

### *How do you conduct a photogrammetric field survey?*

Fig. 1 shows the workflow for planning a photogrammetric survey. The steps of setting up the scientific problem and identifying relevant geologic features are common to every geological study, and we will not elaborate on them here.

The first photogrammetric step is then

to identify the areal extent of the survey and the minimum resolution to resolve features of interest. The size of the survey area and the minimum resolution required will determine many aspects of the survey. Firstly, they will determine the camera platforms use for the survey (Fig. 2). Multirotor aircraft have shorter ranges than fixed wing aircraft, and thus are not suitable for the largest survey areas. However, since fixed-wing aircraft have a minimum speed and a minimum altitude, they are not suitable for smaller survey areas or higher resolutions. Multirotor aircraft can instead hover, significantly reducing the effect of motion blur on the resolution.

The resolution is described by the ground sampling distance (GSD), or the distance a pixel represents in the real world. The GSD can be calculated using similar triangles with (Fig. 3)

$$GSD = \frac{z}{f} \frac{w}{N}$$

where  $z$  is the distance from the camera to the imaged target,  $f$  is the focal length of the camera,  $w$  is the physical width of the camera sensor, and  $N$  is the number of pixels that span that width. In general, the GSD should be 2–3 times finer than the dimensions of the feature to resolve it reliably and accurately. Also, note that the GSD represents a projected distance — the resolution will be worse if the target surface is

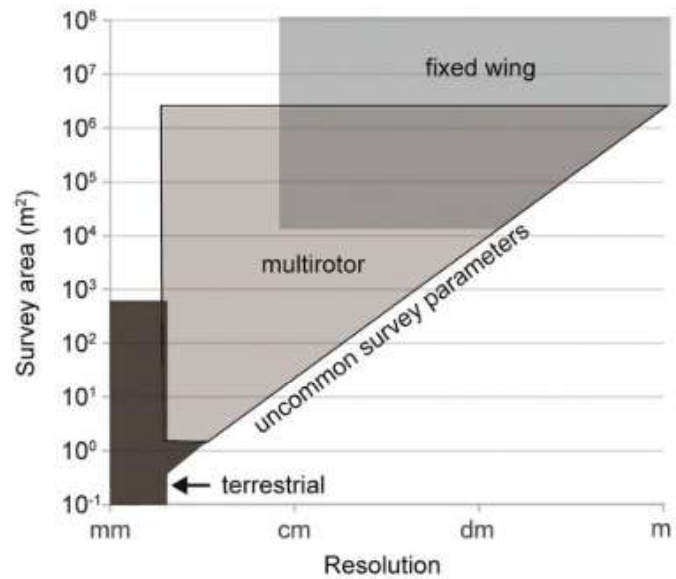


Fig. 2: Camera platforms for various sizes of survey area and resolution

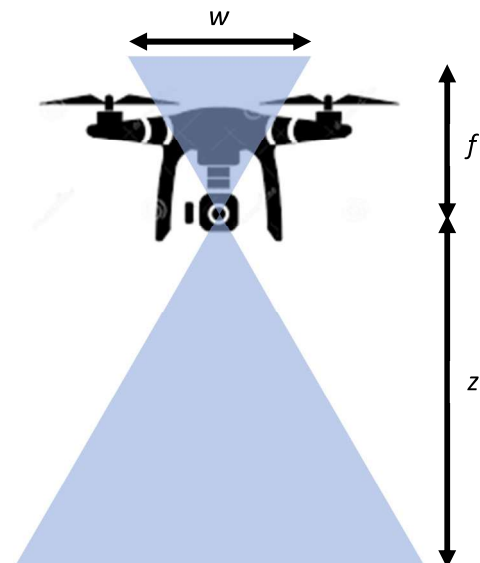


Fig. 3: Observation geometry for resolution calculation

tilted away from the camera. Thus for a typical scene, topography will result in varying GSD across the scene.

Most UAVs can be operated with mission planning software, which are often packaged together with the photogrammetric tools for data post-processing, allowing them to automatically follow pre-defined waypoints and systematically acquire aerial imagery with a set image overlap and GSD. Survey design should also take into account any local UAV flight regulations. A final consideration for survey design is the environmental conditions in which the UAV will operate. Diffuse lighting conditions are ideal (cloud cover, middle of the day) unless shadows in the scene have the advantage of illustrating features of interest. Fixed-wing UAVs are more significantly affected by the wind direction and wind speed than multi-rotor UAVs, resulting in their deviating from the planned course.

The ideal image acquisition plan depends on the type of terrain or object to be mapped. In the general case with relatively flat terrain and a moderate level of detail, the recommended overlap is at least 75% frontal overlap and at least 60% side overlap. Fig. 4 shows a typical regular grid pattern with a constant camera height.

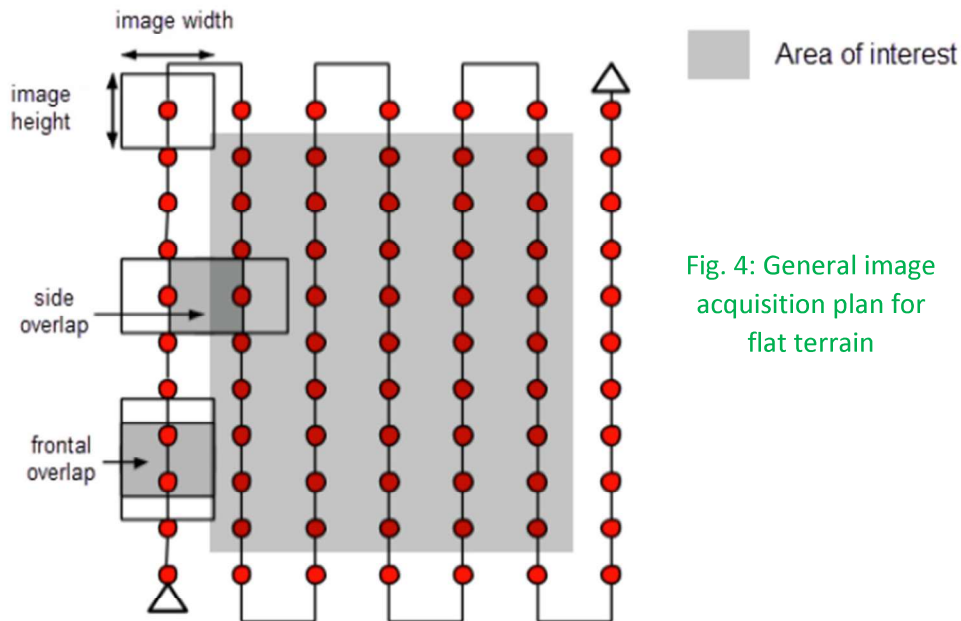


Fig. 4: General image acquisition plan for flat terrain

Scenes with complex detail and geometry (such as trees and dense vegetation with the thousands of branches and leaves) often have a very different appearance between overlapping images. In this case, the overlap can be increased to 85% frontal overlap and 70% side overlap. The flight height can also be increased so that there is less perspective distortion for easier keypoint registration. The same applies for scenes that are flat with homogeneous visual content such as agricultural fields, snow and sand. Reconstruction of 3-D buildings requires a special image acquisition plan, involving multiple flights around the building at different flight heights and camera angles. Water surfaces are impossible to map without surrounding land features.

GCPs provide an absolute spatial reference for the photogrammetric survey, allowing for the determination of scales, calibration of the camera location, orientation and lens properties, and the orientation of the scene relative to a geographic coordinate reference system such as Universal Transverse Mercator (UTM). These GCPs also allow for the calculation of spatial errors in the scene model. Although many UAVs come equipped with GPS systems, the onboard GPS of small UAVs tend to be insufficiently precise, particularly when surveying at high resolutions. Although georeferencing of the model can be done with a minimum of 3 GCPs, each registered in at least 2 images, accurate georeferencing would generally require 5–10 GCPs evenly distributed over the scene. Additional GCPs can be added for calculation of spatial errors. The physical size of the GCPs should be 5–10 times larger than the GSD for their location to be accurately resolved in the model.

### **References**

Dering, Gregory M., et al. "Review of drones, photogrammetry and emerging sensor technology for the study of dykes: Best practises and future potential." *Journal of Volcanology and Geothermal Research* (2019).

Pix4D SA. *Pix4Dmapper 4.1 user manual*. 2019.

DJI. *Mavic 2 Pro/Zoom user manual*. 2019.

Rees, William Gareth. *Physical principles of remote sensing*. Cambridge University Press, 2013.

## Activity

For our activity, we will be using the Pix4D software package to come up with the image acquisition plan and the data processing. Images will be taken with the DJI Mavic 2 Pro drone.

### 1: Image Acquisition

We will be using the Pix4Dcapture Android app on a mobile phone to plan the flight route and acquire the images.

Connect the phone to the Mavic 2 Pro controller via USB. Start the Ctrl+DJI app and ensure that a connection to the drone is established. Select OPEN PIX4DCAPTURE and login to your account.

Select Plan new mission > DOUBLE GRID MISSION to begin a new mission plan.

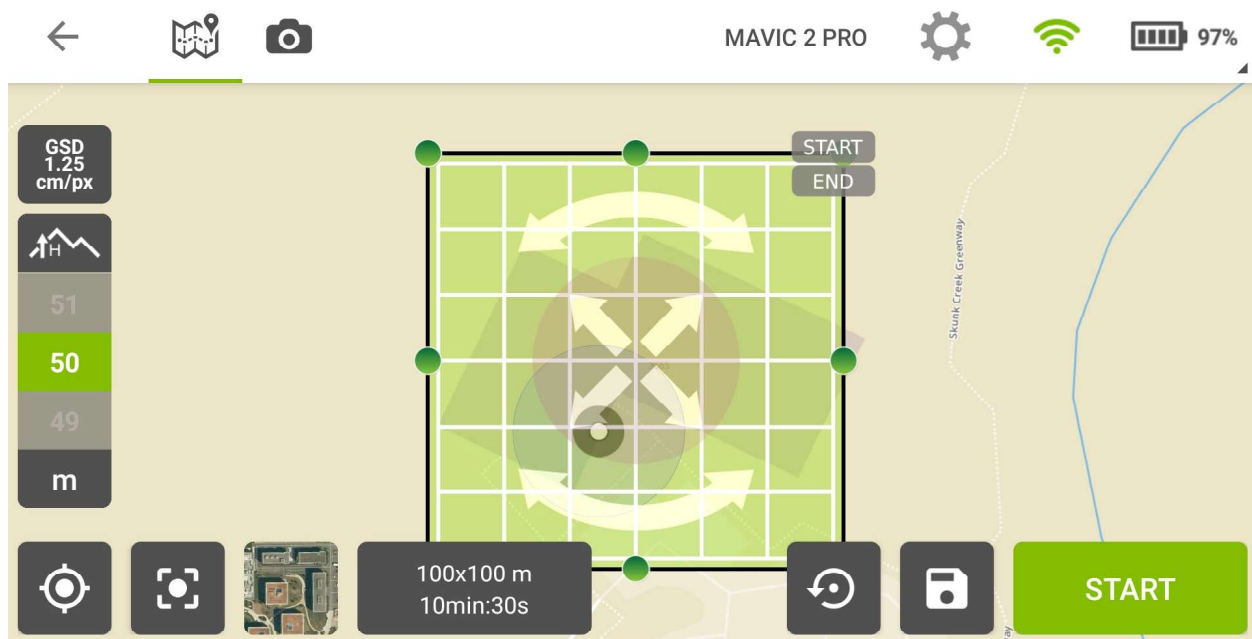


Fig. 5: Flight Plan screen on the Pix4Dcapture app

The Flight Plan screen will open. Pix4Dcapture by default overlays a 100 m by 100 m rectangular flight plan over a map representing the current location based on the phone's location.

Ensure that MAVIC 2 PRO is shown next to the Flight Settings icon at the top. Right of the Flight Settings icon is the Drone Connection icon. If green the drone is properly connected to Pix4Dcapture. If grey, there is no connection to the drone. Right of the Drone Connection icon is the Drone Battery icon indicating the drone's battery levels.

Drone speed, camera angle and image overlap can be adjusted under Flight Settings. For our study, we will be using the default fastest speed, 70° camera angle and 80% overlap.

The flight plan is shown at the center of the screen, with the target area in light green. The area can be resized by dragging the green circles on the perimeter of the area, rotated by dragging the curved arrows, and moved by dragging the cross at the center. The dark gray box at the bottom shows the size of the target area and the total flight time required (maximum flight time for the Mavic Pro 2 is 31 minutes). The starting and ending location of the drone are marked by the `START` and `END` labels respectively.

The flight altitude can be controlled by the scrollbar on the left (the flight ceiling mandated by the FAA is 120 m). The resulting GSD is shown above the scrollbar.

Select `START` to begin the survey. A `Takeoff Checklist` will appear. Ensure that all list items are green. `PRESS AND HOLD (3S) TO TAKEOFF` to begin. The `Pix4Dcapture` app will provide live telemetry from the drone in the `Mapview`. The path flown by the drone is represented by a green line, and a camera icon represents where images are acquired. The mission can be stopped any time with `ABORT`, leaving the drone hovering.

On the completion of the survey, land and turn off the drone. Download the acquired images onto a computer.

## 2: Data Post-Processing

### 2.1: Initialization

After we have acquired the images and downloaded them onto the computer, we will be using the `Pix4Dmapper` software for post-processing.

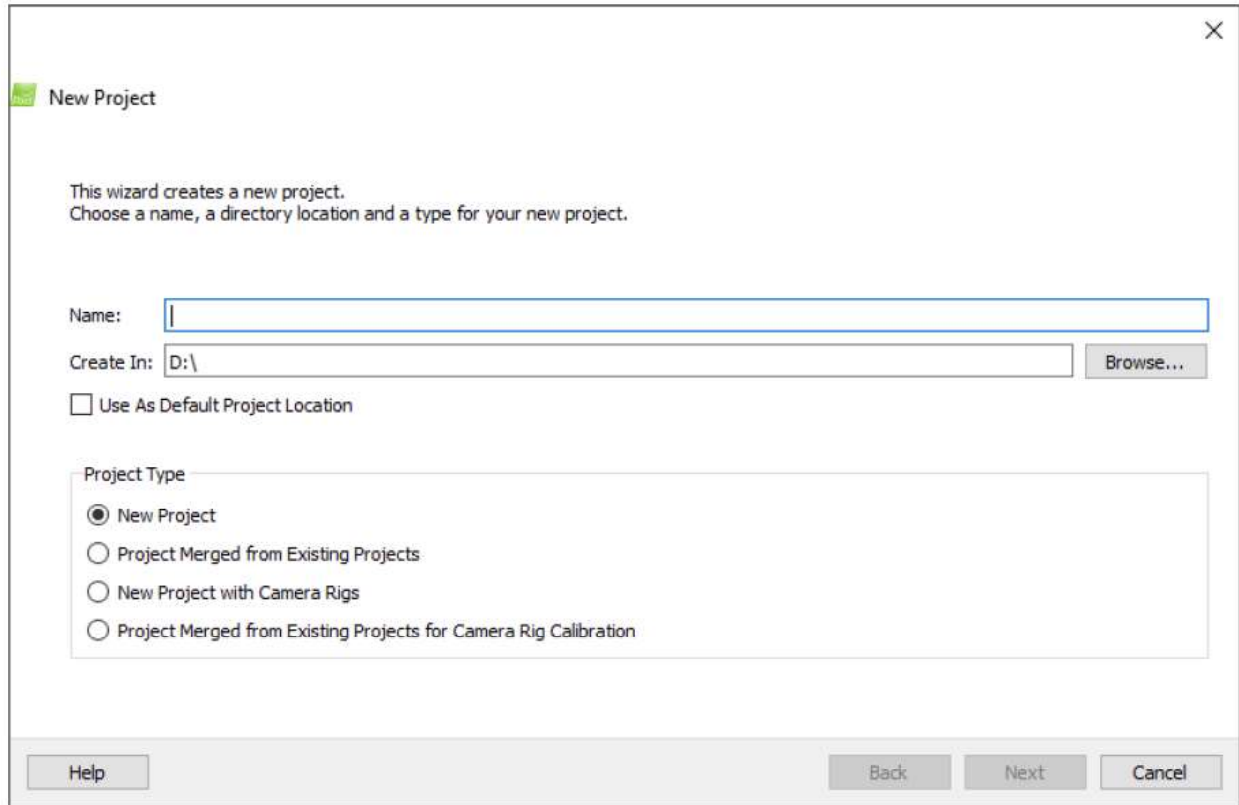


Fig. 6: The New Project wizard window

After starting Pix4Dmapper, we will create a new project with `Project > New Project...` on the menu bar. Type in a name for the project. Keep the default option `New Project` selected for `Project Type`, and click `Next`.

The `Select Images` window will open. Click `Add Images...`, and in the pop-up select the images to be imported, and click `Open`. Individual images can be removed with `Remove Selected`, or the entire list can be removed by clicking `Clear List`. Click `Next`.

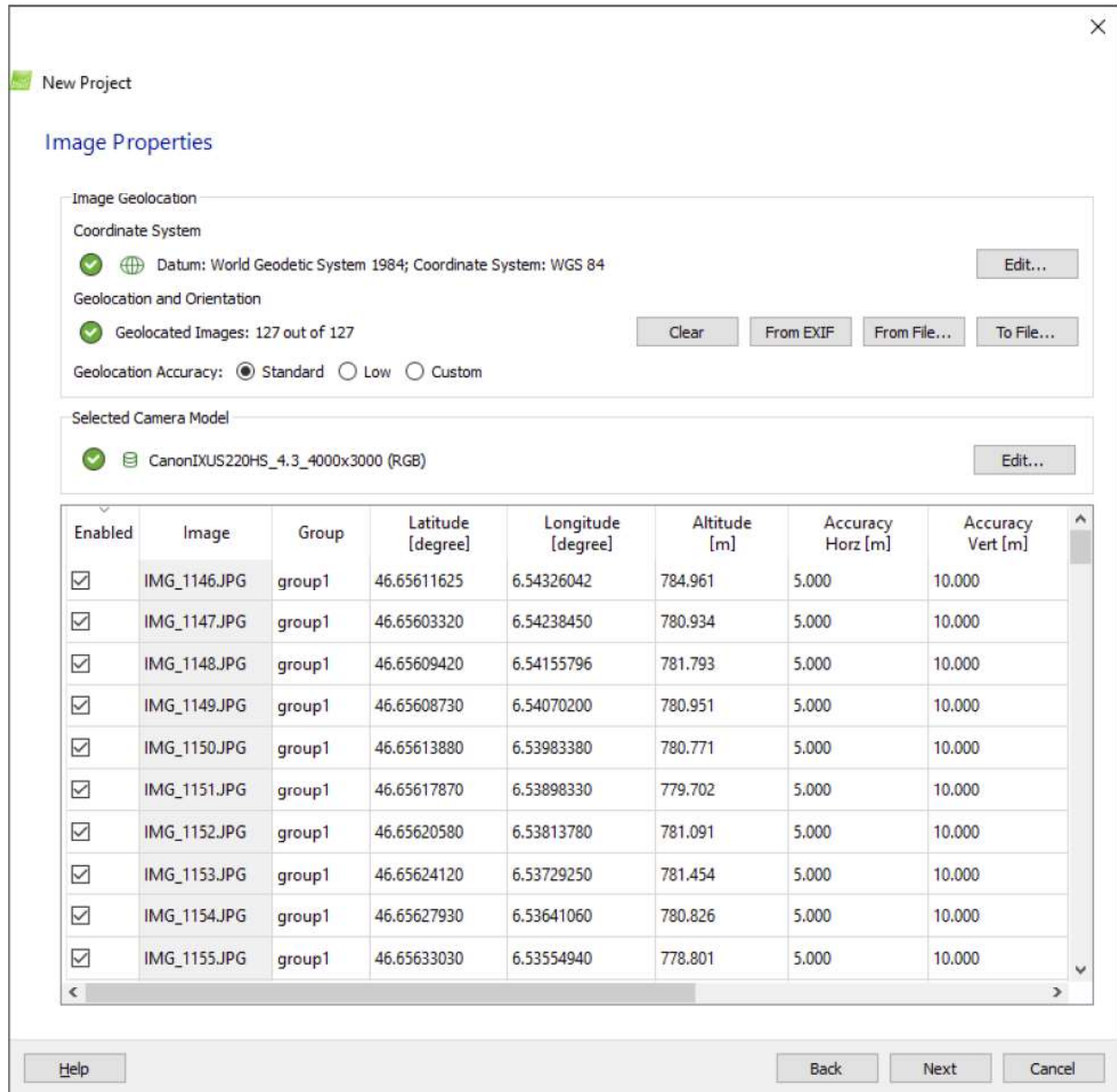


Fig. 7: The Image Properties window

The New Project wizard will then display the Image Properties window. Choose World Geodetic System 84 for the datum and the default coordinate system of Geographic Lat. Long. in Decimal Degrees. D.ddddddd. Geolocation and Orientation automatically displays the information stored in the EXIF of the images.

Choose DJI Mavic 2 Pro for the camera model. Most cameras save their name in the metadata of the image in EXIF format. A green check is displayed if the camera model is valid. If the camera model is not valid, a red cross is displayed and the camera model needs to be defined manually.

The Images table displays the selected images, as well as the group, position, position accuracy and orientation of each image and if the image is enabled for processing.

Click Next.

The Select Output Coordinate System window will then appear. Click Next.

The Processing Options Template window will appear. Choose 3D Maps – Rapid/Low Res and click Finish to close the wizard and start the project. Once the project is created, the Map View is displayed.



Fig. 8: The main window with the Map View tab active



## 2.2: GCP Registration

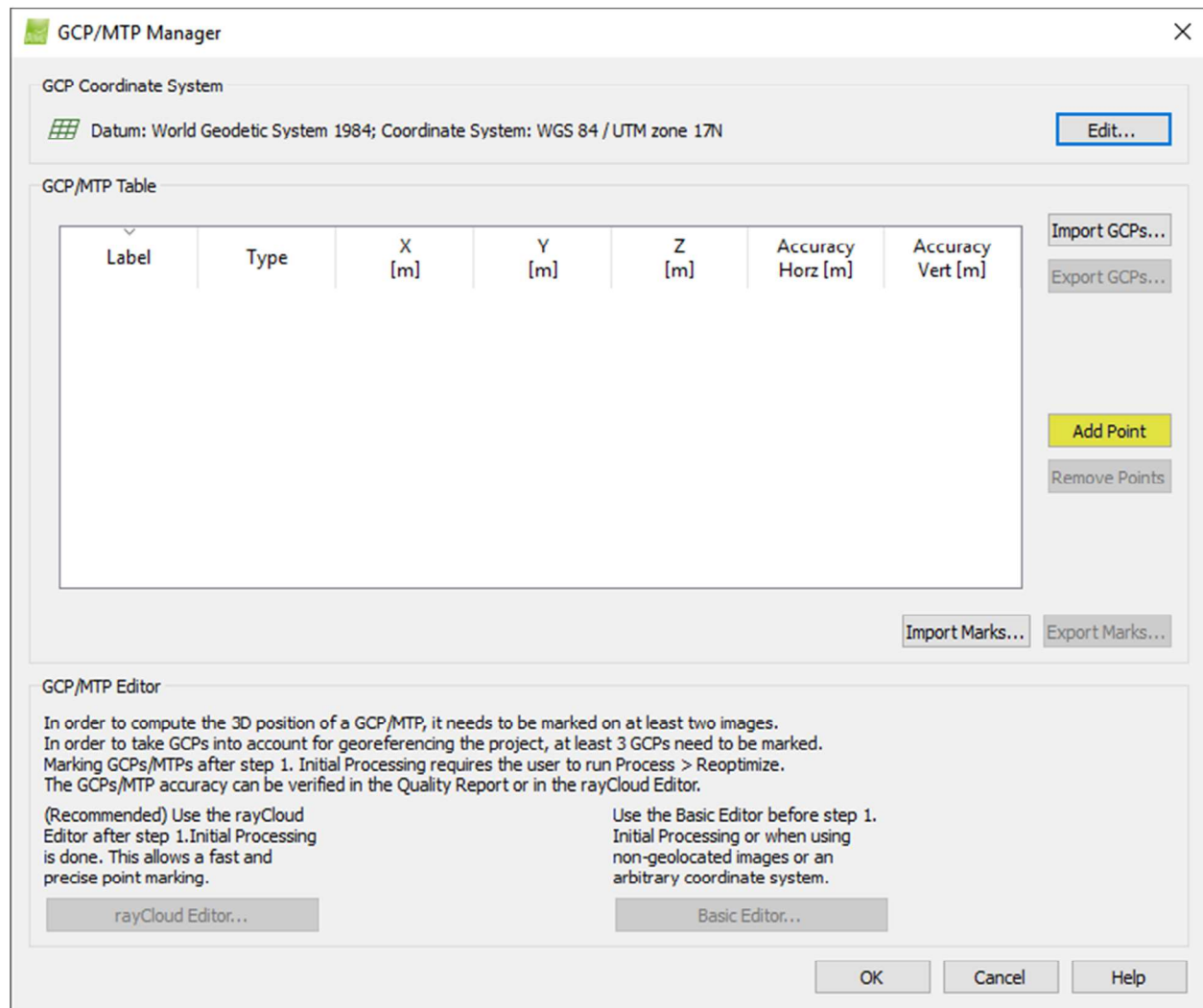


Fig. 9: The GCP/MTP main window

Open the GCP/MTP Manager with `Project > GCP/MTP Manager...` on the menu bar. Enter the GCP coordinates by clicking `Add Point`. Choose 3D GCP in the drop-down list under `Type` and enter the coordinates and accuracy of the GCP. Repeat for the rest of the GCPs.

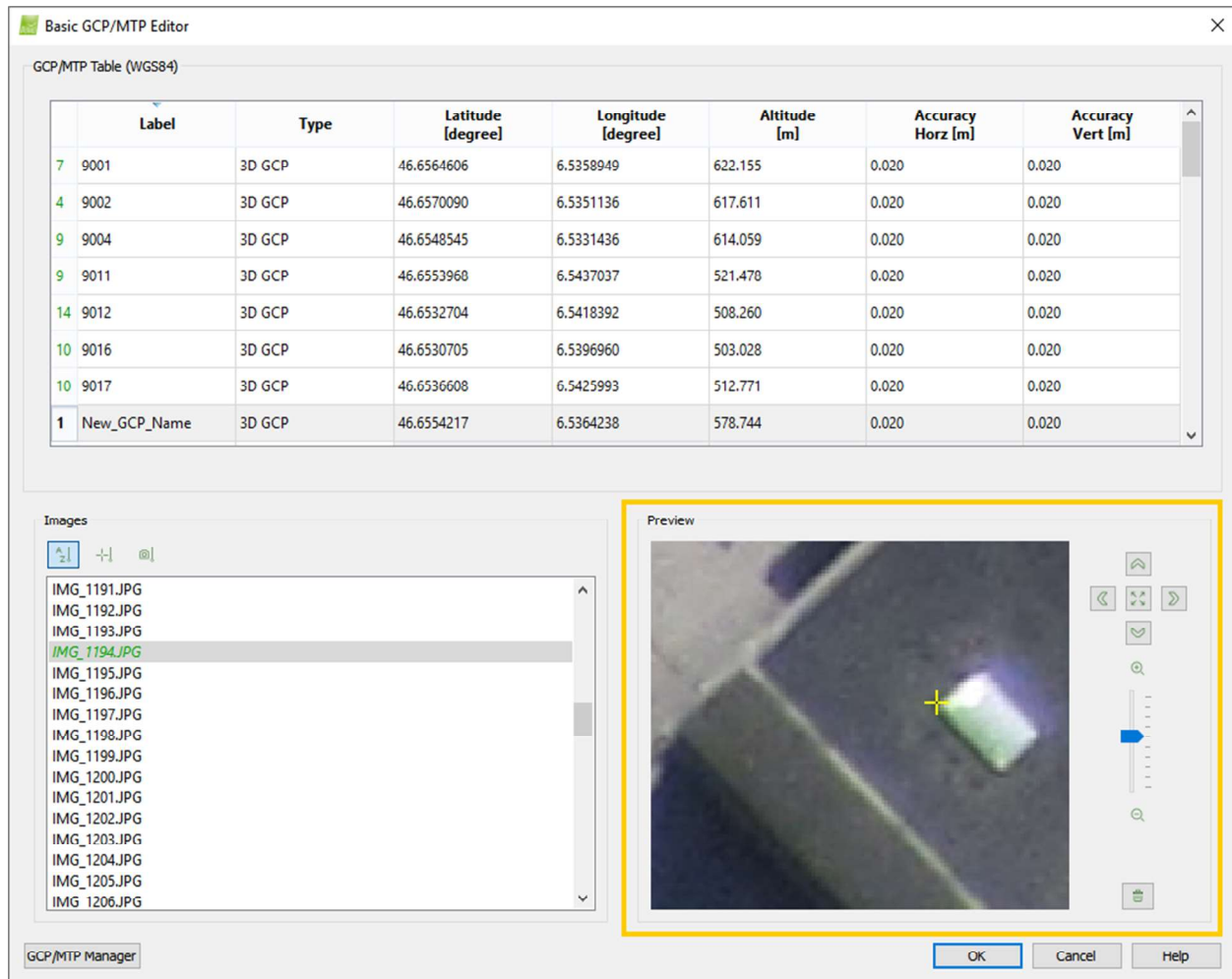


Fig. 10: Registration of the GCP location in the Basic GCP/MTP Editor window

Click Basic Editor... to open the Basic GCP/MTP Editor. In order to mark the location of the GCP on the image, select the GCP to be marked in the GCP/MTP table, the image in the Images table, and left-click the location of the GCP in the Preview image at the bottom right. Click Remove to remove a mark. Repeat over all the images for which the GCP appears, and the other GCPs. Click OK to close the Basic GCP/MTP Editor and OK again to close the GCP/MTP Manager.

### 2.3: Initial Processing

Initial processing provides an initial check to ensure the dataset is free from problems for subsequent processing. To start initial processing, click View > Processing on the menu bar. The Processing bar opens on the bottom of the main window. Ensure that 1. Initial Processing is selected and that 2. Point cloud and Mesh and 3. DSM, Orthomosaic and Index are unselected. Click Start.

Once initial processing is complete, the `Quality Report` is automatically displayed. Verify the following information in the `Quality Report`:

#### Quality Check

- All the checks are green.
- Dataset: All or almost all the images are calibrated in one block.
- Camera Optimization: The relative difference between initial and optimized internal camera parameters is below 5%.
- The GCP error is below 3xGSD.

#### Quality Check i









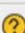

 <b>Images</b>	median of 35858 keypoints per image	
 <b>Dataset</b>	127 out of 127 images calibrated (100%), all images enabled	
 <b>Camera Optimization</b>	0.44% relative difference between initial and optimized internal camera parameters	
 <b>Matching</b>	median of 13945.5 matches per calibrated image	
 <b>Georeferencing</b>	yes, 7 GCPs (7 3D), mean error = 0.046 m	

Fig. 11: Quality Check report following initial processing

#### Computed Image/GCPs/Manual Tie Points Positions

- The difference between input and computed GCPs is small.

#### Absolute Camera Position and Orientation Uncertainties

- The absolute camera position uncertainties are similar to the accuracy of the GCPs.

#### Geolocation Details

- All GCPs are taken into account (not displayed with red color on the Geolocation and Ground Control Points table).
- All marked GCPs have been verified.

#### 2.4: Point Cloud and Mesh Processing

On the menu bar, click `View > Processing`. Select 2. `Point Cloud and Mesh`, and unselect 1. `Initial Processing` and 3. `DSM, Orthomosaic and Index` in the `Processing bar`. Click `Start`.

#### 2.5: DSM, Orthomosaic and Index Processing

On the menu bar, click View > Processing. Select 3. DSM, Orthomosaic and Index, and unselect 1. Initial Processing, and 2. Point Cloud and Mesh in the Processing bar. Click Start.

A new directory named 3\_dsm\_ortho will be created in the project directory with the following subdirectories to contain the products:

- 1\_dsm: Stores the Raster DSM and the Grid DSM
- 2\_mosaic: Stores the orthomosaic
- dtm: Stores the DTM

# Common Rock Forming Minerals

Dark-Colored minerals			
Hardness	Cleavage	Physical Properties	Name
Hardness >5	Excellent or good	Dark gray, Blue-gray or black. May be iridescent. Cleavage in 2 planes at nearly right angles. Striations. Hardness-6	<b>Plagioclase Feldspar</b>
		Brown, gray, green or red. Cleavage in 2 planes at nearly right angles. Exsolution Lamellae. Hardness-6	<b>Potassium Feldspar</b>
		Opaque black. 2 cleavage planes at 60° and 120°. Hardness- 5.5	<b>Hornblende (Amphibole)</b>
	Poor or absent	Opaque red, gray, hexagonal prisms with striated flat ends. Hardness- 9	<b>Corrundum</b>
		Gray, brown or purple. Greasy luster. Massive or hexagonal prisms and pyramids. Transparent or translucent. Hardness- 7	<b>Quartz Black or brown-Smoky , Purple-Amethyst</b>
		Opaque red or brown. Waxy luster. Hardness- 7. Conchoidal Fracture	<b>Jasper</b>
Opaque black. Waxy luster. Hardness- 7		<b>Flint</b>	
		Transparent- translucent dark red to black. Hardness- 7	<b>Garnet</b>
Hardness < 5	Excellent or good	Colorless, purple, green, yellow, blue. Octahedral cleavage. Hardness- 4	<b>Flourite</b>
		Green. Splits along 1 excellent cleavage plane. Hardness- 2-3	<b>Chlorite</b>
		Black to dark brown. Splits along 1 excellent cleavage plane. Hardness- 2.5-3	<b>Biotite mica</b>
	Poor or absent	Opaque green, yellow or gray. Silky or greasy luster. Hardness- 2-5	<b>Serpentine</b>
		Opaque white, gray or green. Can be scratched with fingernail. Soapy feel. Hardness- 1	<b>Talc</b>
		Opaque earthy red to light brown. Hardness- 1.5-6	<b>Hematite</b>

Light-colored minerals			
Hardness	Cleavage	Physical Properties	Name
Hardness >5	Excellent or good	White or gray. Cleavage in 2 planes at nearly right angles. Striations. Hardness-6	<b>Plagioclase Feldspar</b>
		Orange, brown, white, gray, green or pink. Cleavage in 2 planes at nearly right angles. Exsolution Lamellae. Hardness-6	<b>Potassium Feldspar</b>
		Pale brown, white or gray. Long slender prisms. Cleavage in 1 plane. Hardness- 6-7	<b>Sillimanite</b>
	Poor or absent	Opaque red, gray, white hexagonal prisms with striated flat ends. Hardness- 9	<b>Corrundum</b>
		Colorless, white, gray or other colors. Greasy luster. Massive or hexagonal prisms and pyramids. Transparent or translucent. Hardness- 7	<b>Quartz White-Milky, Yellow-Citrine, Pink- Rose</b>
		Opaque gray or white. Waxy luster. Hardness- 7. Conchoidal Fracture	<b>Chert</b>
Colorless, white, yellow, light brown. Translucent opaque. Laminated or massive. Cryptocrystalline. Hardness- 7		<b>Chalcedony</b>	
		Pale olive green. Conchoidal fracture. Transparent or translucent. Hardness- 7	<b>Olivine</b>
Hardness < 5	Excellent or good	Colorless, white, yellow, blue, green. Excellent cleavage in 3 planes. Breaks into rhombohedrons. Effervesces in HCl. Hardness- 3	<b>Calcite</b>
		Colorless, white, yellow, blue, green. Excellent cleavage in 3 planes. Breaks into rhombohedrons. Effervesces in HCl only if powdered. Hardness- 3.5-4	<b>Dolomite</b>
		White with tints of brown. Short tabular crystals or roses. Very heavy. Hardness- 3-3.5	<b>Barite</b>
		Colorless, white or gray. Massive or tabular crystals, blades or needles. Can be scratched by fingernail. Hardness- 2	<b>Gypsum</b>
		Colorless, white. Cubic crystals. Salty taste. Hardness- 2.5	<b>Halite</b>
		Colorless, purple, green, yellow, blue. Octahedral cleavage. Hardness- 4	<b>Flourite</b>
	Poor or absent	Colorless, yellow, brown. Splits along 1 excellent cleavage plane. Hardness- 2-2.5	<b>Muscovite mica</b>
		Yellow crystals or earthy masses. Hardness 1.5-2.5	<b>Sulfur</b>
		Opaque green, yellow or gray. Silky or greasy luster. Hardness- 2-5	<b>Serpentine</b>
		Opaque white, gray or green. Can be scratched with fingernail. Soapy feel. Hardness- 1	<b>Talc</b>
		Opaque earthy white to light brown. Hardness- 1-2	<b>Kaolinite</b>

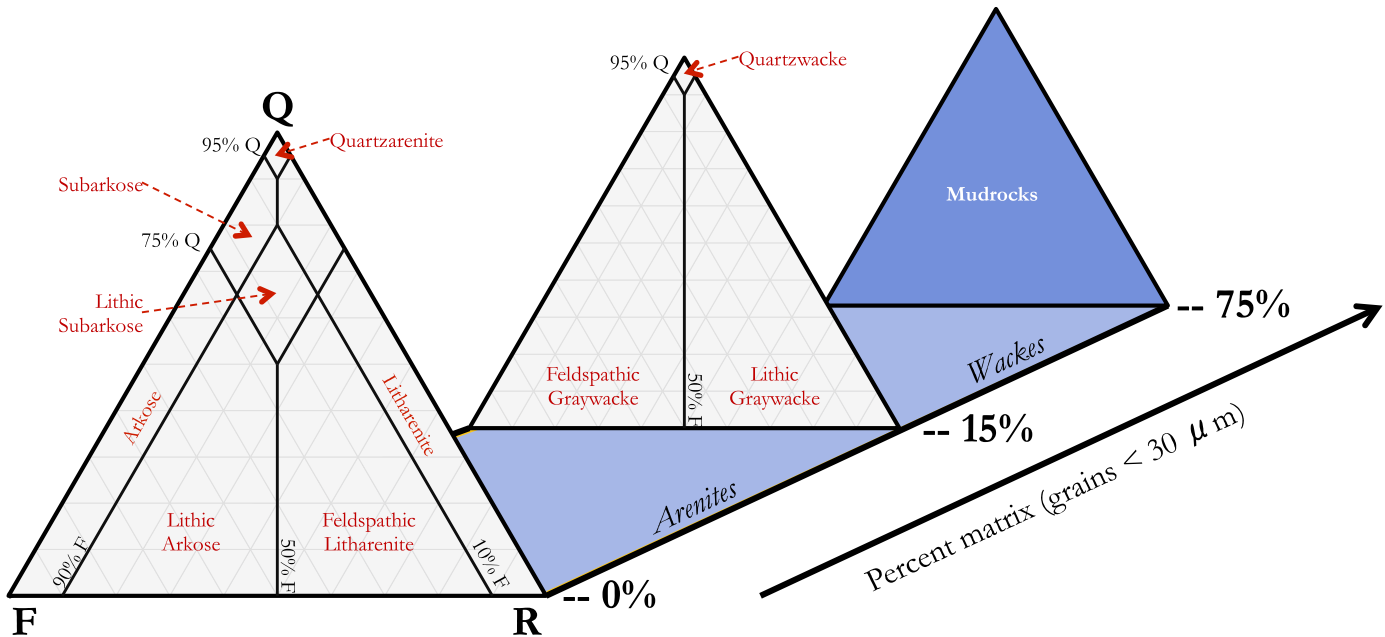
Metallic			
	Streak	Physical Properties	Name
Hardness > 5		Brass yellow	<b>Pyrite</b>
	Dark Gray	Dark gray-black, attracted to magnet	<b>Magnetite</b>
	Brown	Silvery black to black tarnishes gray	<b>Chromite</b>
Hardness < 5	Red-Red/Brown	Silvery gray, black, or brick red	<b>Hematite</b>
		Brass yellow, tarnishes dark brown or purple	<b>Chalcopyrite</b>
		Iridescent blue, purple or copper red, tarnishes dark purple	<b>Bornite</b>
	Dark Gray	Silvery gray, tarnishes dull gray Cleavage good to excellent	<b>Galena</b>
		Dark gray to black, can be scratched with fingernail	<b>Graphite</b>

# Sedimentary Rocks

## McBride, 1963 & Dott, 1964 Classification Scheme for Clastic Sedimentary Rocks

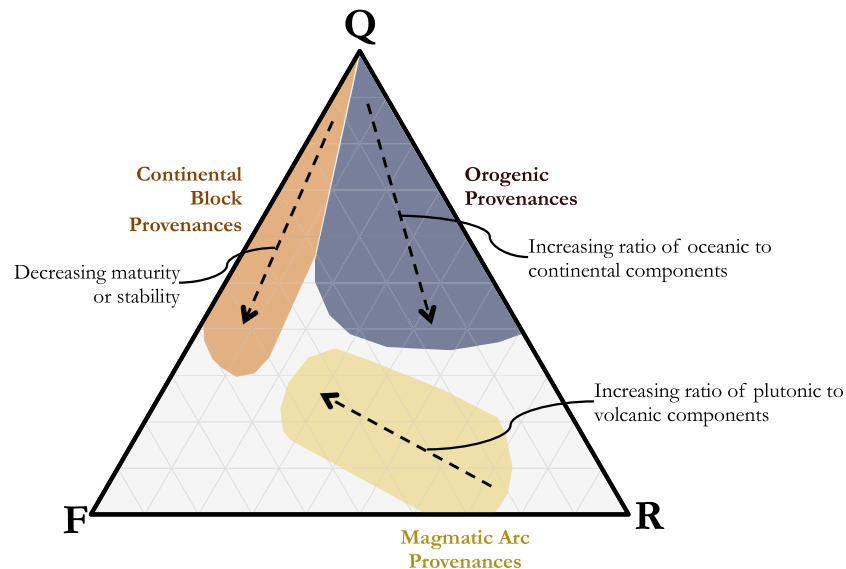


Scheme based on the normalized percentages of the visible grains: quartz and chert (Q), feldspar (F), and lithic rock fragments (R) – as well as the percent composed of matrix (mud & silt)



## Tectonic Setting for Clastic Sedimentary Rocks

Scheme based on the normalized percentages of the visible grains: quartz and chert (Q), feldspar (F), and lithic rock fragments (R) – as well as the percent composed of matrix (mud & silt). Regions based upon field data.



# Sedimentary Rocks

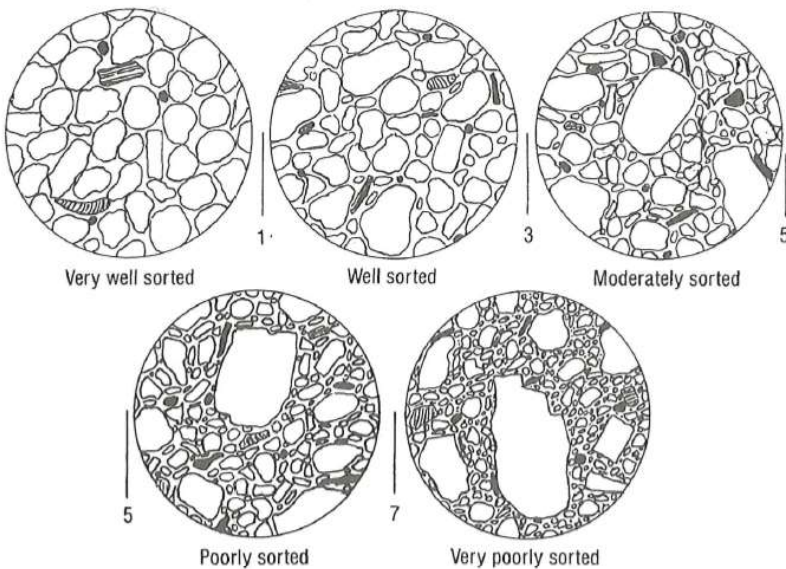
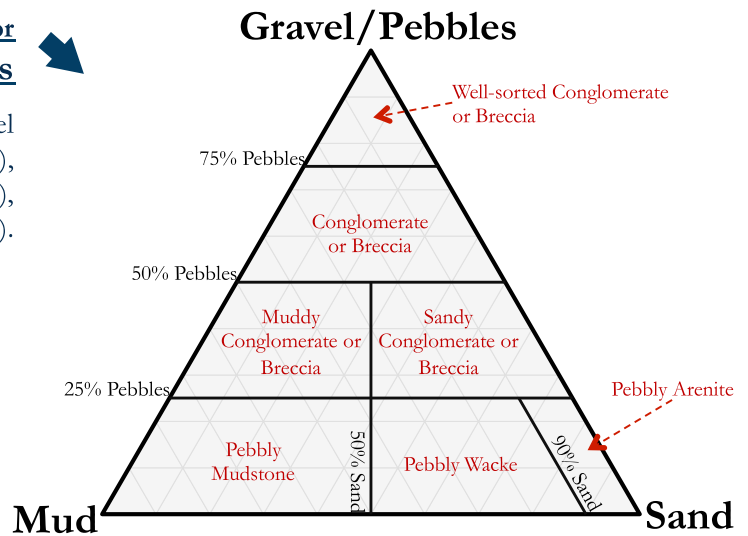
	Mudrocks (containing > 50% mud)			Rocks with <50% mud
	Silt dominant (> 2/3 of rock)	Clay and Silt	Clay dominant (> 2/3 of rock)	Sand-sized or larger grains dominant
<b>Non-laminated</b>	Siltstone	Mudstone	Claystone	Conglomerates, Breccias, Sandstones, etc.
<b>Laminated</b>	Laminated Siltstone	Mudshale	Clayshale	

← **Classification Scheme for Mudrocks**

Scheme based on clay/silt content, and whether the rock is laminated (layered) or not.

## Classification Scheme for Sub-Conglomerates and Sub-Breccias

Scheme based on percent of a rock composed of: gravel or pebbles (size >2 mm), sand (2 mm > size > 1/16 mm), and mud (size < 1/16 mm).



## ← Estimating Sorting

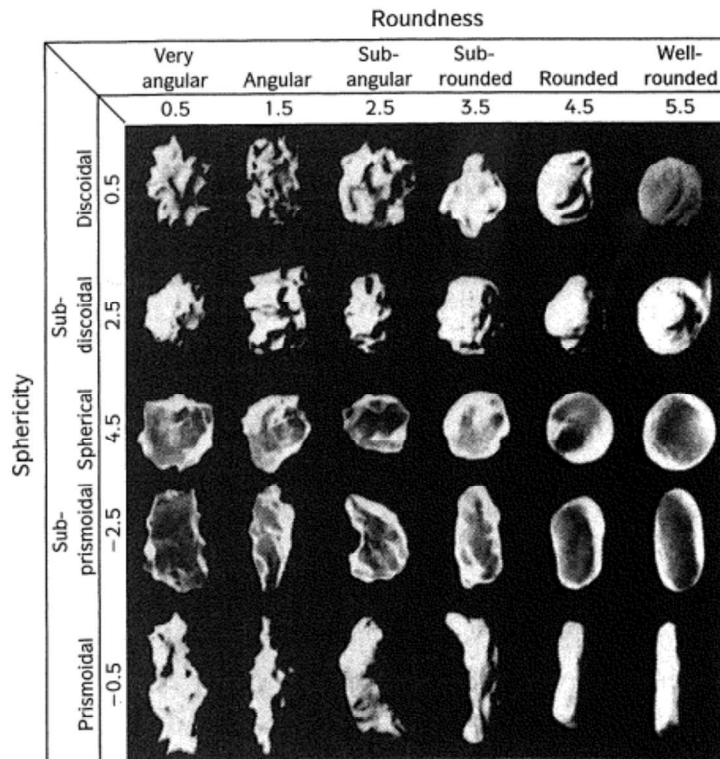
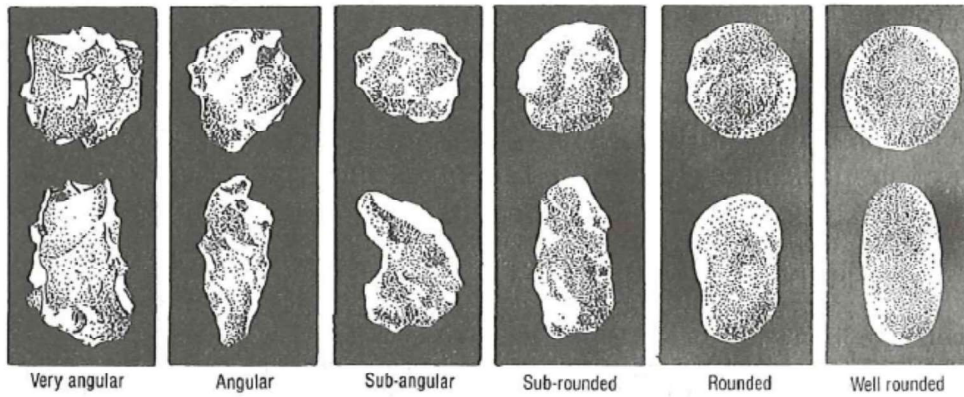
Example hand-lens view of detritus.  
From Compton, 1985

# Sedimentary Rocks

## Degrees of Rounding



Example hand-lens view of detritus of varying degrees of roundedness. The top row are equidimensional (spherical) grains, while the lower row are elongated grains. From Compton, 1985 and Davis & Reynolds, 1996, respectively.



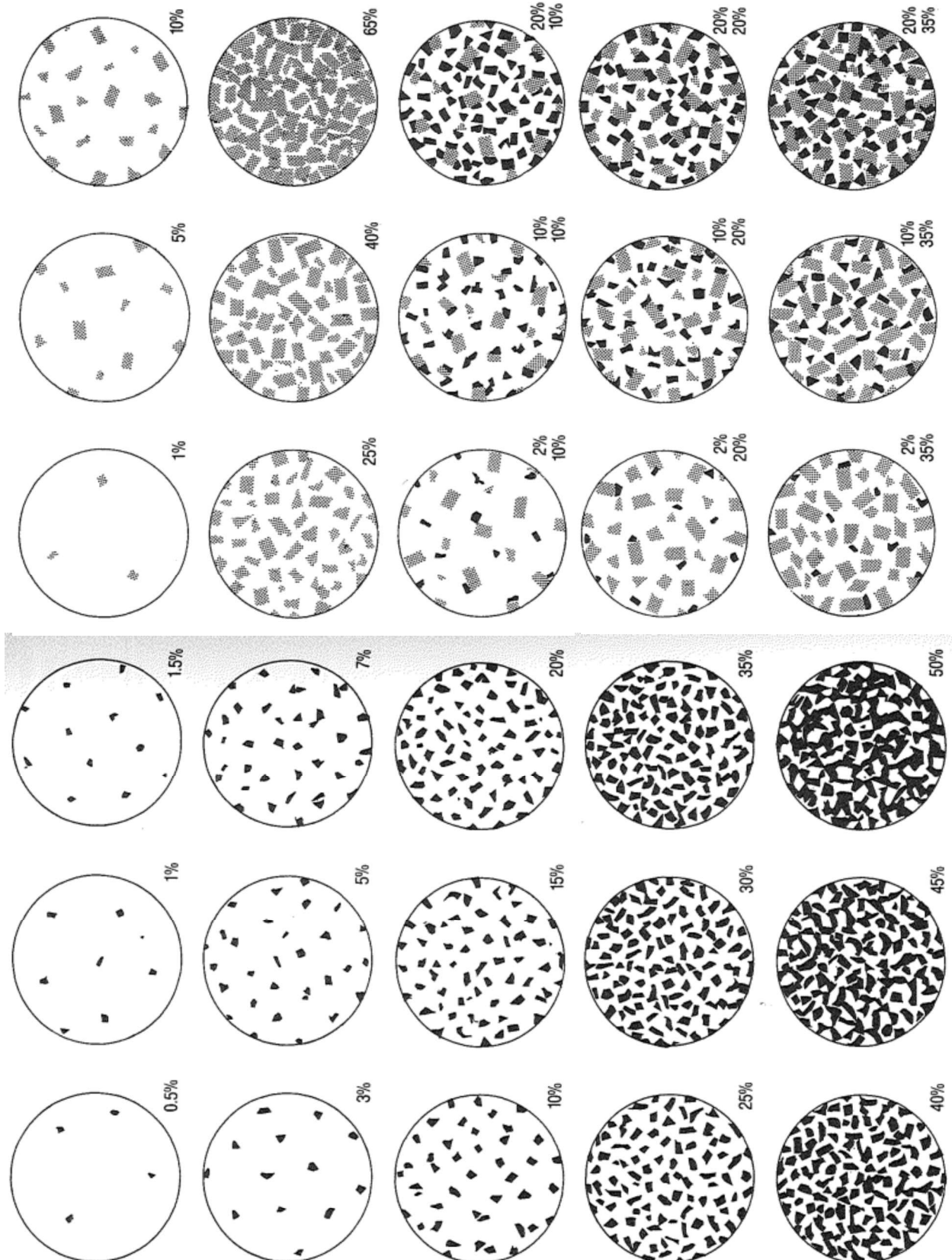


# Sedimentary Rocks

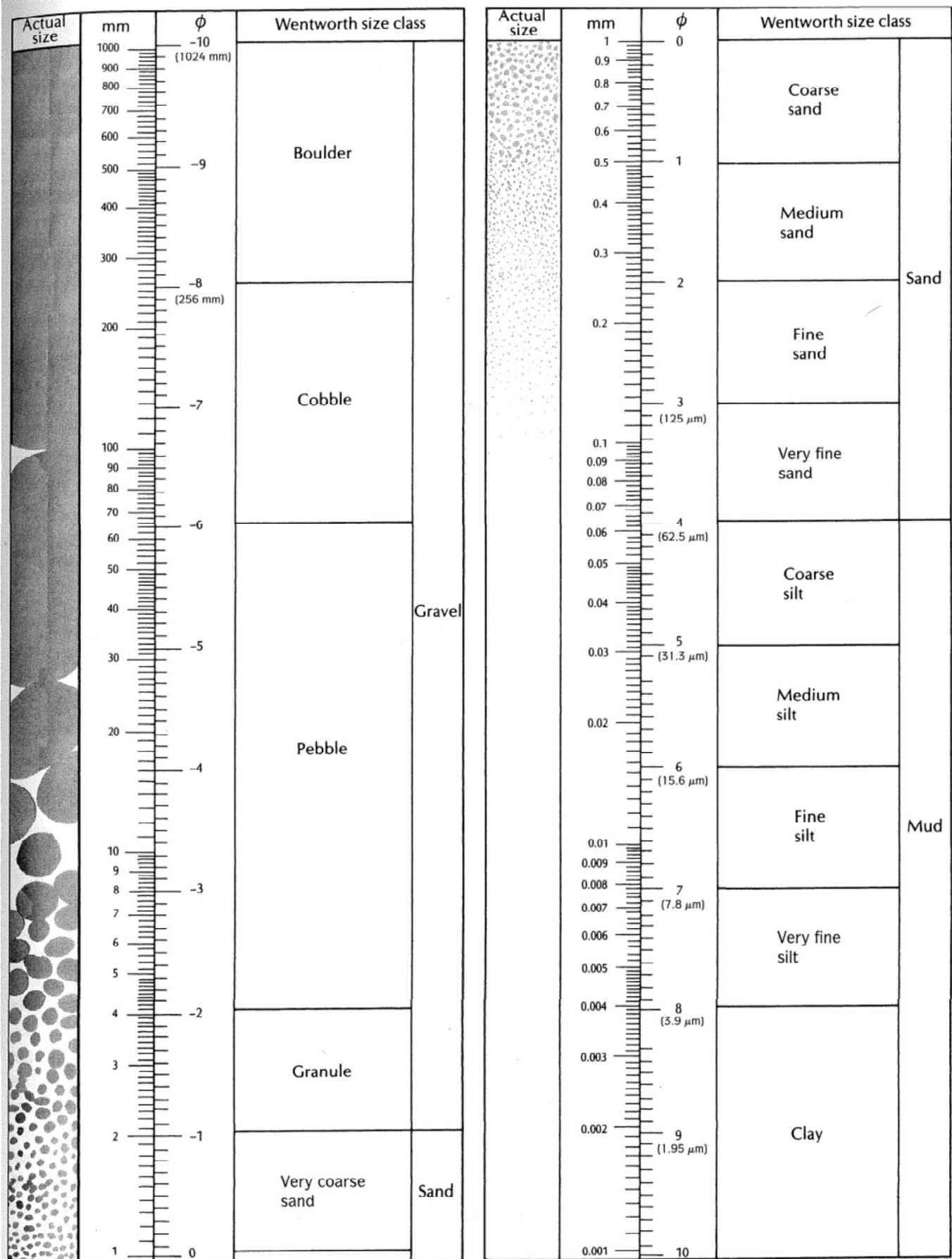
## Percentage Diagrams for Estimating Composition by Volume



Example hand-lens view of rocks with varying composition. To find weight percents, simply multiply each volume percent by the specific gravity of that mineral, and re-normalize. Compton, 1985




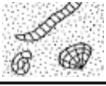
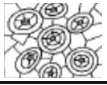
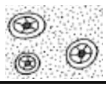
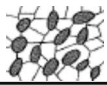

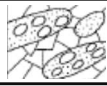

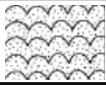
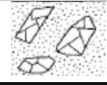
# Sedimentary Rocks



# Sedimentary Rocks: Carbonates

## Folk Classification Scheme for Carbonate Rocks

Folk's classification scheme is based upon the composition (and type of allochems) within a limestone. Figures from Prothero and Schwab, 2004

Principle Allochems in Limestone	Limestone Type			
	Cemented by Sparite		Cemented by Micritic Matrix	
Skeletal Grains (Bioclasts)	Biosparite		Biomicrite	
Ooids	Oosparite		Oomicrite	
Peloids	Pelsparite		Pelmicrite	
Intraclasts	Intrasparite		Intramicroite	
Limestone formed in place	Biolithite		Terrestrial Limestone	

## Dunham Classification Scheme for Carbonate Rocks

Dunham's classification scheme is based upon depositional textures within a limestone.

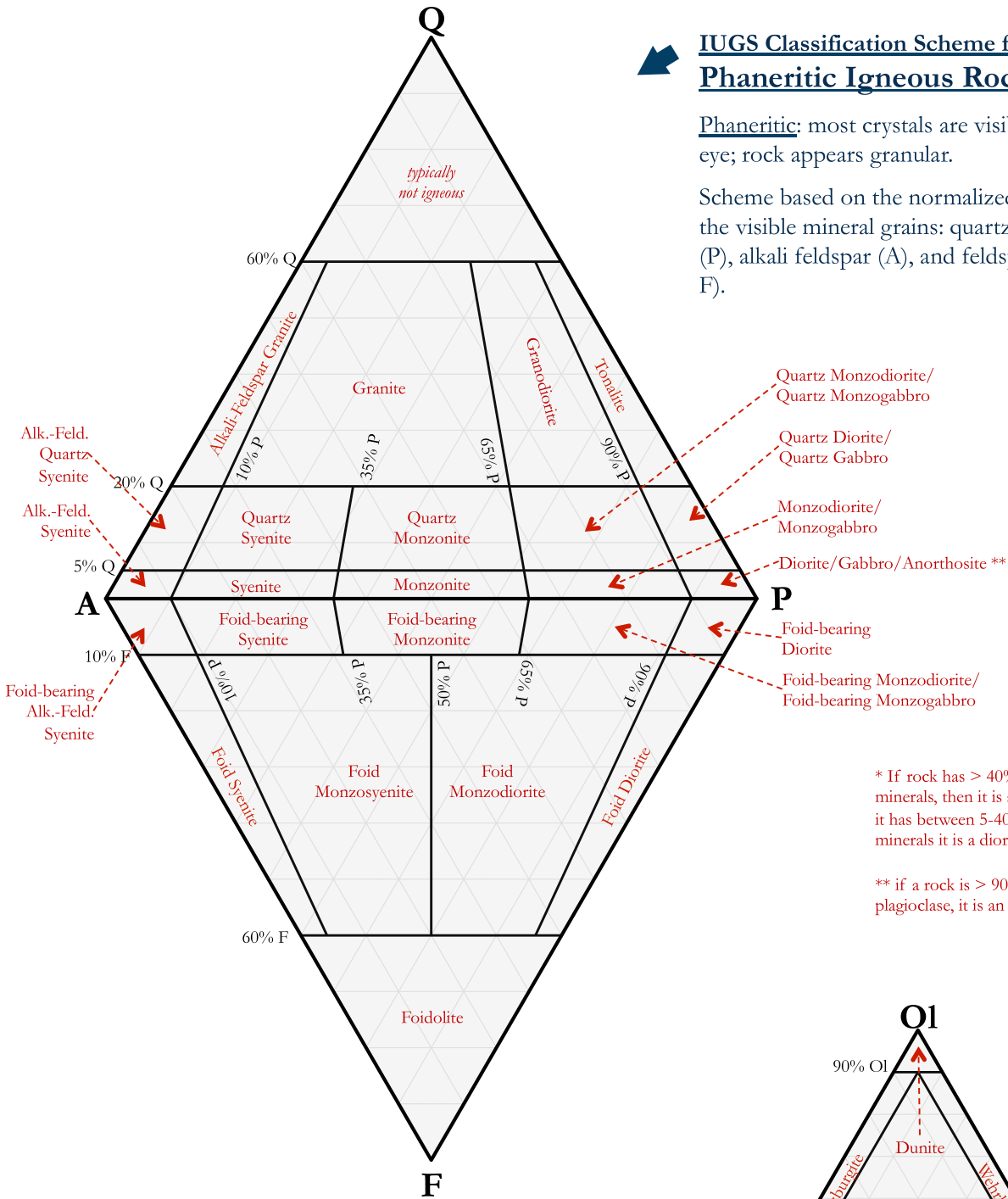
Allochthonous Limestone (original components not organically bound during deposition)				Autochthonous Limestone (original components organically bound during deposition; reef rocks)				
Of the allochems, less than 10% are larger than 2 mm		Of the allochems, greater than 10% are larger than 2 mm						
Contains carbonate mud		No mud		Matrix supported	Grain supported	Organisms acted as baffles	Organisms are encrusting and binding	Organisms building a rigid framework
Grain supported		Grain supported						
Less than 10% grains	More than 10% grains							
Mudstone	Wackestone	Packstone	Grainstone	Floatstone	Rudstone	Bafflestone	Bindstone	Framestone

# Igneous Rocks

## IUGS Classification Scheme for Phaneritic Igneous Rocks

Phaneritic: most crystals are visible to the naked eye; rock appears granular.

Scheme based on the normalized percentages of the visible mineral grains: quartz (Q), plagioclase (P), alkali feldspar (A), and feldspathoids (foids, F).



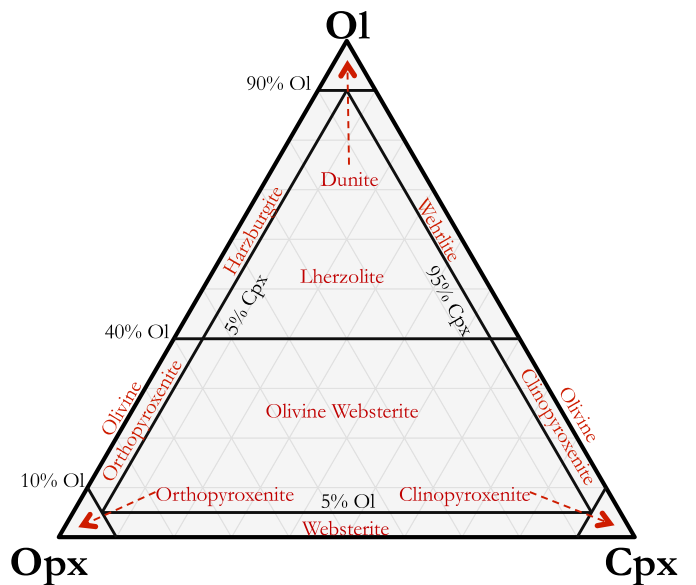
\* If rock has > 40% mafic minerals, then it is a gabbro. If it has between 5-40% mafic minerals it is a diorite.

\*\* if a rock is > 90% plagioclase, it is an anorthosite

## IUGS Classification Scheme for Phaneritic Ultramafic Igneous Rocks (1)

Ultramafic: more than 90% of the total minerals are mafic.

Scheme based on the normalized percentages of the visible minerals: olivine (Ol), orthopyroxene (Opx), and clinopyroxene (Cpx).

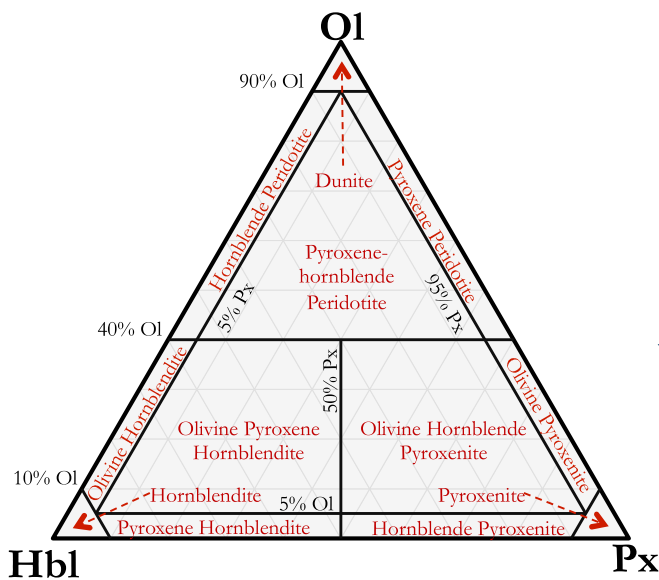
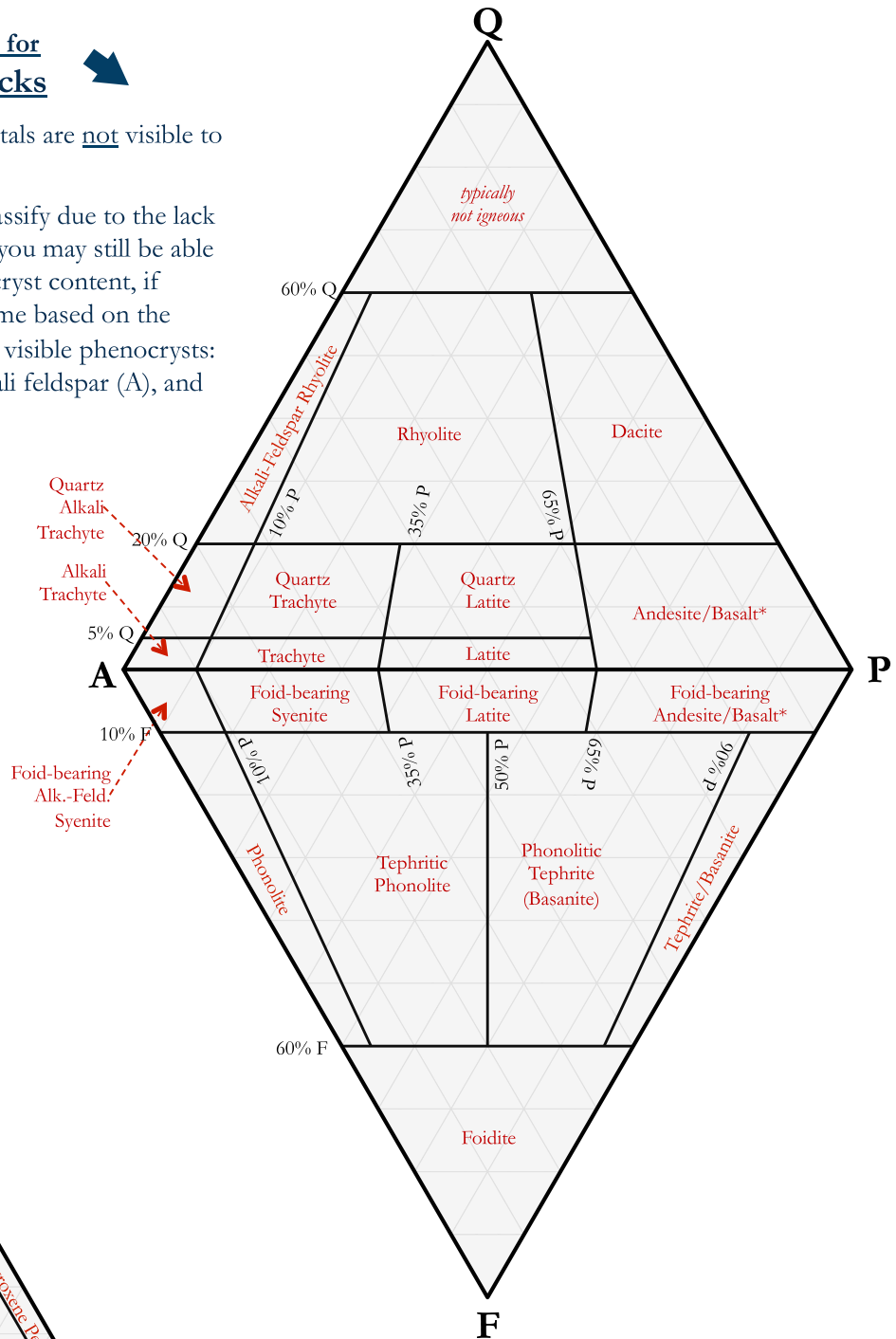


# Igneous Rocks

## IUGS Classification Scheme for Aphanitic Igneous Rocks

Aphanitic: the majority of crystals are not visible to the naked eye.

Aphanitic rocks are hard to classify due to the lack of visible minerals. However, you may still be able to identify them based on phenocryst content, if phenocrysts are present. Scheme based on the normalized percentages of the visible phenocrysts: quartz (Q), plagioclase (P), alkali feldspar (A), and feldspathoids (foids, F).



## IUGS Classification Scheme for Phaneritic Ultramafic Igneous Rocks (2)

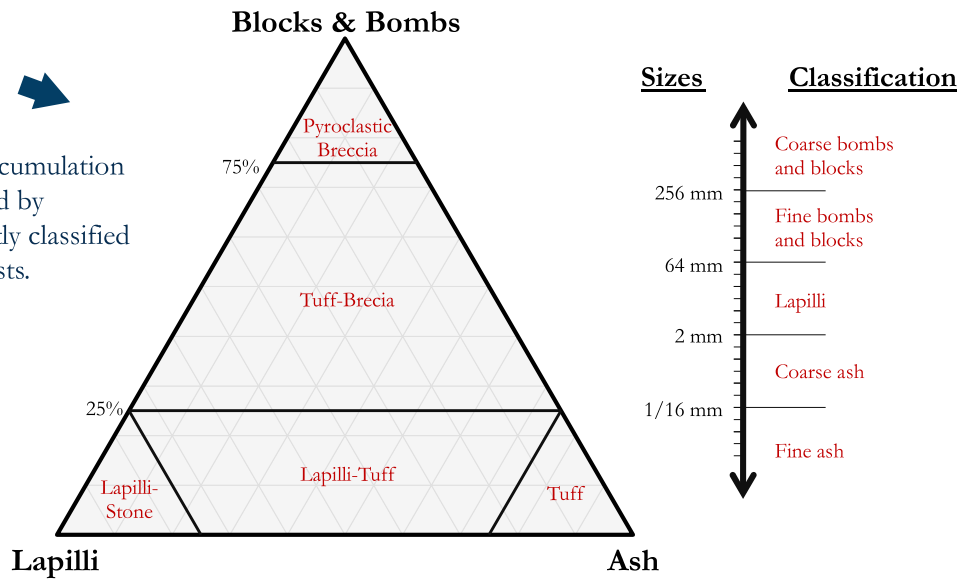
Ultramafic: more than 90% of the total minerals are mafic.

Scheme based on the normalized percentages of the visible minerals: olivine (Ol), hornblende (Hbl), and pyroxene (Px).

# Igneous Rocks

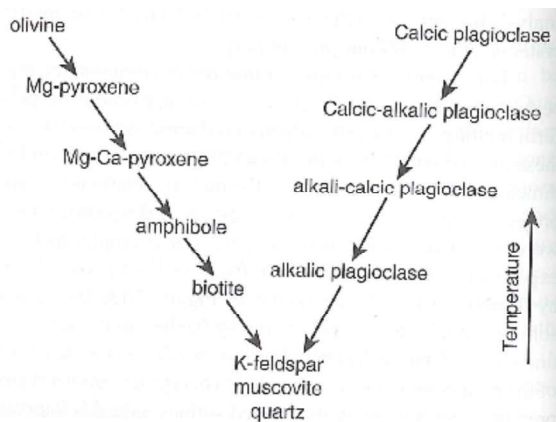
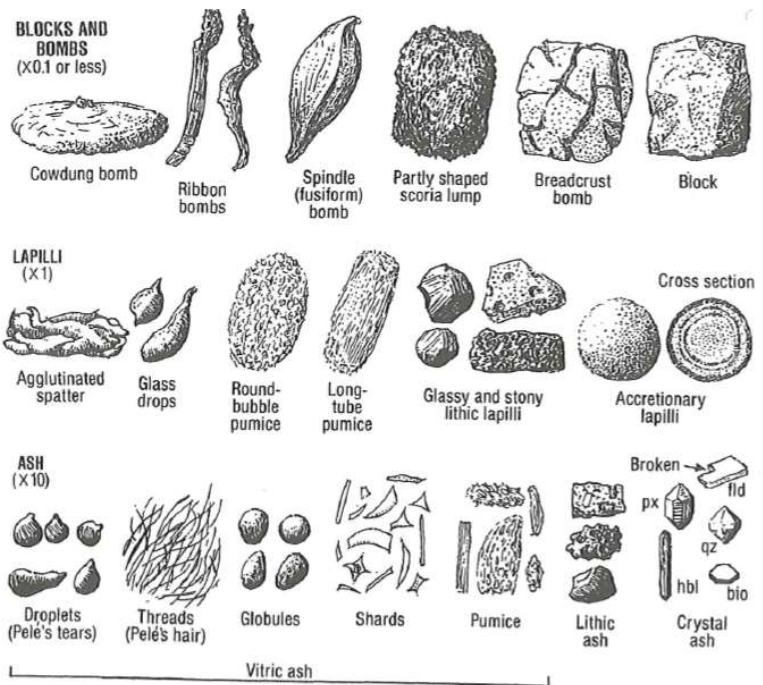
## Classification Scheme for Pyroclastic Igneous Rocks

Pyroclastic rocks are formed via the accumulation of fragments of volcanic rock scattered by volcanic explosions. They are frequently classified based upon the size distribution of clasts.



## Types of Tephra (Pyroclasts)

In each row, the viscosity of the lava increases to the right. From Compton, 1985.



## Bowen's Reaction Series

From Winter, 2010.

# Metamorphic Rocks



## Classification Scheme for Metamorphic Rocks

Based upon texture and mineralogical composition.

Structure & Texture	Characteristic Properties	Characteristic Mineralogy	Rock Name	
Foliate (layered)	Increasing grain size, and degree of metamorphism ↓	Dull luster; very flat fracture surface; grains are too small to readily see; more dense than shale	No visible minerals	Slate
		Silky sheen; Crenulated (wavy) fracture structure; A few grains visible, but most are not	Development of mica and/or hornblende possible	Phyllite
		Sub-parallel orientations of individual mineral grains; wavy-sheet like fracture; often contains porphyroblasts; thinly foliated	Abundant feldspar; Quartz and mica are common; hornblende possible	Schist
		Sub-parallel, alternating bands or layers of light and dark material; coarsely foliated; blocky fracture	Abundant feldspars; Quartz, mica, and hornblende are common	Gneiss
Foliate (layered)	Interlocking crystals; effervesces in dilute HCl; softer than glass	Calcite	Marble	
	Nearly equigranular grains; fracture across grains (not around them); sub-vitreous appearance; smooth feel compared to sandstone	Quartz	Quartzite	



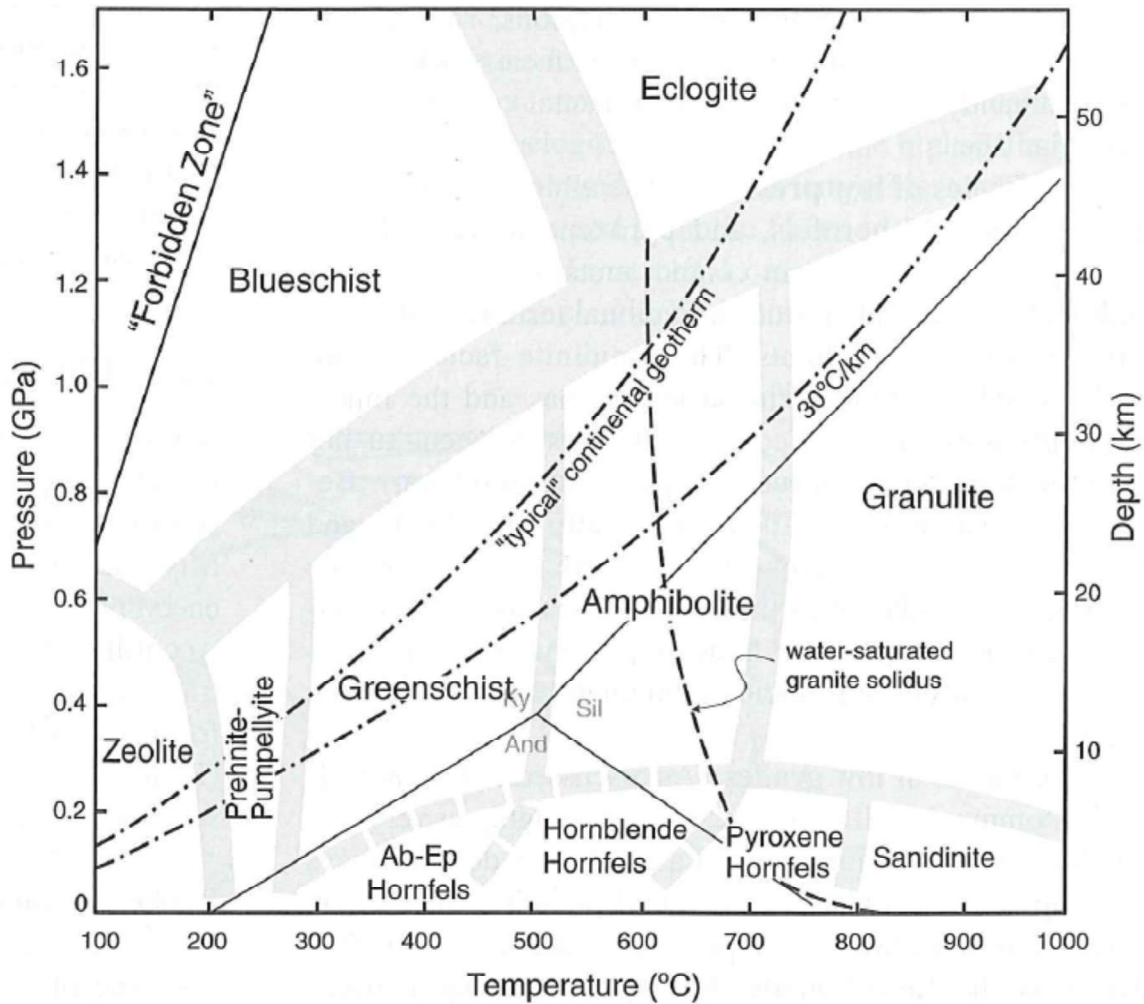
## Mineralogy for Metamorphic Rock Facies

Facies	Definitive Mineral Assemblages in Mafic Rocks
Zeolite	zeolites: especially laumontite, wairakite, analcime (in place of other Ca-Al silicates such as prehnite, pumpellyite and epidote)
Prehnite-Pumpellyite	prehnite + pumpellyite (+ chlorite + albite)
Greenschist	chlorite + albite + epidote (or zoisite) + actinolite ± quartz
Amphibolite	hornblende + plagioclase (oligoclase, andesine) ± garnet
Granulite	orthopyroxene + clinopyroxene + plagioclase ± garnet
Blueschist	glaucophane + lawsonite or epidote/zoisite (± albite ± chlorite ± garnet)
Eclogite	pyralisite garnet + omphacitic pyroxene (± kyanite ± quartz), no plagioclase
Contact Facies	mineral assemblages in mafic rocks of the facies of contact metamorphism do not differ substantially from those of the corresponding regional facies at higher pressure

# Metamorphic Rocks

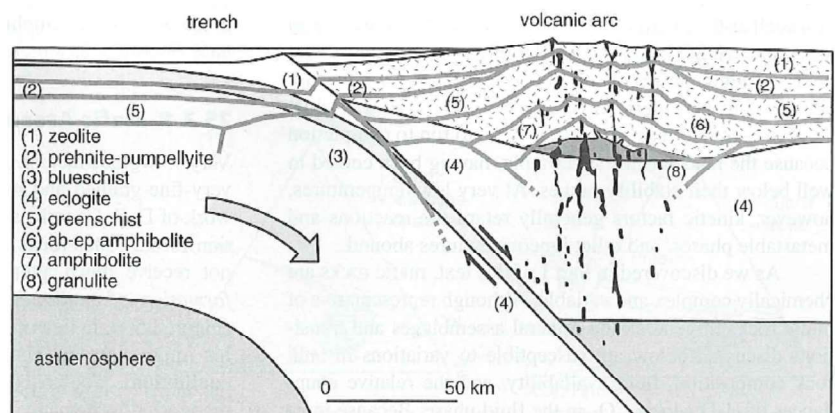
## Metamorphic Rock Facies, P vs. T diagram

From Winter, 2010



## Schematic of Island Arc, and the origins of Metamorphic Facies

A schematic cross section of an island arc. Light gray lines are isotherms. From Winter, 2010

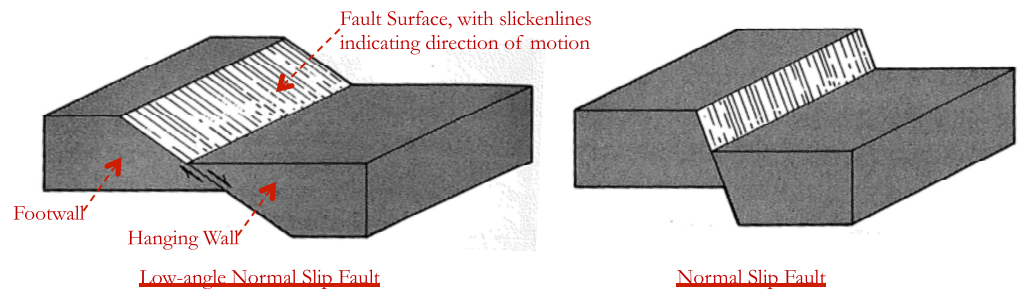




## Structural Geology: Normal Faults

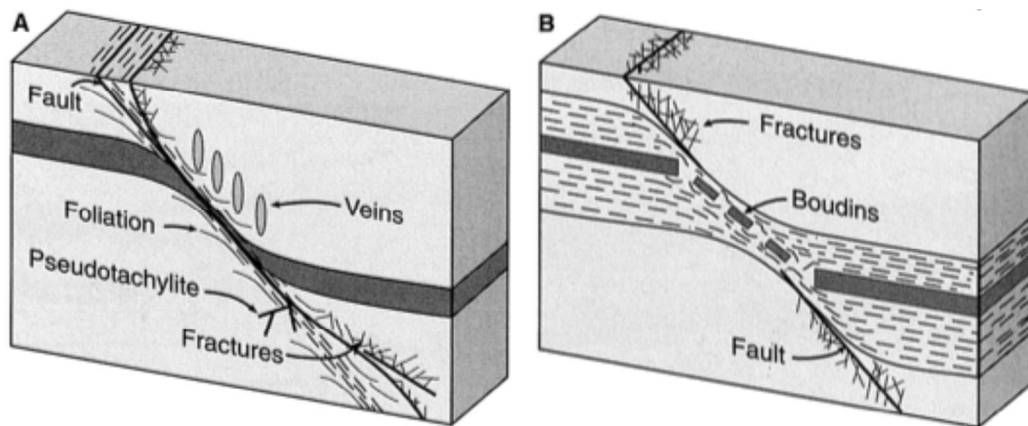
### Normal Faults ➔

In normal faults, the footwall goes up with respect to the hanging wall. Normal faults are indicative of extension. Figures from Davis & Reynolds, 1996.



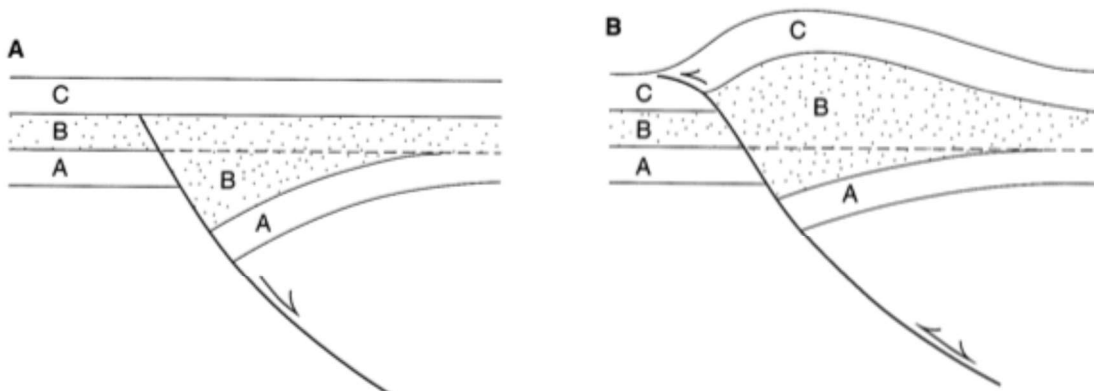
### Effects of Brittle or Ductile Shear in Normal Faults ↓

The block diagrams below illustrate the effects of changing the nature of deformation, between brittle deformation (which results in clear fault planes, fractures and fault rocks), ductile deformation (which causes deformation over a larger shear zone). Often, strata of different rheologies will behave differently, as is shown in the figure at right. The dashed layer was weak and deformed ductilely, while the middle grey layer was rigid and formed boudins. Figures from Davis & Reynolds, 1996.



### Inversion Tectonics ➔

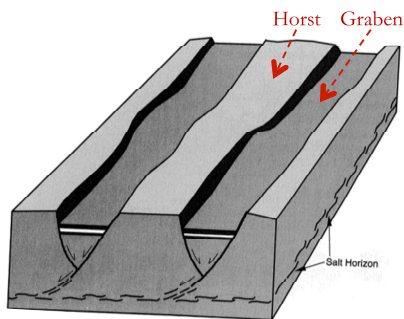
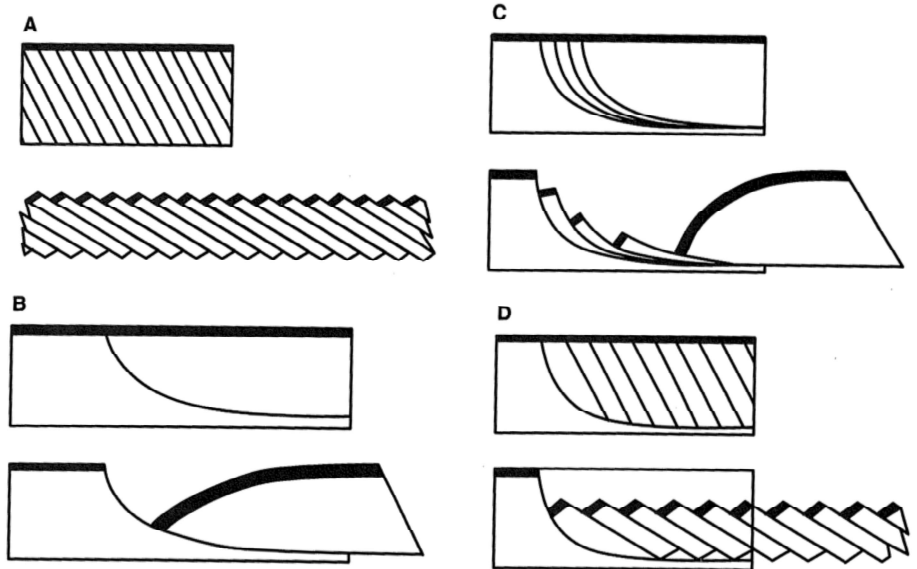
If the regional stresses change, previously inactive faults can reactivate, and change their sense of motion. In the figure at left, layer-A was formed prior to the formation of a normal fault. Layer-B and layer-C were deposited after the formation, and shut down of the fault. In the figure at the right, the fault has reactivated, though as a reverse fault. The resulting stratigraphic sequence is a combination of effects one would expect from both normal and reverse faults. Figures from Davis & Reynolds, 1996.



## Structural Geology: Normal Faults

### Normal Faults Geometries

Various normal fault geometries are possible. They all allow for lithospheric extension. (A) Domino style faulting. (B) Listric normal faulting with reverse drag. (C) Imbricate listric normal faulting. Note that listric faulting can cause extreme rotation of faulted blocks. (D) Listric normal faulting bounding a family of planar normal faults. Figures from Davis & Reynolds, 1996.

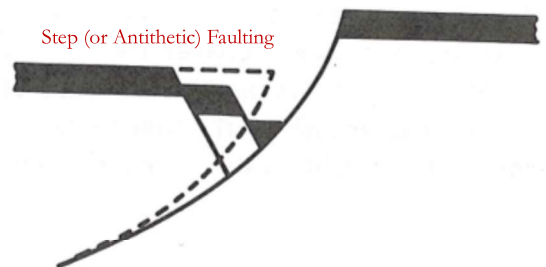
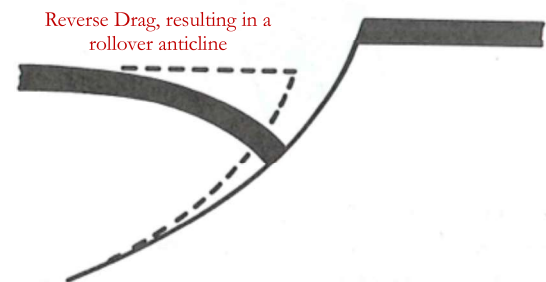
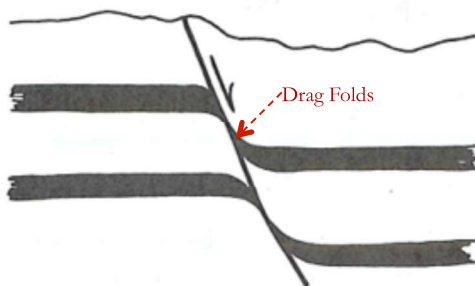


### Horsts & Grabens

Classical formation describing fault-bounded uplifted (horsts) and down-dropped blocks (grabens). Figures from Davis & Reynolds, 1996.

### Drag Folds, Reverse Drag, and Step Faulting

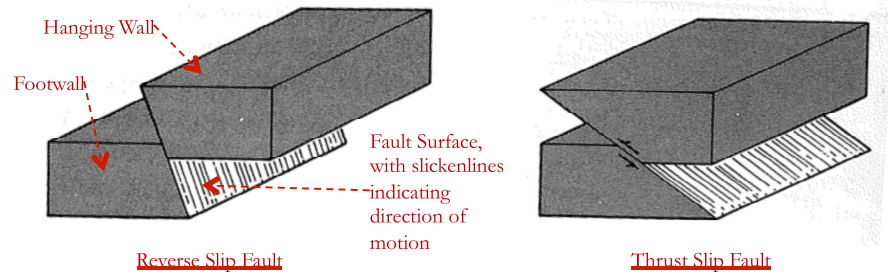
Faulting does not always produce clean displacement along the fault surface. Fault blocks are frequently folded or fractured, and the nature of these deformations are non-trivial. Figures from Davis & Reynolds, 1996.



## Structural Geology: Reverse & Thrust Faults

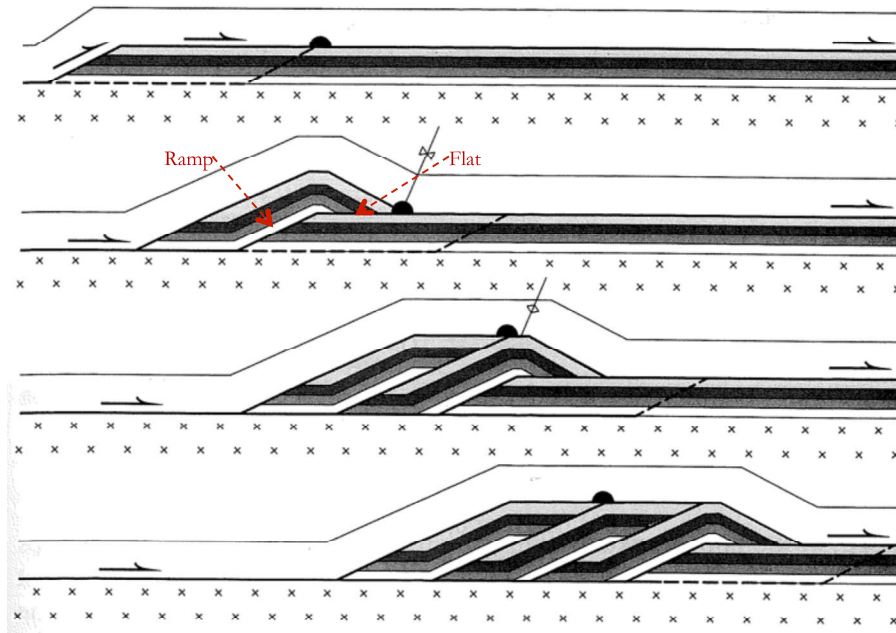
### Reverse Faults ➔

In reverse faults, the footwall goes down with respect to the hanging wall. Normal faults are indicative of compression. Thrust faults are reverse faults with fault dips  $< 45$  degrees. Figures from Davis & Reynolds, 1996.



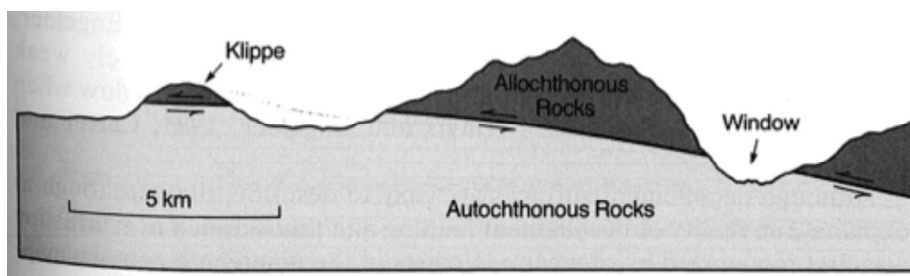
### “Ramp-Flat” Geometry of Typical Thrust Fault Systems ↓

In a regional thrust, faulted blocks are “thrust” on top of younger strata. The exact geometry of these thrust systems can vary significantly. Figures from Davis & Reynolds, 1996.

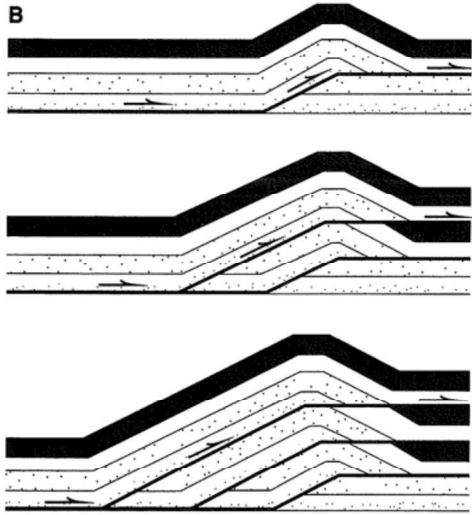


### Klippe & Windows ↓

Thrust faults move large blocks of non-indigenous rock (referred to as “allochthonous” rock) over emplaced rock (referred to as “autochthonous” rock). If the overlying allochthonous rock is eroded, it can create windows into the lower underlying autochthonous rock. Erosion can also create islands of isolated allochthonous rock, called klippe. Figures from Davis & Reynolds, 1996.



## Structural Geology: Reverse & Thrust Faults

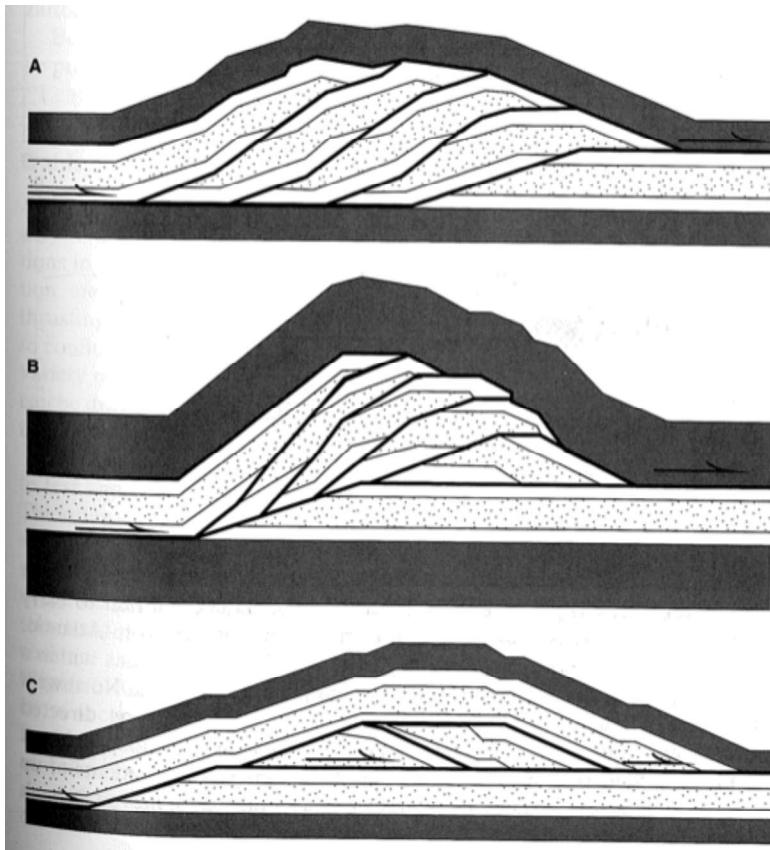
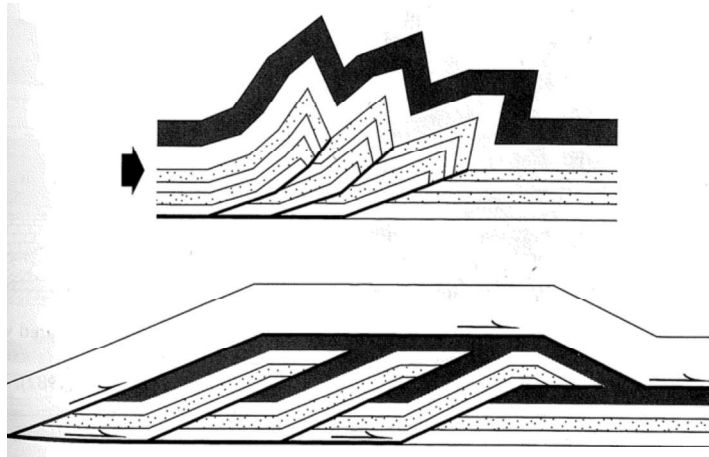


### ← Out-of-Sequence Thrust Fault System

Unlike “in-sequence” thrust fault systems (as shown on the previous page, the “roof” of the thrust block in an out-of-sequence system becomes the “flat” for subsequent fault blocks. Figures from Davis & Reynolds, 1996.

### Imbricate Fans vs. Duplexes ↓

Two thrust fault geometries: imbricate fans (top) and duplexes (bottom). Figures from Davis & Reynolds, 1996.



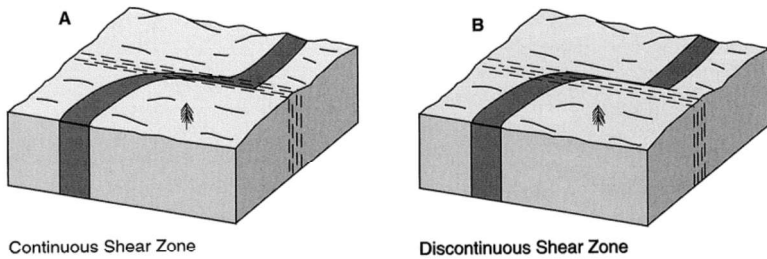
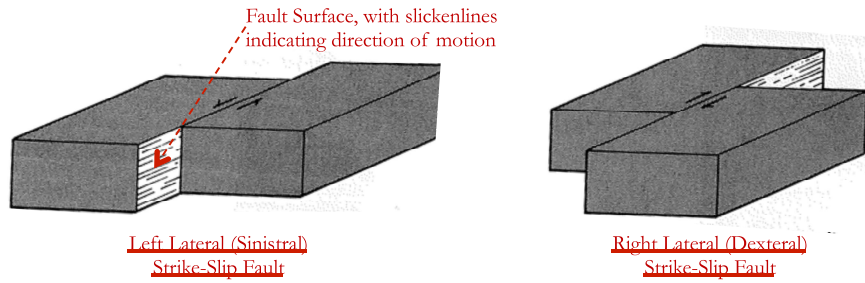
### ← Forms of Duplexes

The exact form of a duplex or imbricate fan depends on the spacing of ramps and the amount of slip. (A) A normal duplex develops when slice length exceeds the fault slip. (B) An antiformal duplex develops when slice length and fault slip are effectively equal. (C) A forward-dipping duplex develops when the fault slip is greater than the slice length. Figures from Davis & Reynolds, 1996.

# Structural Geology: Strike-Slip or Transform Faults

## Strike-Slip Faults ➔

In reverse faults, the footwall goes down with respect to the hanging wall. Normal faults are indicative of compression. Thrust faults are reverse faults with fault dips <45 degrees. Figures from Davis & Reynolds, 1996.

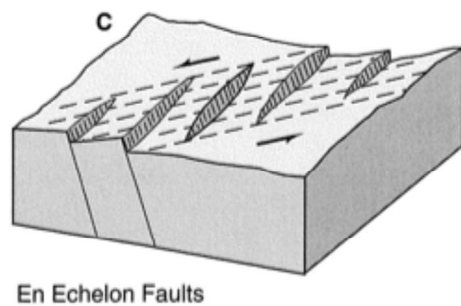
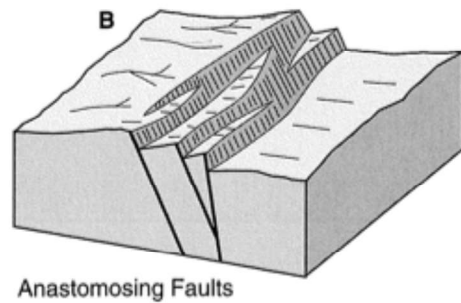
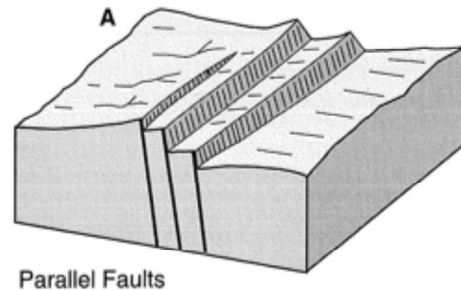
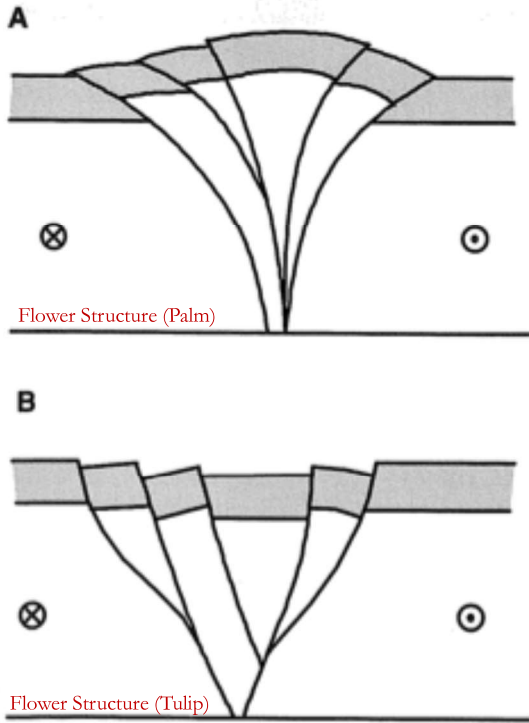


## ➔ Ductile Shear Zones

Shear in a strike-slip fault is not always located in a single plane. Sometimes, shear takes place over an extended region. Figures from Davis & Reynolds, 1996.

## Brittle Shear Zones ➔

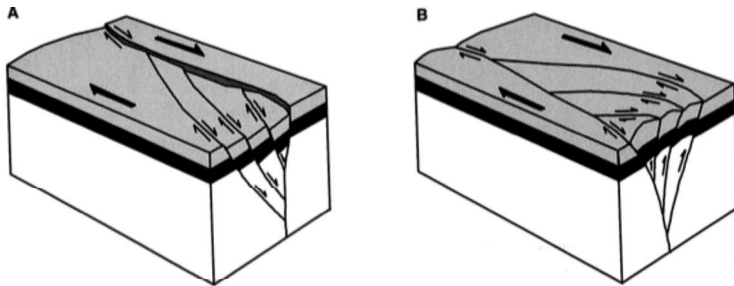
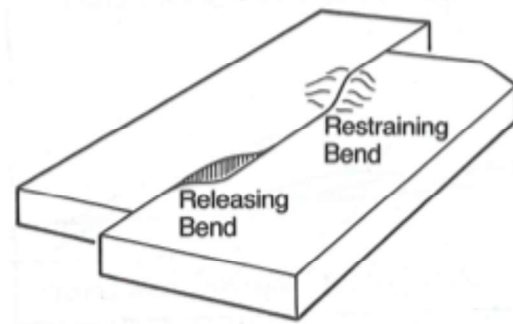
Figures from Davis & Reynolds, 1996.



# Structural Geology: Strike-Slip or Transform Faults

## Bends in Strike-Slip Faults →

Strike-slip faults along irregularly curved faults creates localized regions of extension and compression. Figures from Davis & Reynolds, 1996.

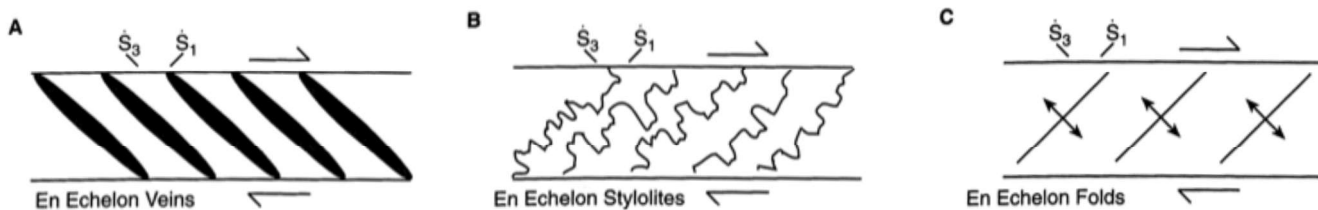


## ← Strike-Slip Duplexes

(A) Extensional duplexes can form at releasing bends. (B) Compressional duplexes can form at restraining bends. Figures from Davis & Reynolds, 1996.

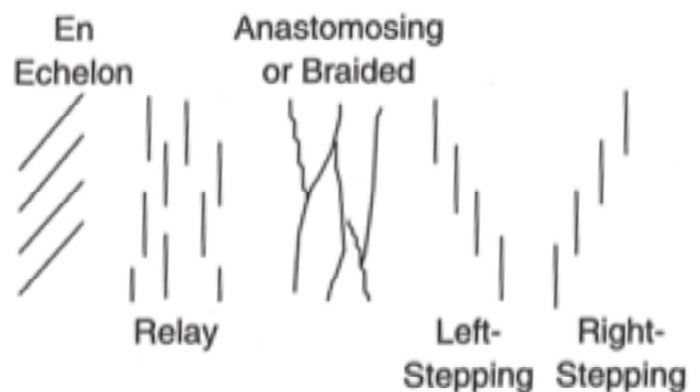
## Slip Indicators in Strike-Slip Systems ↓

In strike-slip systems, the maximum ( $S_1$ ) and minimum compressional stresses ( $S_3$ ) are at an angle with respect to the sense of shear. This can lead to the formation of both large scale folds and faults, or small scale fractures or veins, which are indicative to the sense of motion. Figures from Davis & Reynolds, 1996.



## Even more Geometric Arrangements of Strike-Slip Faults →

Figures from Davis & Reynolds, 1996.

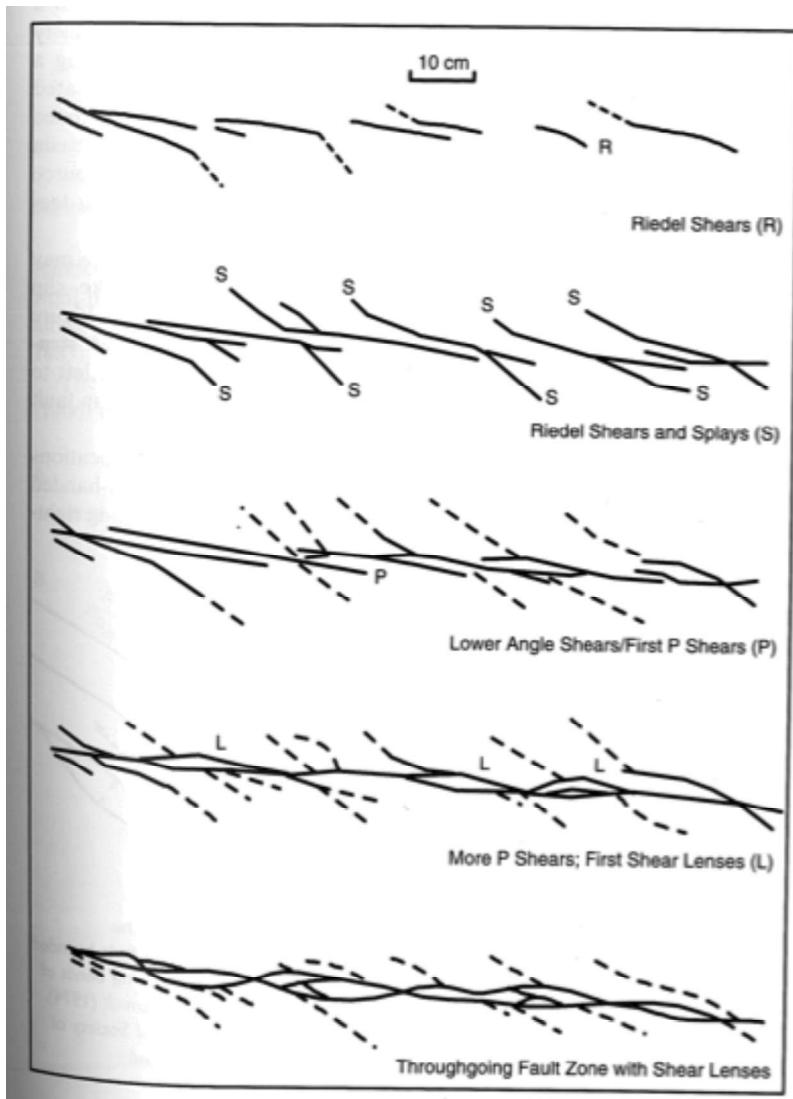
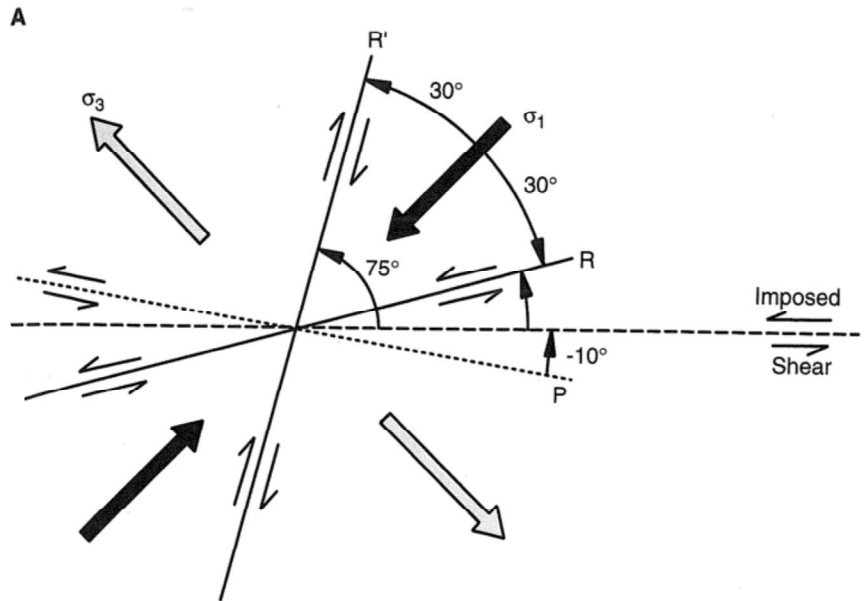


## Structural Geology: Strike-Slip or Transform Faults

### Riedel Shears



When under compression, rocks tend to form fail with faults forming  $30^\circ$  from the primary compressional stress. In a strike-slip fault, the primary compressional stress ( $\sigma_1$ ) is  $45^\circ$  away from the plane of strike-slip shearing. The combination of these two facts results in fractures at interesting angles with respect to the motion of shear. These are called Riedel shears. The figure below shows a left-handed strike-slip zone. Figures from Davis & Reynolds, 1996.

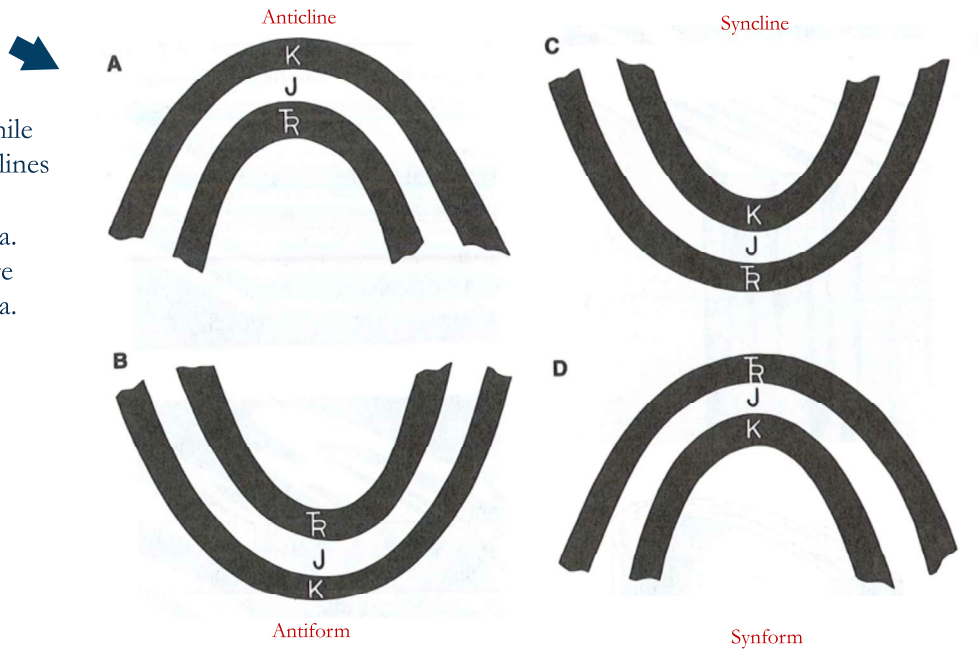


The figure at left illustrate the formation sequence of Riedel shears and other splays and shears in a right-handed strike-slip zone. Figures from Davis & Reynolds, 1996.

# Structural Geology: Folds

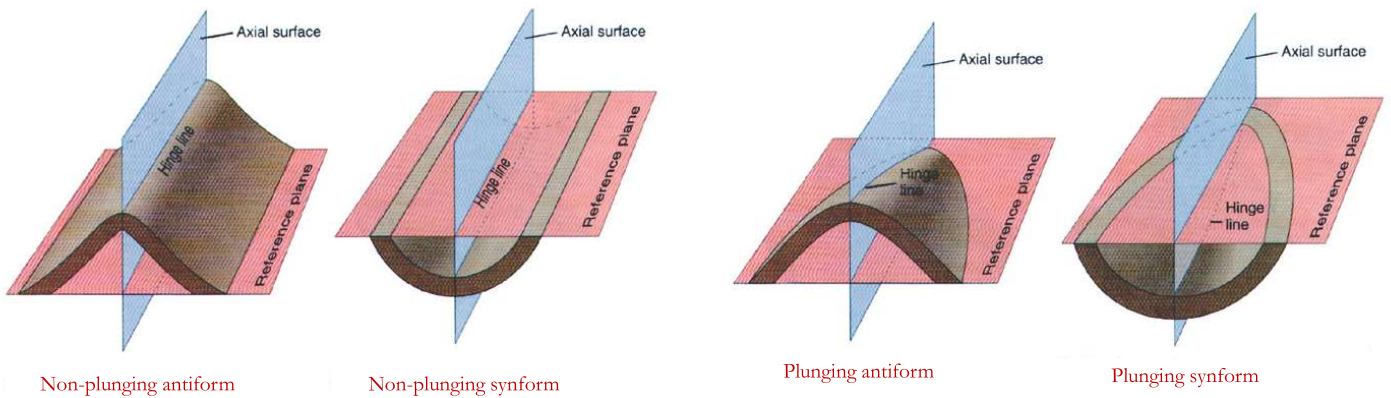
## Anticlines & Antiforms, and Synclines & Synforms

Antiforms are concave-down folds, while Synforms are concave-up folds. Anticlines are antiforms where we know that the younger strata lie on top of older strata. Similarly, Synclines are antiforms where younger strata lie on top of older strata. Figures from Davis & Reynolds, 1996.



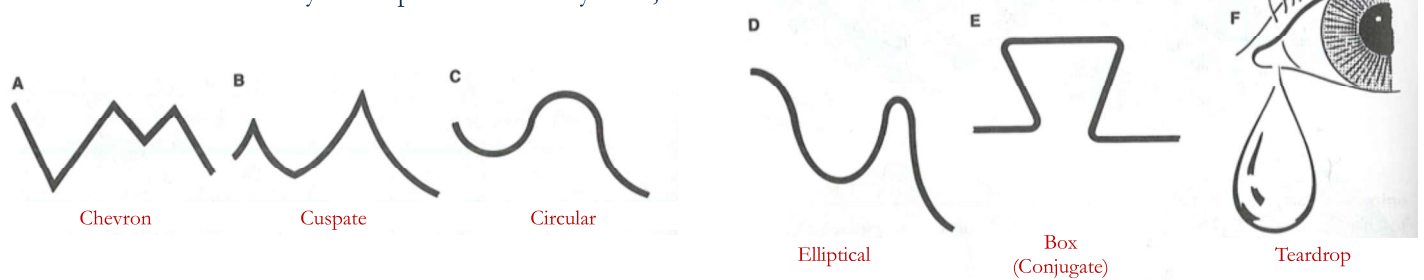
## Plunging Folds

Folds (defined by hinge lines and axial surfaces) are not necessarily perpendicular to the Earth's surface. They can be dipping into or out of the surface. This can create interesting patterns of exposed surface rock, or even topography. Figures from Jones, 2001.



## Fold Shapes

Folds can come in a variety of shapes. Davis & Reynolds, 1996.

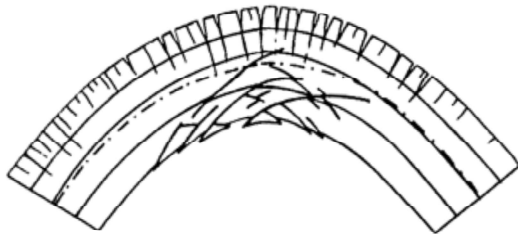
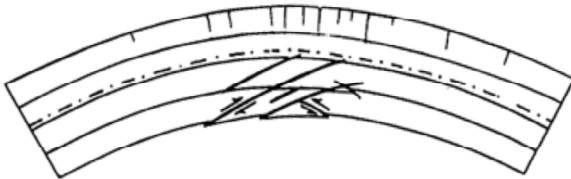
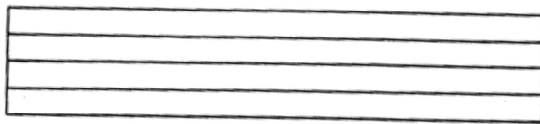
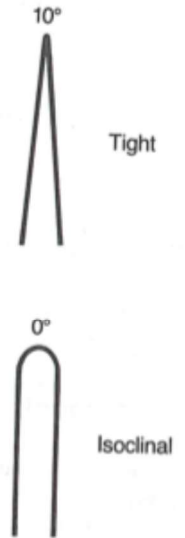
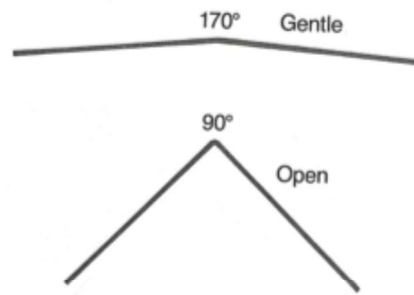
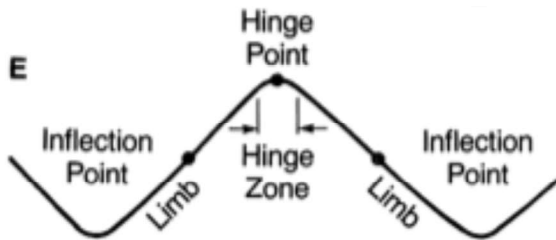




# Structural Geology: Folds

## Fold Tightness

Fold tightness is based upon the size of the inter-limb angle. Figures from Davis & Reynolds, 1996.

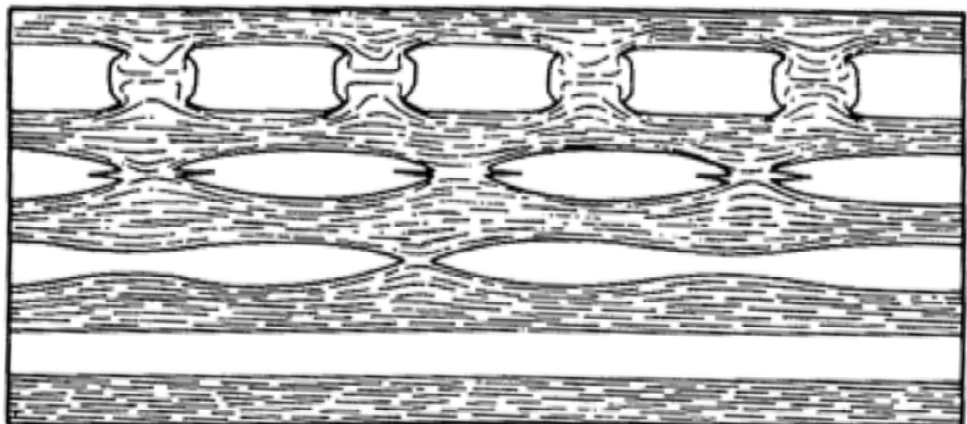


## Minor Structures in Folds

When folding layers of strata, layer-parallel stretching occurs in the outer arc of a folded layer, while layer-parallel shortening occurs in the inner arc. Figures from Davis & Reynolds, 1996.

## Boudins

Layer-parallel stretching can pinch off layers of strata, depending on the ductility contrast between layers. This can result in pinch-and-swell structures or boudins (where the pinching completely pinches off portions of a given strata). Figures from Davis & Reynolds, 1996.



# Geologic Map Symbols

1		Contact, showing dip where trace is horizontal, and strike and dip where trace is inclined	42		Steeply plunging monocline or flexure, showing trace in horizontal section and plunge of hinges
2		Contact, located approximately (give limits)	43		Plunge of hinge lines of small folds, showing shapes in horizontal section
3		Contact, located very approximately, or conjectural	44		Strike and dip of beds or bedding
4		Contact, concealed beneath mapped units	45		Strike and dip of overturned beds
5		Contact, gradational (optional symbols)	46		Strike and dip of beds where stratigraphic tops are known from primary features
6		Fault, nonspecific, well located (optional symbols)	47		Strike and dip of vertical beds or bedding (dot is on side known to be stratigraphically the top)
7		Fault, nonspecific, located approximately	48		Horizontal beds or bedding (as above)
8		Fault, nonspecific, assumed (existence uncertain)	49		Approximate (typically estimated) strike and dip of beds
9		Fault, concealed beneath mapped units	50		Strike of beds exact but dip approximate
10		Fault, high-angle, showing dip (left) and approximate dips	51		Trace of single bed, showing dip where trace is horizontal and where it is inclined
11		Fault, low-angle, showing approximate dip and strike and dip	52		Strike and dip of foliation (optional symbols)
12		Fault, high-angle normal (D or ball and bar on downthrown side)	53		Strike of vertical foliation
13		Fault, reverse (R on upthrown side)	54		Horizontal foliation
14		Fault, high-angle strike-slip (example is left lateral)	55		Strike and dip of bedding and parallel foliation
15		Fault, thrust (T on overthrust side)	56		Strike and dip of joints (left) and dikes (optional symbols)
16		Fault, low-angle normal or detachment (D on downthrown side)	57		Vertical joints (left) and dikes
17		Fault, low-angle strike-slip (example is right lateral)	58		Horizontal joints (left) and dikes
18		Fault, low-angle, overturned (teeth in direction of dip)	59		Strike and dip of veins (optional symbols)
19		Optional sets of symbols for different age-groups of faults	60		Vertical veins
20		Fault zone or shear zone, width to scale (dip and other accessory symbols may be added)	61		Horizontal veins
21		Faults with arrows showing plunge of rolls, grooves or slickensides	62		Bearing (trend) and plunge of lineation
22		Fault showing bearing and plunge of net slip	63		Vertical and horizontal lineations
23		Point of inflection (bar) on a high-angle fault	64		Bearing and plunge of cleavage-bedding intersection
24		Points of inflection on a strike-slip fault passing into a thrust	65		Bearing and plunge of cleavage-cleavage intersections
25		Fault intruded by a dike	66		Bearings of pebble, mineral, etc. lineations
26		Faults associated with veins	67		Bearing of lineations in plane of foliation
27		Anticline, showing trace and plunge of hinge or crest line (specify)	68		Horizontal lineation in plane of foliation
28		Syncline (as above), showing dip of axial surface or trough surface	69		Vertical lineation in plane of vertical foliation
29		Folds (as above), located approximately	70		Bearing of current from primary features; from upper left: general; from cross-bedding; from flute casts; from imbrication
30		Folds, conjectural	71		Bearing of wind direction from dune forms (left) and cross-bedding
31		Folds beneath mapped units	72		Bearing of ice flow from striations (left) and orientation of striations
32		Asymmetric folds with steeper limbs dipping north (optional symbols)	73		Bearing of ice flow from drumlins
33		Anticline (top) and syncline, overturned	74		Bearing of ice flow from crag and tail forms
34		Antiformal (inverted) syncline	75		Spring
35		Synformal (inverted) anticline	76		Thermal spring
36		Antiform (top) and synform (stratigraphic sequence unknown)	77		Mineral spring
37		Separate dome (left) and basin	78		Asphaltic deposit
38		Culmination (left) and depression	79		Bituminous deposit
40		Vertically plunging anticline and syncline	80		Sand, gravel, clay, or placer pit
41		Monocline, south-facing, showing traces of axial surfaces			

## Geologic Map Symbols

81		Mine, quarry, or open pit
82		Shafts: vertical, inclined, and abandoned
83		Adit, open (left) and inaccessible
84		Trench (left) and prospect
85		Water wells: flowing, nonflowing, and dry
86		Oil well (left) and gas well
87		Well drilled for oil or gas, dry
88		Wells with shows of oil (left) and gas
89		Oil or gas well, abandoned (left) and shut in
90		Drilling well or well location
91		Glory hole, open pit, or quarry, to scale
92		Dump or fill, to scale

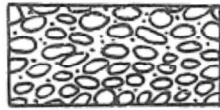
## Fossil and Structural Symbols for Stratigraphic Columns

	Algae		Tree trunk fallen		Foraminifers, general		Scour casts
	Algal mats		Trilobites		Foraminifers, large		Convolution
	Ammonites		Vertebrates		Fossils		Slumped beds
	Belemnites		Wood		Fossils abundant		Paleosol
	Brachiopods		Beds distinct		Fossils sparse		Mud cracks
	Bryozoans		Beds obscure		Gastropods		Salt molds
	Corals, solitary		Unbedded		Graptolites		Burrows
	Corals, colonial		Graded beds		Leaves		Pellets
	Crinoids		Planar cross-bedding		Ostracodes		Oolites
	Echinoderms		Trough cross-bedding		Pelecypods		Pisolites
	Echinoids		Ripple structures		Root molds		Intraclasts
	Fish bones		Cut and fill		Spicules		Stylolite
	Fish scales		Load casts		Stromatolites		Concretion
-					Tree trunk in place		Calcitic concretion

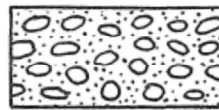
# Lithologic Patterns for Stratigraphic Columns & Cross Sections



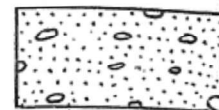
1. Breccia



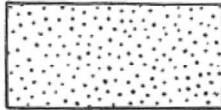
2. Clast-supported conglomerate



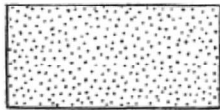
3. Matrix-supported conglomerate



4. Conglomeratic sandstone



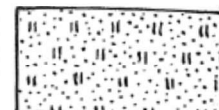
5. Coarse sandstone



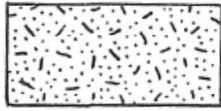
6. Fine sandstone



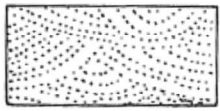
7. Feldspathic sandstone



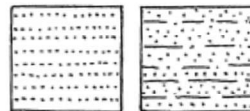
8. Tuffaceous sandstone



9. Graywacke



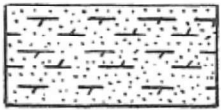
10. Cross-bedded sandstone



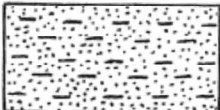
11. Bedded sandstone



12. Calcite-cemented sandstone



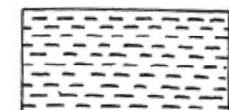
13. Dolomite-cemented sandstone



14. Silty sandstone



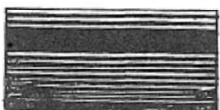
15. Siltstone



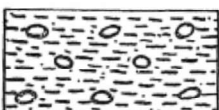
16. Mudstone



17. Shale



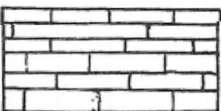
18. Coal bed with carbonaceous shale



19. Pebbly mudstone



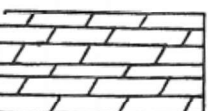
20. Calcareous shale



21. Limestone



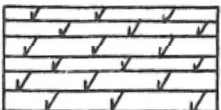
22. Cross-bedded limestone



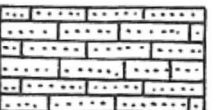
23. Dolomite (dolostone)



24. Dolomitic limestone



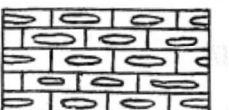
25. Calcitic dolomite



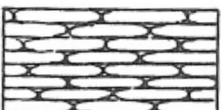
26. Sandy limestone



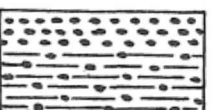
27. Clayey limestone



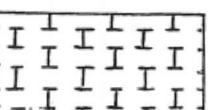
28. Cherty limestone



29. Bedded chert



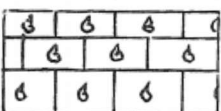
30. Phosphorite, phosphatic shale



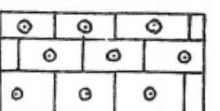
31. Chalk



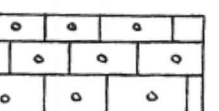
32. Marl



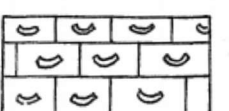
33. Fossiliferous limestone



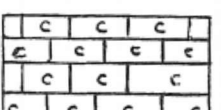
34. Oolitic limestone



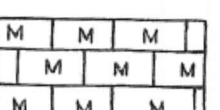
35. Pelletal limestone



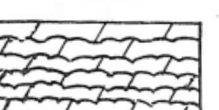
36. Intraclastic limestone



37. Crystalline limestone



38. Micritic limestone



39. Algal dolomite



40. Limestone conglomerate

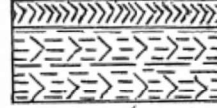
# Lithologic Patterns for Stratigraphic Columns & Cross Sections



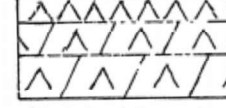
41. Limestone breccia



42. Algal dolomite breccia



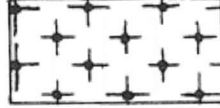
43. Gypsum bed, gypsiferous shale



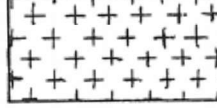
44. Anhydrite, anhydritic dolomite



45. Rock salt, salty mudstone



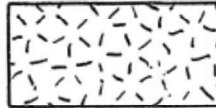
46. Peridotite



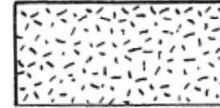
47. Gabbro



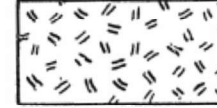
48. Mafic plutonic rock



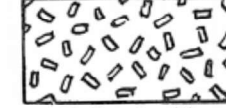
49. Coarse granitic rock



50. Fine granitic rock



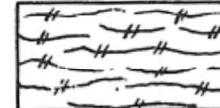
51. Porphyritic plutonic rock



52. Porphyritic plutonic rock



53. Mafic lava



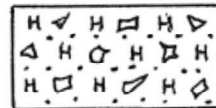
54. Silicic lava



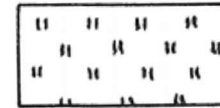
55. Intrusive volcanic rocks



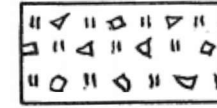
56. Pillow lava



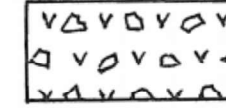
57. Hyaloclastite



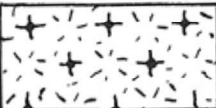
58. Tuff



59. Tuff-breccia



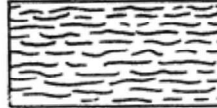
60. Volcanic breccia



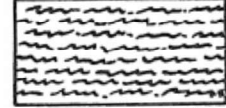
61. Massive serpentinite



62. Foliated serpentinite



63. Schist



64. Crenulated schist



65. Folded schist



66. Semischistose sandstone



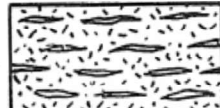
67. Semischistose limestone



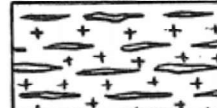
68. Semischistose gabbro



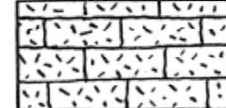
69. Greenstone



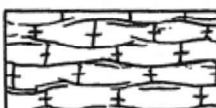
70. Silicic gneiss



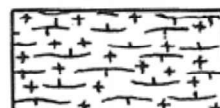
71. Mafic gneiss



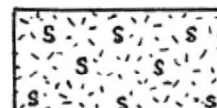
72. Marble



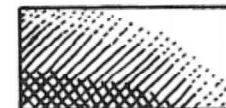
73. Foliated marble



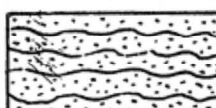
74. Foliated calc-silicate rock



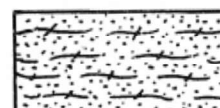
75. Massive skarn



76. Alteration zones



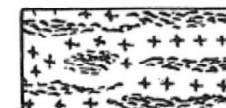
77. Quartzite



78. Quartzite

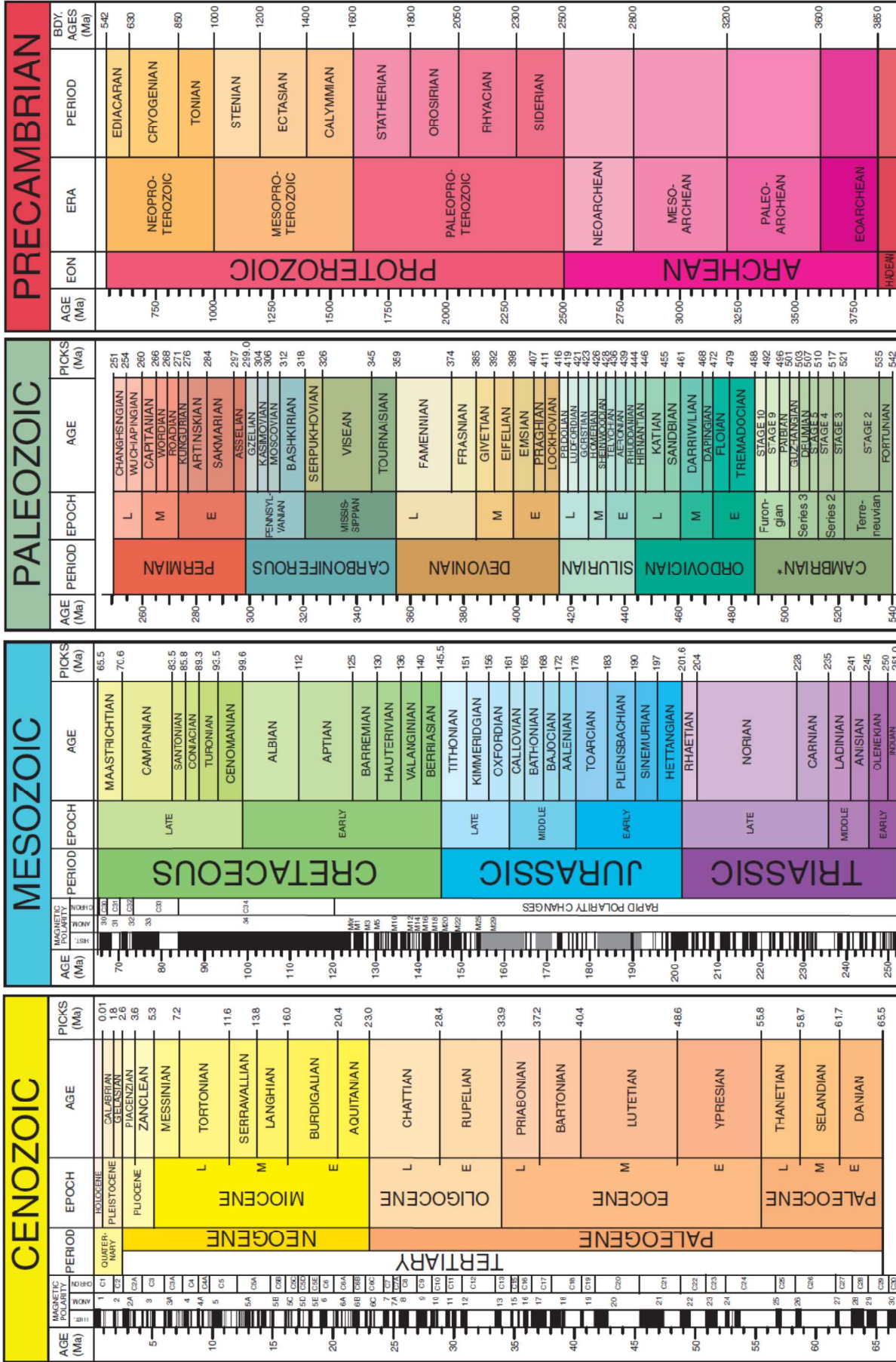


79. Silicic migmatite



80. Mafic migmatite

# Geologic Timescale



# B<sup>85</sup>attleship



Another fun activity from:

[www.funorama.com](http://www.funorama.com)

Defensive Grid

A										
B										
C										
D										
E										
F										
G										
H										
I										
J										
	1	2	3	4	5	6	7	8	9	10

Put the following ships on your defensive grid by placing the appropriate letters -- horizontally, vertically or diagonally.

1 - Aircraft Carrier

A	A	A	A	A
---	---	---	---	---

1 - Battleship

B	B	B	B
---	---	---	---

1 - Cruiser

C	C	C
---	---	---

2 - Destroyers

D	D		D	D
---	---	--	---	---

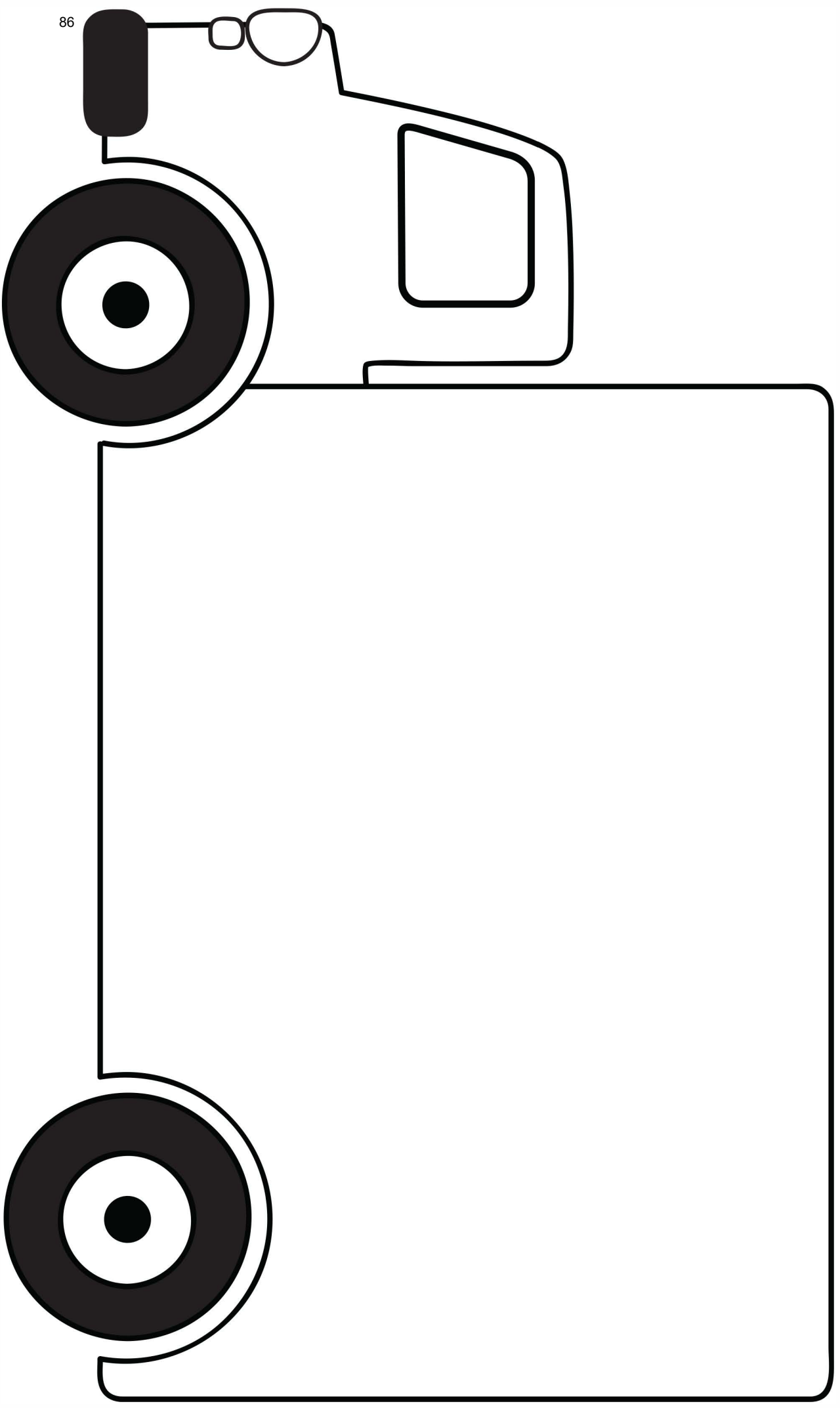
Offensive Grid

A										
B										
C										
D										
E										
F										
G										
H										
I										
J										
	1	2	3	4	5	6	7	8	9	10

Instructions (2 Players Required):

Both players place their ships on the defensive grid according to the chart above. Whoever goes first calls out a position (i.e. G-6). The other player says either "Hit" or "Miss" depending upon whether one of his ships is in the position called out. The person calling out should mark a hit or a miss on the "offensive grid" to keep track of the shots. The other person should mark the shot on the "defensive grid". If the shot is a "Hit", the player goes again--otherwise the other player takes a turn. Once the opposing player has scored a hit on all of the spaces for a particular ship, you must call out "Hit...you sunk my Cruiser" (or whatever type of ship it was). Once a player has sunk all the opponents ships, he is declared the winner.

What's in the truck?





1 87

		5			7			
						9		2
7		1	2		9	6		
9	5			8		3		
	2			3	6			
		7			5		1	
			6				5	9
5	3			9				
			1	5		2	6	

2

		2		8				
	1				3	4	9	
		9		7				5
6	4					3		
					4	8		9
		5		2	7			4
	9						1	
			8	9	2			
		7	1	4				2

3

			6	5				
7				4		9	5	2
3		5	1					4
		3					4	5
2		7					9	
4			5	2	6		7	
	7				8	5		
		4				7	2	
	9				5		6	

4

	4		3					9
		7	6		5			
		2	4			5		1
1		3						2
8					4			
2					6	9	8	
	3	1	7					
	9			2				5
	2					1	9	4

5

					1		8	2
			5	6		1		7
6	3			7	2			
			7			9	1	
		3	4		6	7		
		2					4	
	1				3		7	
	2	5		1				
		6		5		3		

6

			4			8		2
3		7			5			
		2				9		
9		3				1		
		1			7	4	9	8
			6		1			7
	3		8	6		2	4	
	4		3	5				
2	9						3	

7 88

	3		2		4	5		8
		4	6		7			2
		5			3			4
	2	1					4	
	5		9	3	2			
	6					3		
5			4	7				
6			3	1		7	5	
7							1	6

8

2	5			7				
			5	9		1	3	
				2	3		6	7
							9	6
8	1	4						
			7		5			
4		2	1			6		
		8			6	3	1	
		1		3		8		9

9

		8	2				1	5
2			3	6				
9	5	6					2	
								4
7		5		3	2			
			6	5	7		8	
	6	1				4		
			1	4	3	5		
	2					8	7	

10

1			7	8	4			
8	2					9	3	
	6				2			
			3	2				7
		5		9			8	2
6	1							
					8	5	9	
9		6		5				
7						8	2	3

11

	5	9		8				
						2		7
		7	6	1				
	1	6	5	9			8	
			7					1
	9	8				6	2	
8					9		4	
2							1	8
9	6				5			2

12

					5	4		6
	6	2			9	1		
9				8	4			
	9					6		5
3		8		2				
		5			8	2	1	
8			7	6			2	
							4	7
1		7	4					

# SUPER TIC TAC TOE

Like the normal version, but more. The board is made up of 9 sub-games within the larger supergame. Player one begins by placing an X inside one of the sub-games. The square chosen within that sub-game determines the next sub-game for player two to make their move, and so on. For example, if player one chooses the middle square in the upper-right sub-game, player two must place their move within the middle sub-game. If you win a sub-game, you win that space in the uber-game. Connect three squares in a row in the super game to win. This game can be broken. There might not be a winner. Maybe you'll have fun. You'll probably get mad at your opponent.

